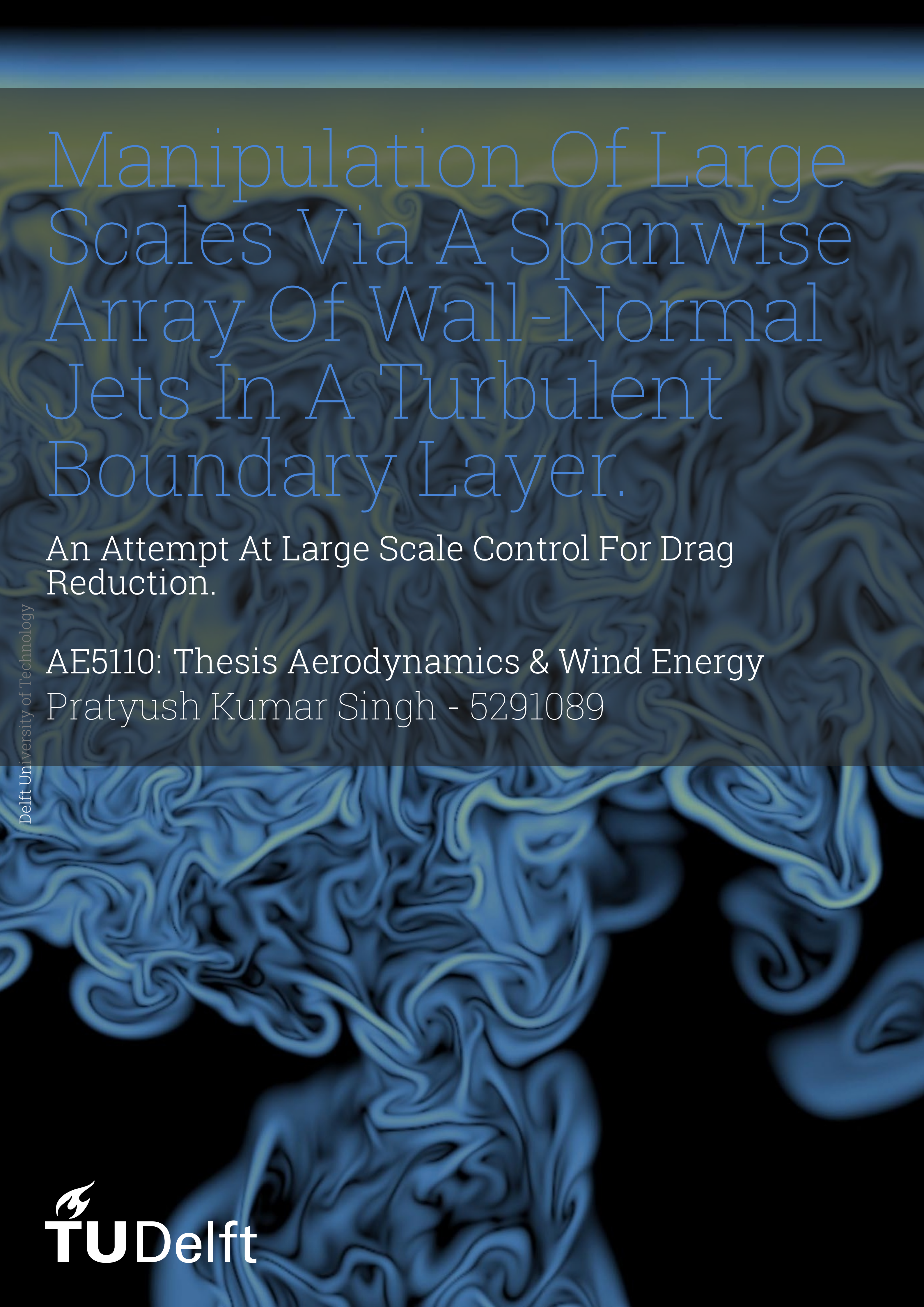

Manipulation Of Large Scales Via A Spanwise Array Of Wall-Normal Jets In A Turbulent Boundary Layer.

An Attempt At Large Scale Control For Drag Reduction.

AE5110: Thesis Aerodynamics & Wind Energy

Pratyush Kumar Singh - 5291089

Delft University of Technology

TU Delft

Manipulation Of Large Scales Via A Spanwise Array Of Wall-Normal Jets In A Turbulent Boundary Layer.

An Attempt At Large Scale Control For Drag Reduction.

by

Pratyush Kumar Singh - 5291089

to obtain the degree of

Master of Science in Aerodynamics

in the faculty of Aerospace Engineering

at the Delft University of Technology,

Student number:	5291089	
Project duration:	January, 2022 – February, 2023	
Thesis committee:	Dr. ir. W.J. Baars,	Thesis Supervisor
	Dr.ir. B.V Oudheusden,	Thesis Chair
	Dr. D. Ragni,	Examiner
	ir. G. Dacome,	P.h.d Supervisor

This thesis is confidential and cannot be made public until April, 2023.

Abstract

In recent years, research for turbulent boundary layer (TBL) has shifted towards developing novel approaches to reduce drag. This shift is driven by new industrial standards emphasizing fuel-efficient and environmentally friendly air transportation. As wall-bounded turbulence plays a significant role in the overall drag experienced by an aircraft, any understanding and control authority on associated flow structures becomes vital for more optimized and efficient flow control techniques to reduce drag. In this context, conventional passive flow control techniques have been widely used as they are simple and do not require any external power supply. However, active flow control techniques have demonstrated the potential for greater effectiveness, which offers more substantial drag reduction. Existing active control methods, such as wall oscillation, traveling wave, blowing, and suction, have been previously studied to reduce the viscous drag in the TBL. However, the efficacy of such control strategies tuned to outer layer large-scale motions (LSMs) at higher Reynolds number (Re) flows has emerged as a promising avenue for achieving significant drag reduction. In contrast, control techniques targeting the inner layer small-scales encounter limitations due to restricted control authority and the difficulties associated with miniaturizing hardware at higher Re flows.

LSMs convecting in the logarithmic region (log region) of TBL play a critical role in the dynamics of wall-bounded turbulence, as they carry a significant portion of the turbulent kinetic energy (TKE) [Abbassi et al., 2017]. The active wall oscillation technique tuned to the frequency of the LSMs has proven to be energy-efficient, as drag reduction increases with the frictional Reynolds number (Re_τ) and the contribution of LSMs to the TKE and wall shear stress increases with the Re_τ [Marusic et al., 2021]. In this thesis work, the receptivity of LSMs to active large-scale control strategy is assessed via a spanwise array of wall-normal jets in a TBL. Multiple wall-normal jets manipulate the flow over a flat plate by introducing a spanwise traveling wave, which aims to mimic wall oscillation tuned to the large scales in the log region of the TBL.

To assess the efficacy of the suggested control strategy with spatial and temporal tuning, particle image velocimetry (PIV) and hot-wire anemometry (HWA) are employed to quantify second-order turbulence statistics and analyze the organization of the coherent patterns introduced in the flow via two-point correlations. In addition, the effect of different control cases derived from different tuning and control strategies is analyzed at $Re_\tau = 2227$. The TKE production plots show that control cases targeting the LSMs effectively attenuate the TKE production near the wall. Furthermore, based on the analysis of the spectral energy plot of streamwise velocity fluctuations, it is observed that the energy content associated with larger length scales convecting in the middle of the log region decreases in the controlled case compared to the uncontrolled base case. This finding suggests that certain control cases notably impact the organization of LSM and second-order turbulence statistics far downstream of the actuation point. Additionally, the reduction in TKE production near the wall represents a reduction in wall shear stress and viscous drag. However, additional research must be conducted in the future based on the current findings to reach a definitive conclusion regarding the efficacy of individual control cases.

Preface

This thesis report concludes my thesis work on manipulating large-scales and very large-scale motions in a turbulent boundary layer via a spanwise array of wall-normal jets as a completion of my master's program at TU Delft's Faculty of Aerospace Engineering. This period has enabled me to grow as an engineer by allowing me to develop myself and think analytically.

Secondly, I'd like to thank my supervisor, **Dr. ir. Woutijn Baars** for supervising the project and providing constant feedback support. My supervisor's positive attitude and constructive remarks constantly created a motivating environment for me. I would also like to thank **ir. Giulio Dacome** for his time, understanding, and continuous support. Their comments and assistance during this period have significantly impacted my professional growth and technical understanding.

I am fortunate to have my friends and family's unwavering support and encouragement. They have been a constant source of encouragement and motivation throughout this journey. Their words of encouragement, kindness, and faith in my abilities were crucial in assisting me in navigating the challenges and uncertainties of the TUD MSc program. Before concluding, I would like to acknowledge and thank all lab technicians for their assistance and support during my thesis phase. Finally, after completing my thesis, I plan to produce a resourceful and significant results to boost my future career in aerodynamics.

Pratyush Kumar Singh - 5291089
Delft, April 2023

Contents

List of Figures

List of Tables

1

Introduction

The aviation industry is an integral part of modern civilization, playing a crucial role in connecting people and goods around the globe. However, socioeconomic and political reforms in recent years have prompted major polluting industries, such as the energy sector, to transition to renewable/sustainable energy sources. Although not the largest polluter, the aviation industry has also been subjected to increasingly strict regulations and mounting pressure to reduce its global greenhouse gas emissions [Airbus, 2020]. Moreover, according to Figure 1.1, Airbus predicts that the number of commercial and transport aircraft will double over the next two decades. This increase will likely lead to a significant rise in greenhouse gas emissions unless the industry implements more sustainable practices and technologies.

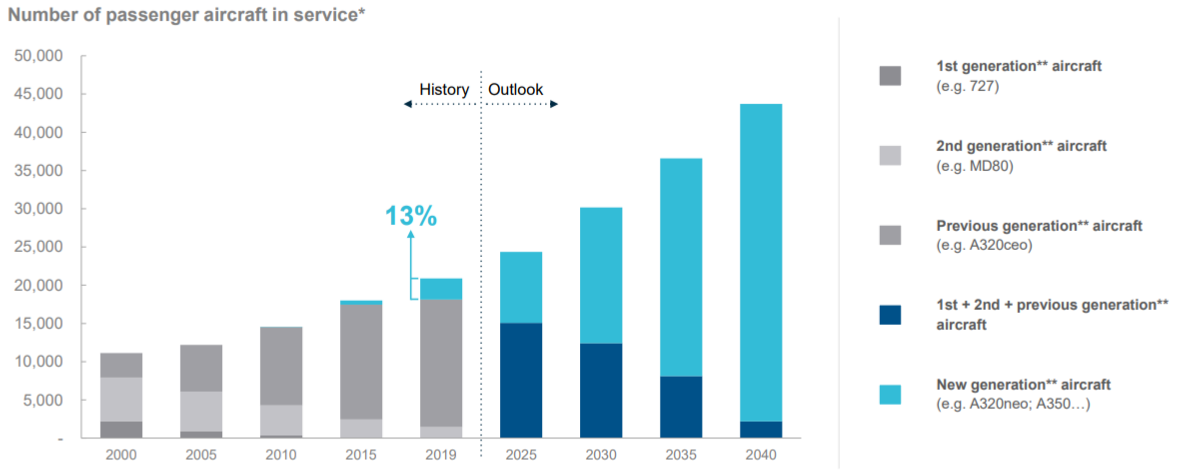

Figure 1.1: Market forecast for passenger aircraft requirement for the next 20 years [Airbus, 2020].

Drag is a major factor contributing to fuel consumption and greenhouse gas emissions; therefore, reducing drag considerably enhances fuel efficiency and extends the range of aircraft. In recent years, research has pivoted towards sustainable aviation, taking into account the industry's future and global impact. Given that viscous drag constitutes 50% of the total drag and fuel represents roughly 20% of an airliner's overall operating expenses, any decrease in drag significantly affects the aircraft's operational costs.

Drag force is a force that opposes the motion of a body through a fluid medium. The drag force for any subsonic flow can be roughly divided into pressure drag and viscous drag (also referred to as skin-friction drag) based on the various fluid phenomena acting on a body and generating drag.

1. **Pressure Drag** - Pressure drag is caused by a pressure difference around a body moving in a fluid medium. As the body moves, the fluid is forced to flow around it, generating higher and lower pressure zones around the body. These pressure differences provide a net force that resists the body's motion, known as pressure drag. Pressure drag is proportional to the square of the body's speed as well as the size and shape of the body.
2. **Viscous Drag** - Viscous and shear forces (τ_w) dominate over inertial forces near the wall inside the formed boundary layer. This results in an additional and dominant viscous drag, which acts over the entire surface in contact with the fluid. When a fluid travels over a body, the fluid in contact with the surface experiences shear stress, which results in a momentum transfer from the fluid medium to the body. This transfer of momentum generates a net force that opposes the body's motion, known as viscous drag. Viscous drag is affected by numerous variables, including the body's speed, shape, and size. However, the viscous drag coefficient remains relatively constant over a small range of Reynolds numbers.

Generally, viscous drag is often dominant over pressure drag for more streamlined bodies moving at moderate speeds in a fluid medium. This is mainly because viscous drag depends on the fluid's viscosity, the surface area, and the roughness of the body. In contrast, pressure drag is more dominant for blunt and larger bluff bodies moving at higher speeds in a fluid medium. Pressure and viscous drag are usually considered separately to accurately estimate the total drag force. However, this is partially true for turbulent flows, as both pressure and viscous effects are interdependent and complex to separate.

In a turbulent boundary layer (TBL) of an aircraft, viscous drag is dominant as the turbulence near the wall inside the TBL greatly enhances the shear stresses and frictional forces. This is because the fluid velocity fluctuates rapidly and unpredictably, leading to higher shear. For any aircraft, viscous drag significantly contributes to overall drag, accounting for up to 50% of total drag as visualized in Figure 1.2. Additionally, considerable research has already been conducted on reducing induced drag and form drag through winglets, raked wingtips, etc. Comparatively, viscous drag reduction is a relatively uncharted and promising field, creating interest for future investigations.

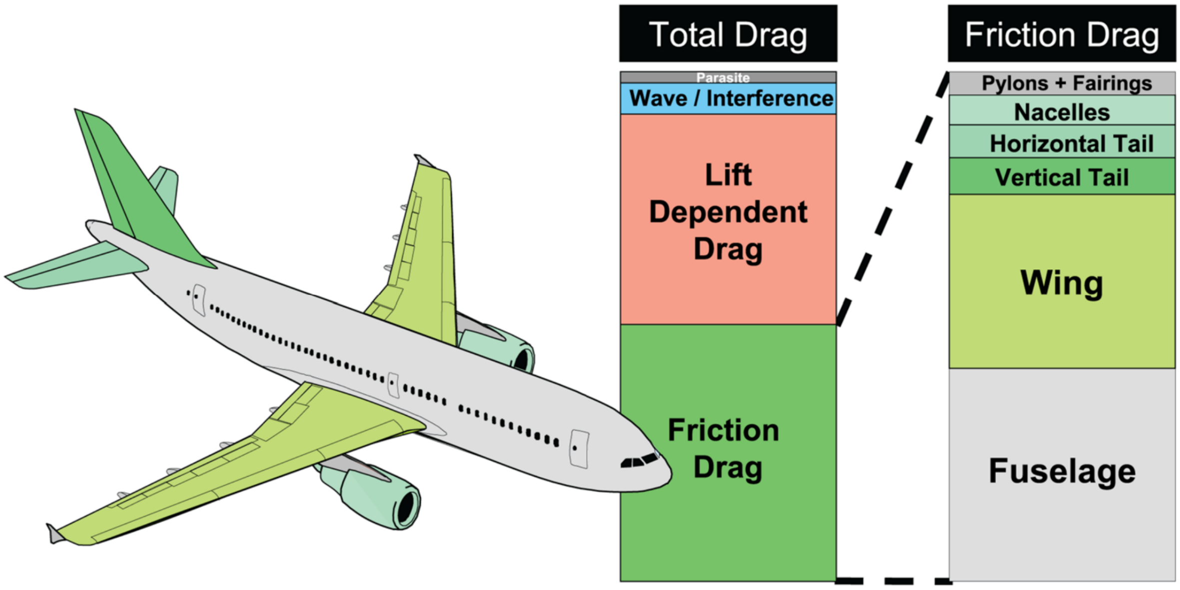

Figure 1.2: A typical distribution of the overall drag contribution for an A320 aircraft, as presented by Kornilov, 2021.

Reducing viscous drag will eventually lead to more sustainable aviation practices and reduced operational costs. Developing effective viscous drag reduction strategies that reduce frictional forces and shear stress between the fluid and the aircraft surface is essential for enhancing the overall fuel efficiency of an aircraft. Moreover, as demand for air travel has increased, the need for efficient and sustainable aviation technology has become more critical than ever. Inside a TBL, the presence of multiple spatiotemporal scales makes it a complicated and unpredictable phenomenon. However, despite its apparent randomness, it has been observed that turbulence exhibits a degree of coherence [Theodorsen, 1955; Robinson, 1991]. The tendency of flow structures to persist and travel together for a certain distance or time is called coherence. Additionally, the coherence can be linked to nonlinear interactions between fluid elements, creating self-organizing patterns.

The two basic control mechanisms used to affect the fluid flow behavior are active and passive control systems. Passive control systems are non-powered and employ stationary flow features that change the dynamics of TBL. Passive control techniques comprise riblets, vortex generators, and other methods. On the other hand, active flow control systems are powered and use active devices such as sensors and actuators with a control algorithm. This active control technique dynamically changes the flow properties near the wall by manipulating certain spatiotemporal scales. Therefore, it is often seen as superior and far more efficient due to its greater control authority. Additionally, active control can adapt to varying conditions and optimize system performance either in real-time or through a predetermined approach, making this control technique more adaptable and versatile [Ghaemi, 2020]. As a result, active control strategies are gaining popularity in fluid mechanics research and viscous drag reduction. This motivates the research to look into active control as an exciting and evolving field with many open research questions and practical applications.

An active control technique can further be classified into open and closed-loop control. Open loop control refers to an active control technique where the input or control actions are solely based on the pre-determined set of flow conditions and are made without considering dynamic changes in fluid flow. In contrast, closed-loop control can adapt to changing flow conditions and disturbances. As the feedback signal modifies the control mechanism based on the desired control effect, closed active control systems are employed for more precise control. However, open-loop active control is better for instances where the flow behavior can be predicted. Additionally, open-loop control is typically more cost-efficient and simple than closed-loop control. Given the trade-off between effectiveness and ease of implementation, open-loop active control was selected for this thesis work.

1.1. Motivation

In the past, most research on active control techniques focused on decreasing the energy dissipation associated with near-wall small-scale turbulence. However, small-scale control techniques face limitations at higher Reynolds number flow due to the increased oscillating frequency (f^+_{osc}) of near-wall small scales. In contrast, the efficacy of an active control strategy tuned to the outer layer large-scale at higher Reynolds number flows has emerged as a promising avenue for achieving significant drag reduction [Talluru, 2014]. However, most of the previous literature targeting the large energetic scales achieved drag reduction either through a random actuation frequency or actuation frequency limited by the hardware of the experimental set-up.

Various active flow control techniques have been developed, such as wall oscillation, pulsating synthetic jets, continuous blowing, and suction. Many authors have studied synthetic jets such as Spinosa and Zhong, 2017 for analyzing the effect of injection and suction through a slit. However, synthetic jets faces limitations regarding large-scale actuation in a TBL. Synthetic jets lack higher actuation amplitude which limits the interaction with large-scale structures. Sano and Hirayama, 1985 first conducted an experimental study to analyze the influence of injection and suction separately using a blower. They concluded that injection reduced the eddy scales, whereas suction increased them. Additionally, the blowing techniques exert a greater amount of control authority for both inner scale control [Chen, 2019; Zhang et al., 2022] and for outer scale control [Talluru, 2014]. Sano and Hirayama, 1985 also concluded that suction decreases the shape factor and increases the skin friction coefficient. Considering these factors, blowing emerges as the actuation technique that affects large eddies over more considerable streamwise distances. Later Antonia et al., 1995 also concluded that blowing techniques reduce the turbulent eddies' size. In contrast, suction can remove already-formed turbulence and promote the formation of a laminar boundary layer (only seen for lower Re_τ). These findings have led to discarding active suction in favor of active blowing as a more promising technique for reducing drag in TBL.

Talluru, 2014 examined the usefulness of wall-normal jet tuned to the coherent frequency of the large-scale motions (LSMs) in TBL and determined that the jet targeting outer LSMs reaches the logarithmic region of the boundary layer and weakens these LSMs. However, even though Talluru, 2014 introduced a novel approach for assessing and concentrating on energetic LSMs, his work lacked a comparison of near-wall small-scale forcing and outer-wall large-scale forcing in terms of efficiency. Later, Marusic et al., 2021 shed light on the contributions of LSMs to the overall wall shear stress in turbulent boundary layers and how this contribution increases with the Reynolds number. By analyzing high-resolution experimental data of wall-bounded turbulent flows over a broad range of Reynolds numbers, Marusic et al., 2021 demonstrated that the larger eddies in the flow have a more significant influence than previously believed in the total wall shear stress. Specifically, they discovered that the contribution of larger eddies to the wall shear stress grows with the Reynolds number and that, at high Reynolds numbers, this contribution is significant to the contribution of smaller eddies. The underlying principle behind drag reduction via wall oscillation, as observed by Marusic et al., 2021, is based on the creation of streamwise vortices in a controlled manner to attenuate large energetic scales. The wall oscillation control technique tuned to the dominant frequency of large scales resulted in maximum drag reduction. Therefore choosing a large-scale active flow control technique can be strongly motivated for several underlying reasons:

1. Large scales are frequently the dominant structures in turbulent flows, and altering these structures can significantly affect the flow's overall behavior.
2. As large-scale active flow control techniques target the most energetic flow structures, they can be easier to target and more effective in reducing drag.
3. Active flow control approaches targeted to large scales may be simpler to construct and less energy expensive than techniques that target smaller scales.

Utilizing an array of wall-normal blowing jets instead of a single jet offers several advantages in the performance of the active flow control techniques, including increased adaptability and efficiency in actively manipulating large-scale structures convecting in the turbulent boundary layer. In addition, employing numerous jet slits can achieve a more spatially distributed actuation control, allowing for a more effective alteration of flow structures across various length scales. Furthermore, an array of jets also provides a higher degree of redundancy, improving the control system's resilience to failures. To reduce drag in a TBL, spanwise wall oscillation and spanwise traveling wave actuation from multiple spanwise arranged wall-normal jets share an identical principle. They both intend to manipulate the large-scale structures convecting in the flow by introducing periodic disturbances. These perturbations have a negative effect on the energetic large scales. In spanwise wall oscillation, the wall itself oscillates periodically, regularizing eddies that counteract large-scale turbulent fluctuations and reduce skin friction drag. In contrast, spanwise traveling wave actuation is implemented with an array of multiple wall-normal jets. Controlling the actuation timing and amplitude of the jets generates a spanwise shear that replicates the wall oscillation and produces similar drag-reduction effects. In real-world circumstances, the spanwise traveling wave actuation using multiple spanwise arranged wall-normal jets is deemed more practical than wall oscillation. This is primarily due to the fact that spanwise traveling wave actuated from jets does not require moving components or complex mechanical systems to oscillate the wall, which could be difficult to implement and maintain in real-world applications such as aircraft surfaces. Instead, wall-normal nozzles are more easily controlled and adjustable, allowing for a more practicable approach to active flow control techniques for drag reduction. Moreover, by utilizing the existing compressed air supply, the implementation of spanwise traveling waves by the wall-normal jet array becomes less demanding in terms of additional infrastructure or resources, thereby increasing its appeal for real-world applications.

1.2. Research Objective and Research Questions Addressed

This report answers the following research questions based on the takeaways from the literature review and previous experimental campaign results.

1. What is the organization of the dominant flow structures within a turbulent boundary layer?
    (a) How do they contribute to the momentum and energy transfer in the flow?
    (b) What changes in the flow dynamics and individual flow features when a TBL develops at higher Reynolds numbers?
    (c) How do the large-scale structures interact with the small-scale structures in TBL?
2. What are the existing flow control techniques for drag reduction in a TBL?
    (a) What are the key drag reduction mechanisms for each passive and active control method, and how effective are they in practice?
    (b) What are the limitations of each method in terms of efficiency and practical implementation?
    (c) What are the limitations of existing flow control techniques?
    (d) How can the different active control methods be combined and optimized to achieve more effective drag reduction, and what are the challenges associated with such hybrid approaches?
3. How can an array of wall-normal jets be designed and tuned to LSMs convecting in the logarithmic region of a TBL?
    (a) What are the trade-offs between a 2-dimensional forcing technique, such as a wavy wall with normal wall deformation, a spanwise wall oscillation, and a 1-dimensional spanwise forcing via an array of multiple wall-normal jets to introduce coherent streamwise patterns?
    (b) What are the optimal actuation parameters for large-scale manipulation?
    (c) How does this actuation technique be scaled to a real-world full-size aircraft?
4. How does the suggested active control technique influence the incoming TBL?
    (a) How do different tuning strategies affect the 1^{st} and 2^{nd} order turbulence statistics of a TBL?
    (b) Does different methods of jet actuation (standing wave vs traveling wave) result in different flow control effectiveness, even when the actuation frequency remains the same?
    (c) Is there a noticeable difference in second-order turbulence statistics for different control cases far downstream of the actuation plate?
    (d) How are the LSMs organized in the logarithmic region, and do the control cases cause any differences in their intensity and organization?
    (e) Can a drag reduction potential be established for any of the suggested control cases?

The structure of this report is organized as follows. First, chapter 2 addresses the principles and composition of TBLs and reviews the literature on the formation and characteristics of near-wall small scales and outer-wall large scales. Next, chapter 3 examines existing literature on passive and active TBL control techniques. The experimental methodology and setup employed in the campaign are explained in chapter 4. In Chapter 5, various flow measurement techniques used to assess the effectiveness of different control cases are discussed. The findings from these measurement techniques are analyzed in detail in chapter 6. Finally, chapter 7 reviews and concludes the results, followed by future recommendations in chapter 8.

2

Boundary Layer Turbulence

This chapter delves into boundary layer theory's fundamental principles, formation, and development. Turbulence can be classified into two types: free shear turbulence and wall-bounded turbulence. Wall-bounded turbulence can be divided into internal flows, which occur through pipes or ducts, and external flows, which occur over surfaces such as an aircraft fuselage or a ship's hull. The three major canonical flows are characterized by mean velocities parallel to the surface and involve fully developed flows over a flat plate, inside a pipe flow, and within a channel flow [Buschmann and Gad-El-Hak, 2006]. This chapter reviews turbulent boundary layers and their associated flow structures over a flat plate in detail.

2.1. Turbulent Boundary Layer Over A Flat Plate

The boundary layer can be defined as a thin layer of fluid flow near a wall where the velocity is zero at the wall (referred to as a no-slip condition) and increases to the free-stream velocity near the edge of the boundary layer. This boundary layer can be laminar or turbulent depending on the Reynolds number. A laminar flow is defined as a fluid flow that is smooth and uniform, with fluid particles moving in parallel layers (also known as "lamina") without mixing. This flow is predictable. Each lamina has a slightly distinct velocity, with the highest velocity at the upper edge and decreasing velocity as it approaches the wall. As a result, momentum transfer occurs between these laminae as they move past one another. Turbulent flow, on the other hand, is characterized by chaotic and irregular motions. The velocity of fluid particles varies rapidly and randomly in a turbulent flow. The turbulent flow mainly occurs at a high Reynolds number. Turbulent flow is an essential research topic in fluid mechanics due to its prevalence in many real-world scenarios.

The Reynolds number is defined as the ratio of inertial forces to viscous forces. This is a non-dimensional number that determines the state of the boundary layer and can be expressed as:

$$Re_x = \frac{u_\infty \cdot x}{\nu} \tag{2.1}$$

Here x is the streamwise distance from the plate's leading edge, ν is the kinematic viscosity of the fluid, and u_∞ is the free stream velocity. The flow is laminar at a lower Reynolds number, and the viscous forces are dominant for laminar flows. As the Reynolds number increases, the contribution of inertial forces increases and they become dominant, making the flow more chaotic and turbulent. This transition is not sudden but gradual and depends on several factors, such as the body's shape, fluid properties, and flow velocity. The flow changes from laminar to turbulent at the critical Reynolds number of $Re_x = 3 \cdot 10^5 - 5 \cdot 10^5$ on a typical fuselage of an aircraft. The Reynolds number can also be defined in terms of boundary layer thickness(δ) and frictional velocity(u_τ) as:

$$Re_\tau = \frac{u_\tau \cdot \delta}{\nu} \tag{2.2}$$

Here the friction velocity (u_τ) is given as $u_\tau = \sqrt{\frac{\tau_w}{\rho}}$. The shape of a typical wall-bounded flow can be visualized in Figure 2.1. As depicted, the turbulent boundary starts developing from the right and forms a boundary layer of thickness $\delta(x)$. The pressure gradient($\frac{dP_\infty}{dx}$) can be defined as the measure of change in pressure along the surface of the flat plate due to the motion of the fluid particles. The Bernoulli principle determines this and describes the behavior of the fluid flow. This is given as:

$$\frac{dP_\infty}{dx} = -\rho U_\infty \frac{du_\infty}{dx} \tag{2.3}$$

The variable ($\frac{dP_\infty}{dx}$) can determine the nature of the flow. For a boundary layer with a zero pressure gradient (ZPG), the pressure remains constant along the streamwise direction, and there is no flow acceleration downstream of the test section. A negative pressure gradient develops downstream of the test section for accelerating flows, also known as a favorable pressure gradient (FPG). In contrast, a positive pressure gradient appears downstream of the test section for an adverse pressure gradient (APG) case. For APG, the flow decelerates and eventually separates from the surface. However, since most skin friction originates from the fuselage of an aircraft, which represents a ZPG, this report will primarily focus on ZPG.

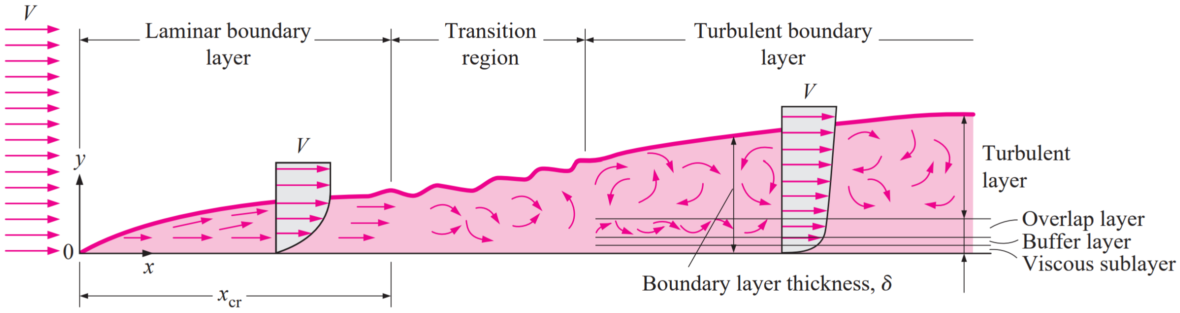

Figure 2.1: Development of a boundary layer on a flat plate, as illustrated by Cengel, 2010.

The wall shear stress is defined as the force per unit area that is applied by the fluid when it is in contact with the surface. As per the no-slip condition, the velocity of fluid particles at the wall is zero. This is due to the effects of viscosity and friction. The wall shear stress can be calculated using the following formula:

$$\tau_w = \mu \left(\frac{\partial \bar{u}}{\partial y} \right)_{y=0} \tag{2.4}$$

Here τ_w represents the shear stress at the wall ($y = 0$), μ is the fluid property known as dynamic viscosity, and $\frac{\partial \bar{u}}{\partial y}$ is the velocity gradient.

The boundary layer formed on any component of an aircraft is predominantly turbulent through the flight regime. Hence, reducing this turbulent skin friction drag will result in more efficient aircraft design, making this an active area of research. The primary objective of this chapter is to increase the knowledge of the underlying mechanisms that generate turbulence in fluid flow and to investigate the interaction between the energetic large scales in the outer-layer and the near-wall small scales that causes friction and wall shear.

To better understand the boundary layer, a few key parameters are discussed in detail before going through existing literature:

1. **Boundary Layer Thickness (δ):** The boundary layer thickness is the wall-normal distance between the point at the wall where the velocity is zero and the point at the boundary layer's edge where the velocity is equal to the freestream velocity (u_∞). In a boundary layer, viscous forces are most dominant at the wall and decrease until it is negligible away from the wall. As the wall-normal distance increases, fluid velocity increases and the viscous forces' effect decreases, making inertial forces dominant. This behavior forms a log region where the velocity profile behaves logarithmically with increasing wall-normal distance. The free stream Reynolds number (Re_x) can express the boundary layer thickness for any flat plate with a TBL [Schlichting and Gersten, 2016]. This formula is derived under several conditions such as: *(1)* the boundary layer

behaves geometrically similarly in x, meaning the velocity and pressure profile are similar through the streamwise direction. *(2)*. The flow is turbulent from the beginning of the boundary layer formation. Even though these assumptions have limitations in real-life, this formulation very well approximates the boundary layer thickness.

$$\delta(x) \approx \frac{0.37 \cdot x}{Re_x^{1/5}} \tag{2.5}$$

2. **Displacement Thickness (δ^*):** The distance that the wall or surface must be moved perpendicular to the initial wall position in an inviscid flow to compensate for the mass flux deficit caused by the formation of a boundary layer.

$$\delta^* = \int_0^\delta \left(1 - \frac{u(y)}{u_\infty}\right) dy \tag{2.6}$$

3. **Momentum Thickness (θ):** The distance that the wall or surface must be moved perpendicular to the wall in an inviscid flow to compensate for the momentum flux deficit caused by the formation of a boundary layer.

$$\theta = \int_0^\delta \frac{u(y)}{u_\infty} \left(1 - \frac{u(y)}{u_\infty}\right) dy \tag{2.7}$$

4. **Viscous Length Scale (l^*) and Time Scale** (t^*)**:** The near-wall small scales are defined in terms of the viscous length scale as:

$$l^* = \frac{\nu}{u_\tau} \tag{2.8}$$

On the other hand, the energetic large scales of the outer layer are in the order multiples of the boundary layer thickness (δ). Equation 2.2 can be re-written in terms of boundary layer thickness (δ) and the viscous length scale (l^*) as:

$$Re_\tau = \frac{\delta}{l^*} \tag{2.9}$$

Similarly, a time scale (t^*) is defined as:

$$t^* = \frac{\nu}{u_\tau^2} \tag{2.10}$$

The streamwise evolution of the integral momentum thickness can be used as a surrogate for the trend in skin friction because it is closely related to the momentum exchange in the TBL. When the integral momentum thickness increases, momentum transfer between the fluid and the wall increases, increasing wall shear stress and skin-friction drag and vice-versa.

2.2. Composition And Scaling of Turbulent Boundary Layer

A turbulent boundary layer can broadly be classified into two different regions as:

1. **Inner Layer ($\frac{y}{\delta} < 0.1$):** Inside the inner layer, the viscous and molecular shear forces are predominant. Hence the mean velocity in streamwise direction ($\bar{u}$) depends on wall shear stress (τ_w), density (ρ), dynamic viscosity (μ) and wall-normal distance (y). Initially, close to the wall, the velocity profile is linear, but as the distance from the wall increases, it transitions to logarithmic behavior. The mean velocity within this region is expressed as:

$$u^+ = f(y)^+ \tag{2.11}$$

2. **Outer Layer ($\frac{y}{\delta} > 0.2$):** For an outer layer, the turbulent or the eddy shear forces are dominant, and viscous shear stress can be neglected. The mean velocity in the streamwise direction is given by velocity deficit law ($u_\infty - \bar{u}$). It depends on the wall shear stress (u_τ), density (ρ), free stream velocity (u_∞), boundary layer thickness (δ), wall-normal distance (y) and pressure gradient in streamwise direction ($\frac{dP_\infty}{dx}$). The mean velocity inside this region is given by:

$$\frac{u_\infty - \bar{u}}{u_\tau} = g\left(\eta, \xi\right) \tag{2.12}$$

Where $\eta = \frac{y}{\delta}$ and ξ is a function of the streamwise pressure gradient.

3. **Overlap Region ($0.1 \leq \frac{y}{\delta} \leq 0.2$):** This region forms in between the inner and outer layer and can be scaled using both inner layer variables and outer layer variables.

As the boundary layer falls under the similarity flow regime, spatial dimension and velocity can be scaled by inner and outer region variables. For the inner region, scaling is done with viscous length scales (l^*) and friction velocities (u_τ). Consequently, the scaling for these variables is as follows::

$$\begin{aligned} y^+ &= \frac{y \cdot u_\tau}{\nu} \\ u^+ &= \frac{u}{u_\tau} \end{aligned} \tag{2.13}$$

Whereas for outer layer region scaling, δ is used to measure the ratio of the overall boundary layer thickness (y/δ), and u_∞ is used to normalize the velocity deficit ($u_\infty - \bar{u}$).

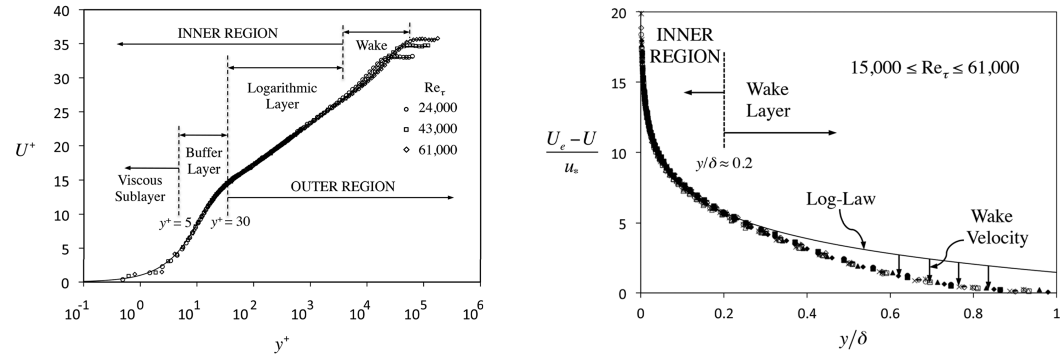

(a) Mean velocity profile scaled with inner variables of a TBL over a flat plate. **(b)** Mean velocity profile scaled with outer variables of a TBL over a flat plate.

Figure 2.2: Experimental data representation of mean velocity profiles at various Re_τ, showcasing the universal nature of velocity profiles, as presented by Perlin et al., 2016.

The inner layer and outer layer region can further be subdivided based on the non-dimensional wall units (y^+) as:

1. **Viscous Sublayer ($y^+ < 5$):** This layer is present adjacent to the wall, where the velocity varies linearly with wall-normal distance. As a result, the thickness of the region is small and can be visualized in Figure 2.1. According to the law of the wall:

$$u^+ = y^+ \tag{2.14}$$

2. **Buffer Layer ($5 < y^+ < 30$):** This is an intermediate layer between the viscous sublayer and logarithmic layer. The velocity profile in this region is neither linear nor logarithmic.
3. **Logarithmic Layer ($30 < y^+ < 0.2\delta^+$):** This forms the overlap between the inner and the outer layer discussed earlier. The velocity profile exhibits a logarithmic profile, and the formulation is given as log law:

$$u^+ = \frac{1}{\kappa} ln(y^+) + B \tag{2.15}$$

   Here κ and B are the Von Karman constant and universal constant respectively. These variables are found out by experiments. Approximately $\kappa \approx 0.41$ and $B \approx 5$ [Pope, 2000; Chauhan et al., 2009].
4. **Wake ($y^+ > 0.2\delta^+$):** The wake region spans for approximately 80% of the whole boundary layer thickness. In this region, the velocity profile strongly depends on the streamwise pressure gradient ($\frac{dP_\infty}{dx}$). The mean velocity profile in this region deviates from logarithmic behavior and hence is scaled mostly using the outer layer variables. The velocity defect law for this region can be written as:

$$\frac{u_\infty - \bar{u}}{u_\tau} = -\frac{1}{\kappa} ln\frac{y}{\delta} + A(\xi) \tag{2.16}$$

Where A is a constant and depends on the external flow conditions such as streamwise pressure gradient. For a zero pressure gradient boundary layer, the velocity defect equation is written as:

$$\frac{u_\infty - \bar{u}}{u_\tau} = \frac{1}{\kappa}\left(-\ln\left(\frac{y}{\delta}\right) + \Pi\left[2 - w\left(\frac{y}{\delta}\right)\right]\right) \tag{2.17}$$

Here $w\left(\frac{y}{\delta}\right)$ is defined from the wake function satisfying $w(0) = 0$ and $w(1) = 1$ and π is approximately equal to 0.44 and is known as wake strength parameter as given by Chauhan et al., 2009.

The boundary layer profile is universal overall and does not entirely depend on the Re_τ. This boundary layer velocity profile independence from Re_τ can be visualized from Figure 2.2a.

2.3. Turbulent Cascade And Production

Turbulent velocity fluctuations have a substantial effect on the dynamics of a TBL. The instantaneous turbulent fluctuation velocity is the difference between the instantaneous and the average velocity. This decomposition process is known as Reynolds decomposition and can be written as:

$$u'(t) = u(t) - \bar{u} \tag{2.18}$$

The fluctuating turbulent velocity component captures the flow's chaotic behavior and plays a significant role in turbulent kinetic energy transport. Richadson, 1922 proposed the idea of energy contained in large-scale turbulent eddies and is transferred to smaller eddies until the energy is dissipated by the smallest eddies (Kolmogorov length scale). He theorized that turbulence cascade is self-similar; hence, statistical properties of the flow are scale invariant. As the energy gets transferred, the eddies' length and velocity scales decrease; however, the statistical property of the flow remains constant. Ultimately, the energy gets dissipated as heat due to viscosity.

As turbulent flows are highly non-linear, the turbulent velocity fluctuation component can be characterized in terms of statistical property to express Reynolds stress (RSS) tensors. The (RSS) tensor is a second-order tensor representing the anisotropic contributions of stress due to turbulent fluctuations. The major components of the RSS tensor are $< u'u' >$, $< v'v' >$ and $< u'v' >$. These quantities represent the Reynolds stresses in streamwise (x), wall-normal (y) direction, and shear stresses respectively. A detailed overview of these RSS is plotted in Figure 2.3. As visualized from Figure 2.3, the inner peak at $y^+ = 15$ for streamwise turbulent velocity fluctuation exhibits the location of maximum turbulence production. As RSS is derived from the product of different fluctuating velocity components, the $y^+ = 15$ corresponds to the highest RSS and steepest velocity gradient. At this region, the energy transferred from the mean flow to the turbulence is the highest, leading to the generation and maintenance of turbulent structures [Pope, 2000].

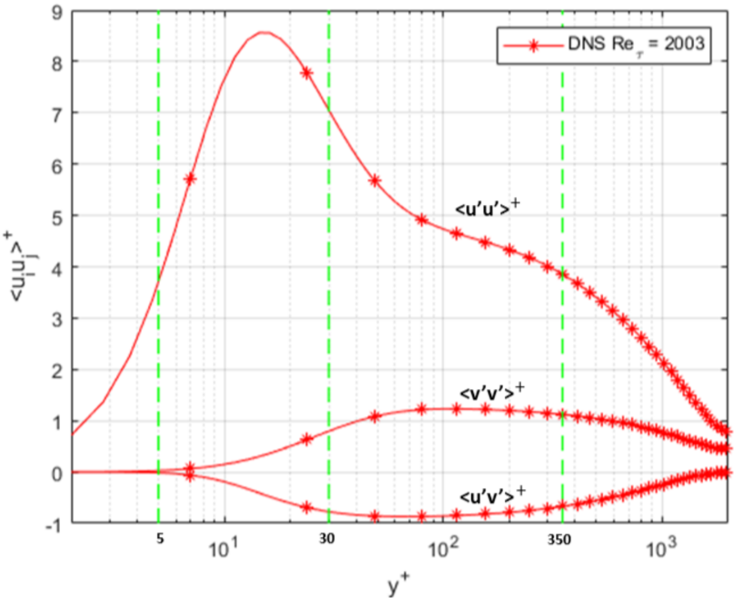

Figure 2.3: Reynolds stress budget constructed from data provided by Hoyas and Jiménez, 2008 for a channel flow.

Turbulent kinetic energy (TKE) is a fundamental quantity that characterizes the intensity of turbulence in a fluid flow. The TKE can be expressed in terms of the RSS tensors. The diagonal terms of the RSS tensors represent the individual contributions of the three turbulent velocity fluctuation components. However, The off-diagonal terms of the Reynolds stress (RSS) tensors represent the anisotropic behavior and the interaction between the turbulent velocity fluctuation components. Using the Reynolds decomposition, the TKE can be expressed as:

$$TKE = \frac{1}{2}(u'^2 + v'^2 + w'^2) = \frac{1}{2}(u_i u_i - \overline{u_i u_i}) \tag{2.19}$$

The TKE production (P) signifies the TKE produced by the interaction of turbulent fluctuations in the streamwise (u') and wall-normal (v') directions with the mean shear $(\frac{du}{dy})$ of the flow. The variable P quantifies the energy transfer from the mean flow to turbulent fluctuations and is essential to the turbulent energy cascade.

$$P = -\frac{\partial \bar{u}}{\partial y}\overline{u'v'} \tag{2.20}$$

This relation is derived using the Reynolds-Averaged Naiver-Stokes equation for an incompressible turbulent flow. This derivation assumes the flow to be in a steady state with homogeneous turbulence for a plat plate [Pope, 2000]. The derivative $\frac{\partial \bar{u}}{\partial y}$ represents the spatial variation of mean streamwise velocity in the wall-normal direction. Understanding TKE production in turbulent flows requires understanding the generation of Reynolds shear stress (RSS) and wall-normal velocity gradient. The integral of P over the whole boundary layer thickness measures the bulk production of TKE (B_{TKE}). This represents the rate at which TKE is generated inside the boundary layer.

$$B_{TKE} = \int_0^\delta P dy \tag{2.21}$$

The wall shear stress (τ_w) can be related to the coefficient of friction by the following relationship:

$$C_f = \frac{\tau_w}{\frac{1}{2}\rho U^2} \tag{2.22}$$

Although P and C_f are not directly proportional, they both are related to the wall shear stress. Therefore, changes in the production of TKE can affect skin friction drag. Additionally, the ejection event (combining negative streamwise velocity fluctuations and positive wall-normal fluctuations) and sweep event (combining positive streamwise velocity fluctuations and negative wall-normal fluctuations) result in positive TKE production, accounting for 70% of shear stress ($< u'v' >$). To reduce viscous drag, either the near wall events such as ejection and sweep can be suppressed, thereby reducing the shear stress, or the energy of the larger length scales can be decreased, which directly influences the near wall scales via different interaction processes.

2.4. Flow Structures In A Turbulent Boundary Layer

Coherence motion is highly correlated over at least one fluid property over a temporal or spatial domain that is significantly larger than the length scale of its smallest scale in the flow and is not restricted to geometric size [Kline and Robinson, 1990)]. Kline and Robinson, 1990 proposed eight different classes of coherent structures based on their geometry, kinematics, and underlying physical mechanisms. Later, Smits et al., 2011 classified them into more concise groups based on their principle timescale characterization (eddy-life cycle) as follows:

1. QSVs (Quasi-streamwise vortices) near the wall [Kline et al., 1967] having long lifespan in order of several minutes.
2. Hairpin vortices that exist 100 viscous wall units away from the wall [Perry and Chong, 2022] [Theodorsen, 1955].
3. LSMs (Large Scale Motion) in the log region of a turbulent boundary layer [Kim and Adrian, 1999] and believed to play a critical role in the transport of momentum and energy in turbulent flows.
4. VLSMs (Very Large Scale Motions) populating the log region of the turbulent boundary layer [Kim and Adrian, 1999] and playing a crucial role in the organization of turbulent atmospheric structures.

2.4.1. Instantaneous Flow Structures Near The Wall And Hairpin Vortices

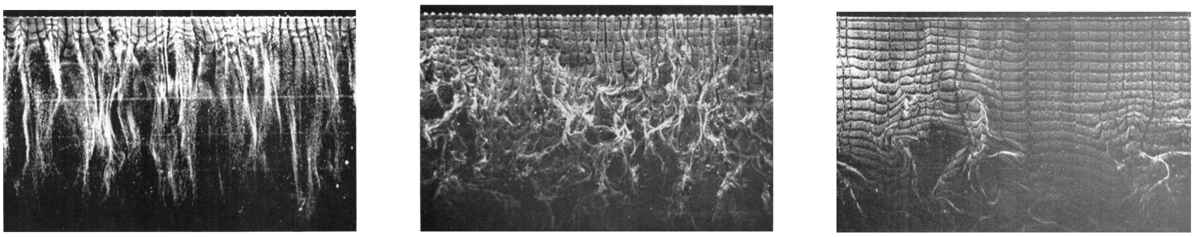

(a) $y^+ = 2.7$ **(b)** $y^+ = 101$ **(c)** $y^+ = 407$

Figure 2.4: Snap-shorts of low-speed ejection (Q4) event seen near the wall at different wall-normal positions as presented by [Kline et al., 1967].

Kline et al., 1967 captured the streakiness of the near-wall structure through the first-ever TBL flow visualization utilizing the hydrogen bubbles technique (as visualized in Figure 2.4). They stated that the streaks are lifted and stretched near the wall in a TBL. Therefore, these structures can be modeled and reproduced using the 'lifted vortex element' as visualized in Figure 2.5. In addition, Kline et al., 1967 stated that the assembled regions grow in size and move away from the wall at a particular angle and speed. After combining the results from hydrogen bubble visualization and Hot-Wire Anemometry (HWA), they concluded that the streaks lift and oscillate away from the wall. These streaks burst and grow away in the boundary layer through vortex induction. Later, Smith, 1983 renamed this phenomenon as Quasi-Streamwise Vortices(QSVs), which exhibited cyclic behavior and regenerated in the viscous sub-layer region with a spanwise spacing of 100 wall units. QSVs play an important role in the self-sustaining mechanism of turbulence and in transporting turbulence away from the wall and into higher regions of the boundary layer.

Sweep was introduced by Corino and Brodkey, 1965 and linked with the ejection of fluid away from the wall by pushing high-velocity fluid toward the wall to satisfy the continuity condition. The low-speed streaks ejected from the wall contribute to approximately 50% of turbulence production. The interaction between this high-velocity sweep streak and the low-velocity ejected streak creates an inclined shear layer near the wall. The quadrant splitting method introduced the ejection as (Q2) and sweep as (Q4) events contributes to Reynolds shear stress (RSS) [Wallace et al., 2022]. The maximum turbulence production is at $y^+ = 15$. The interaction between the Q2 and Q4 events causes the Q1 and Q3 event, which accounts for negative 20% RSS each. Using multiple flow visualization techniques such as dye and hydrogen bubble, Offen and Kline, 1974 discovered that these low-speed streaks ejecting from the wall eventually induce the wall-ward sweep of high-speed streaks in the near wall region ($20 < y^+ < 200$), thereby creating a mechanism of periodic burst-sweep in the shear layer.

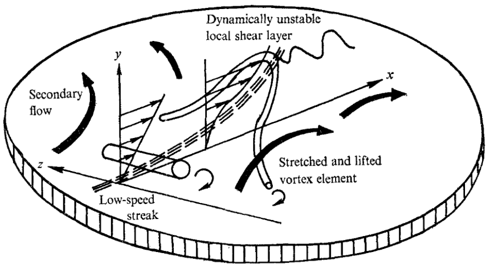

Figure 2.5: The streak break up mechanism as produced by [Offen and Kline, 1974].

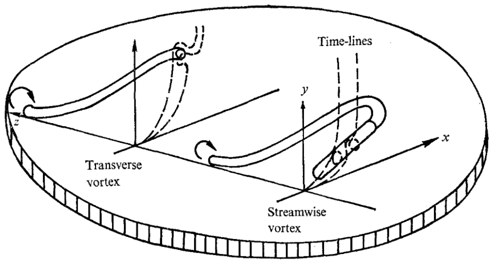

Figure 2.6: Timeline of stretched and lifted vortex element from the wall at different locations as produced by [Offen and Kline, 1974].

Praturi and Brodkey, 1978 stated that vortical structures roll the free-stream flow into a bulge in the boundary layer, thereby accelerating and initiating the regenerative or cyclical process of sweep and ejection. Later, Nychast et al., 2022 also suggested that the interaction between the alternative patterns of high-speed and low-speed structures creates a transverse vortical structure expanding from the wall to the outer region.

While the origin and cause of turbulence production and the self-sustaining cycle are the subjects of debate, the literature described thus far can be divided into two categories.

1. One in which ejection and sweep trigger self-sustained turbulent production [Kline and Robinson, 1990; Kline et al., 1967; Offen and Kline, 1974; Offen and Kline, 2022; Kim and Adrian, 1999].
2. The other in which the transverse vortex is believed to be primarily responsible for the turbulence production and regeneration cycle [Praturi and Brodkey, 1978; Nychast et al., 2022].

The vortex filament that transports the TKE from the region adjacent to the wall to the outer region acts as a conduit between QSVs and transverse vortices. QSVs are elongated, streamwise-oriented structures that maintain large-scale patterns in turbulent flows. In contrast, transverse vortices are structures with a cross-flow orientation responsible for mixing the fluid. Theodorsen, 1955 conceptualized the hairpin vortex filament, which is shaped like a ”tornado” and begins to grow from the wall at 45^o angle. As the Reynolds number increases, these cohesion structures stretch and transform a simple vortex loop to a hairpin vortex as visualized in Figure 2.8. The growth of these hairpin vortices is accompanied by stretching and tilting of vortex legs that form the hairpin shape. Understanding the development and evolution of turbulence in wall-bounded flows primarily depends on the hairpin vortex filament. These hairpin structures contribute significantly to the production and transport of turbulent kinetic energy through their expansion and transformation.

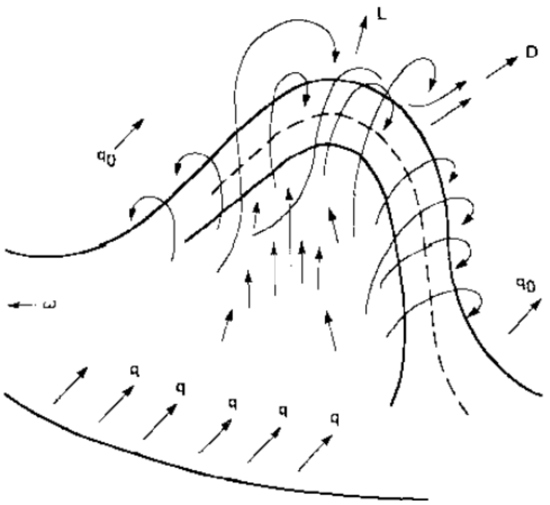

Figure 2.7: Hairpin Vortex as conceptualised by Theodorsen, 1955.

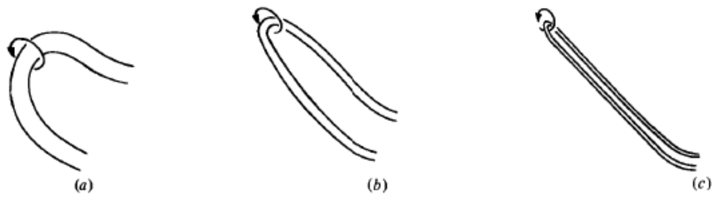

Figure 2.8: Reynolds number effect on the formed hairpin vortex as viewed by (Theodorsen, 1955) (a) Very low Re - Vortex loops; (b) Low-moderate Re - Elongated loops or Horseshoe; (c) Moderate-high Re - Elongated hairpins or vortex pairs[Theodorsen, 1955].

Even though the inclination of a single hairpin from the upstream is approximately 45^o, agglomerations of hairpin vortices which form a larger coherent structure, tend to incline at 20^o due to mean shear (as visualized in Figure 2.9). The legs of these hairpin vortices are typically the ear;ier mentioned QSVs close to the wall, which generates the high skin friction event close to the wall.

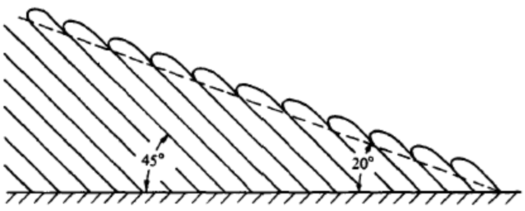

Figure 2.9: A schematic showing individual hairpin vortex inclination and agglomerated hairpin vortices inclination[Head and Bandyopadhyay, 1981].

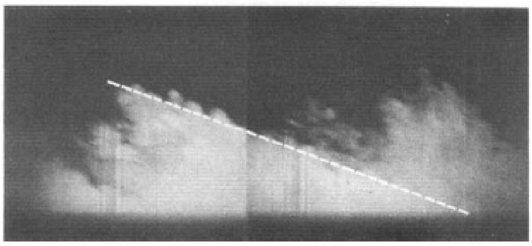

Figure 2.10: Instantaneous snapshot of coherent structure formed by agglomeration of hairpin vortices[Head and Bandyopadhyay, 1981].

Later, Robinson, 1991 concluded all previous research and proposed a new model for the region near the wall in the TBL. He postulated that QSVs play a significant role and dominate the inner region. The legs rise gradually and form an arch that meets at the boundary layer's wake. Later, Adrian et al., 2000 proposed that the arches or heads of these hairpin vortices are formed in the wall-normal plane, specifically at the interface between the turbulent and non-turbulent flow. The arches are oriented in the spanwise direction, and the agglomeration forms a larger domain of arches that forms a three-dimensional bulge at the edge of a TBL with a length scale of boundary layer thickness (δ) as visualized in Figure 2.11. According to Zhou et al., 1999, these hairpins are arranged in the flow direction as packets that extends up to $2 \cdot \delta$ in the streamwise direction and $0.8 \cdot \delta$ in the spanwise direction.

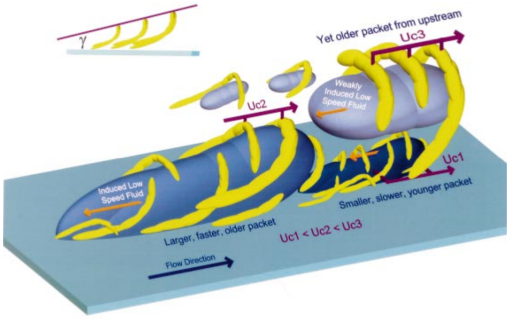

Figure 2.11: Nested packets of the hairpins as conceptualised by [Adrian et al., 2000].

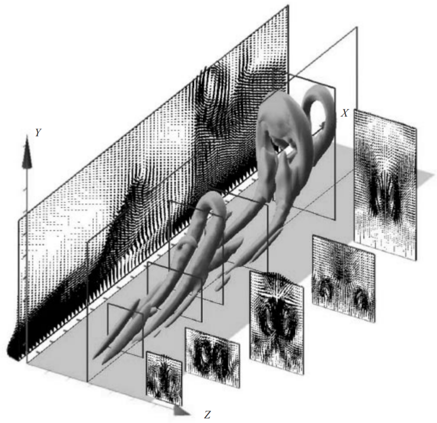

Figure 2.12: Hairpin vortices as computed by [Zhou et al., 1999].

The heads are typically formed in the region just outside the viscous sublayer. As the hairpins are formed near the wall, they significantly impact the flow dynamics. These vortices can transport the mass and momentum from near the wall region to the outer layer of a TBL and contribute to forming larger scales and producing TKE.

2.4.2. Flow Structures and Events In Outer Layer - Large Scale Motions and Very Large Scale Motions

The 3-D bulges discussed earlier have a length scale greater than or equal to δ. The fluid in the streamwise direction of the free stream is convected and entrained into these bulges to form weak rotational eddies just beneath the bulges. When a fluid with a relatively high velocity interacts with the upstream side of these large coherent structures, backward-sloping shear layers with a scale of δ are observed. These shear layers span nearly the entire turbulent boundary layer for flows with low and high Reynolds numbers. Blackwelder and Kovasznay, 1972 determined that the small-scale structures close to the wall are strongly correlated till $y/\delta \approx 0.5$ for the entire domain, indicating the presence of large eddies with extended life-cycles and traveling distances of up to $10 \cdot \delta$ without any identity loss. Meinhart and Adrian, 1995 also noted the presence of large zones with uniform streamwise momentum and irregular shapes in the boundary layers. These were later dubbed Uniform Momentum Zones (UMZ) and resulted from the backflow caused by hairpin packets in the streamwise direction. The association of near-wall burst events with the large scales was also observed by Kline et al., 1967.

Adrian et al., 2000 reported that most low momentum zones exist just above the current low-speed streaks in the buffer layer. Later, Ganapathisubramani et al., 2003 conducted PIV studies to visualize the streamwise and spanwise planes of a TBL and concluded that large-scale momentum regions exist. Furthermore, they observed that these elongated regions are present between the legs of hairpins and that the packets of hairpin vortices carry a substantial amount of RSS, constituting a crucial component of the turbulence transport mechanism. In the spanwise direction, the elongated low momentum structures observed by both Adrian et al., 2000 and Ganapathisubramani et al., 2003 are between $0.3 \cdot \delta$ and $0.5 \cdot \delta$ wide and occur in an alternating pattern. Later, Hutchins and Marusic, 2007a analyzed the length of these structures using an array of HWA in the spanwise direction as visualized in Figure 2.13. The fact that these structures extend up to $20 \cdot \delta$ in the streamwise direction led to their designation as "Superstructures."

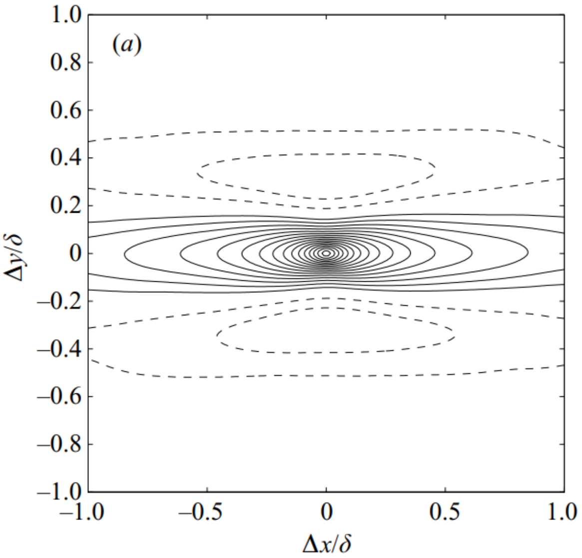

Figure 2.13: Two point correlation of ’u’ fluctuation on the horizontal plane [Hutchins and Marusic, 2007a].

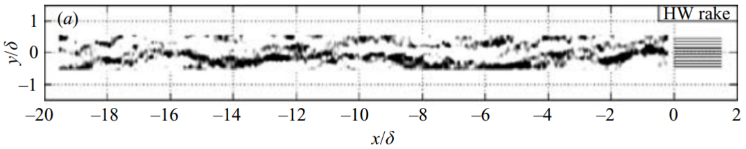

Figure 2.14: Instantaneous snapshot LSMs, indicated by an array of spanwise HWA [Hutchins et al., 2011].

According to Hutchins and Marusic, 2007a, the superstructures, now referred to as LSMs and VLSMs, meander in the spanwise direction and result in an alternate streamwise velocity fluctuation that aligns in the streamwise direction such that the meandering effect obscures the true length in the pre-multiplied energy spectra plots. Later Hutchins et al., 2011 again studied the conditionally averaged u fluctuation (u') and determined the presence of a forward-leaning low-speed structure above a low skin friction event. In addition, they also observed the presence of two high momentum regions on either side of these structures (Figure 2.13).

2.4.3. Interaction Of Large And Very Large Scale Motions With Near Wall Scales

The interaction between LSMs and near-wall scale in a TBL is a topic of active study. Two effects characterize this interaction. One is amplitude modulation, in which the convecting large-scale motion in the log region dynamically amplifies or attenuates the small-scale structures. Using a hot wire in a TBL with a band-pass filtered turbulence signal, Rao and Narasimha, 2022 determined that the characteristic time scale scales with the outer variables (δ and U_∞). It represents the interaction between small scales near the wall and large scales in the outer layer. This amplitude modulation in large scales can also lead to changes in kinetic energy production, kinetic energy transport, and near-wall scale organization. For Superposition modulation, the outer layer’s large-scale structures impose the energy onto the nearby small scales. This explains why the inner peak of $\bar{u}^2$ increases as the Reynolds number increases (see Figure 2.16). The low-frequency motion of the outer layer’s large scales contributes additional energy to the nearby small scales. According to Hutchins and Marusic, 2007b, there is an increase in the amount of low wave number energy that extends to the wall for higher Reynolds numbers. This phenomenon tends to intensify and become more prominent as Reynolds number increases.

Recent studies on modulating these large-scale structures using various wall-embedded actuation are based on the realization that even in high Reynolds number flows, large-scale structures in the outer layer influence the near-wall scale.

2.4.4. Statistical Mechanics of Large Scale Motions

The statistical mechanics of large scales are essential as they provide insight into the organization and dynamics of large scales. The LSMs and VLSMs play a significant role in transporting mass and momentum in a TBL. To better understand these large-scale outer structures, various statistical methods have been put forward. These methods are *(1)* Two-Point Correlation and *(2)* Energy Spectrum.

Two-Point Correlation

Two-point spatial correlation is a statistical analysis tool for quantifying the similarities between two points in a flow field. It gives information regarding the organization and formation of fluid structures such as eddies, vortices, and other coherent structures. Two-point spatial correlation has also been employed extensively in the past to examine the organization and general features of turbulence structures [Sillero et al., 2014; Wang et al., 2019; Chen, 2019]. The Eulerian two-point correlation coefficient can be defined as:

$$R_E(x, \Delta x, \tau) = \frac{\langle u_i\left(x, t_0\right) u_j\left(x+\Delta x, t_0+\tau\right)\rangle}{\sqrt{\langle u_i^2\left(x, t_0\right)\rangle}\sqrt{\langle u_j^2\left(x+\Delta x, t_0+\tau\right)\rangle}} \tag{2.23}$$

Where $\langle\cdot\rangle$ represents ensemble averaging; x is the initial reference position ($x = x_1, y_1, z_1$); $x + \Delta x = (x_1+\Delta x_1, y_1+\Delta y_1, z_1+\Delta z_1)$ are the new location with respect to initial position x; τ is the time increment between initial time t_o and final time $t_o + \tau$; u_i and u_j denotes the velocity fluctuation for $i, j = x, y, z$ at a given position and time. For PIV measurements, the averaging is done over all captured snapshots. The reference position is taken at the middle of the domain ($z_{ref} = z^+ = 0$), and the new location is taken along traversed spanwise z_{signal} location. Practically the numerator of Equation 2.23 is calculated by taking a Fourier transform of the reference signal and multiplying it with the complex conjugate of the Fourier transform of the new location signal. This value is then normalized by the product of the standard deviations of the velocity fluctuations at both locations.

Different types of two-point correlation, such as conditioned correlation, velocity-velocity, velocity-vorticity, or Reynolds stress correlation function, can be used to characterize different fluid motions. In addition, they can be used to characterize different properties of a coherent structure, such as its shape, size, and location.

Hutchins and Marusic, 2007b used high-resolution PIV data to compute two-point correlation at different wall-normal locations for analyzing large-scale structures' scaling behavior. They observed self-similar behavior in both streamwise and spanwise directions. They postulated that the length scale of LSMs grows proportional to the distance from the wall, and their contribution to RSS grows significantly in the outer region of TBL. Therefore the two-point correlation contour, as visualized in Figure 2.13, can be used to analyze the spatial organization and strength of existing and introduced large-scale streaks.

Energy Spectra For Statistical Analysis Of Turbulent Boundary Layer

The energy spectrum is a useful tool to analyze the distribution and organization of energy across different length scales. It is used measures the power spectral density (PSD) on all scales present in a turbulent boundary layer and interprets the turbulence cascade. Considering the fluctuation of the streamwise velocity component as (u'), then $\phi_{uu}(k_x)$ represents the energy spectrum, and k_x is the streamwise wave number. The energy spectrum is constructed from the time series of the fluctuating velocity component $(u'(t))$. $k_x = \frac{2\pi}{\lambda_x}$ represents the relationship between the streamwise wave number and streamwise wavelength. Streamwise turbulence intensity also referred as velocity variance $(\bar{u'^2})$ is equal to the integrated spectral energy: $\bar{u'^2} = \int \phi_{uu} dk_x$. Pope, 2000, and Baars and Marusic, 2020 describes a detailed construction method for the energy spectrum. The pre-multiplied energy spectrum $k_x\phi_{uu}(k_x)$ can be plotted against the wave number k_x or the wavelength λ_x to analyze the contribution and wave number of different scales at different wall-normal positions.

Using time series data from HWA in an experimental campaign or Direct Numerical Simulation results (DNS), the energy spectrum contour can be generated. A hot-wire time series is used for the experimental campaigns to construct an energy spectrum based on the frequency-wavelength conversion [Baars and Marusic, 2020]. The frequency-wave number conversion is non-trivial; hence Taylor's frozen hypothesis can be applied. This fundamental assumption simplifies the effect of turbulence scale interaction while modeling different real-world cases. According to Taylor, the statistical properties of turbulence remain constant along individual fluid properties. Here the fluid is assumed to be in a quasi-steady state, where the flow properties remain constant over a time scale much longer than the turbulence time scale. This allows assuming the turbulent flow to be frozen, simplifying to study of the statistical properties. Therefore, $k_x = \frac{2\pi f}{U_c}$, where u_c is the convection velocity of structures present at various locations of the turbulent boundary layer and convecting downstream. When scaled with inner variables, the inner layer's convection velocity is approximately constant ($u_c^+ \approx 10$). In contrast, the convection velocity is approximately equal to the mean boundary layer velocity for the outer layer.

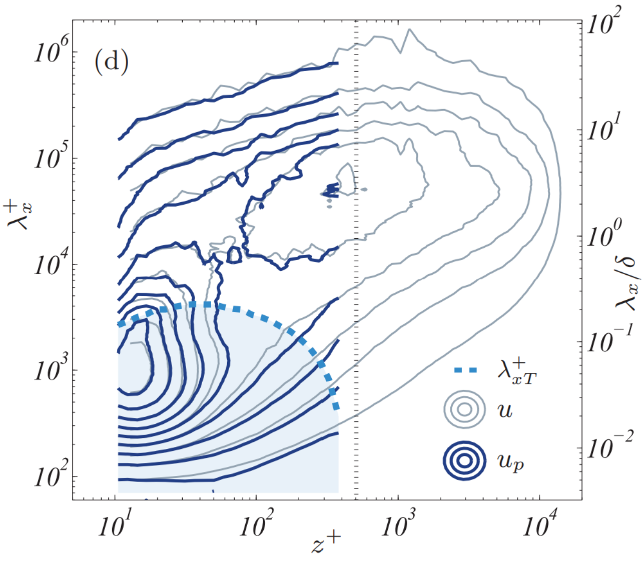

Figure 2.15: Contour for pre-multiplied energy spectra of 'u' fluctuation as visualized by Baars et al., 2016.

In high Reynolds number flow TBL, the presence and significance of LSMs and VLSMs are evident in the pre-multiplied energy spectra. LSMs and VLSMs produce a second peak on the spectrogram for u' across the boundary layer for flows with $Re_\tau > 2000$. This peak is located at the geometric center of the logarithmic region, i.e., at $y^+ = 3.9\sqrt{Re_\tau}$. Baars et al., 2016 confirmed this with a pre-multiplied energy spectrogram map for the u' fluctuation, as visualized in Figure 2.15.

Effect Of Reynolds Number On Energy Spectra

The outer peak, as visualized in Figure 2.15 provides insight into the effect of the Reynolds number on scales in the inner and outer layers. As Equation 2.8 and Equation 2.2 show the relation between Re_τ, l^*, and δ, any increase in the Reynolds number influences the expansion of the outer layer. This is because the viscous length scale at $y^+ \approx 100$ is assumed to be fixed in the inner layer. Hence any increase in Re_τ directly affects the expansion of the outer layer compared to the inner layer. As the superstructure primarily follows an outer scaling, a higher Reynolds number also increases the size and energy of these structures relative to those near the wall. As mentioned earlier, this also increases the amplifying and superposition effects of these outer layer structures on the near-wall scales.

For flow at a higher Reynolds number, the length scale of near-wall small-scales becomes very small compared viscous length scale. In a real-life scenario, an aircraft fuselage at a very high Re_τ has a viscous length scale in order of $\mathcal{O}(100\mu m)$ along with a characteristic inner scale frequency of $\mathcal{O}(10KHz)$ [Ruan, 2021]. This makes it impossible to target near-wall small-scale with conventional actuators making small-scale manipulation practically impossible at higher Reynolds numbers.

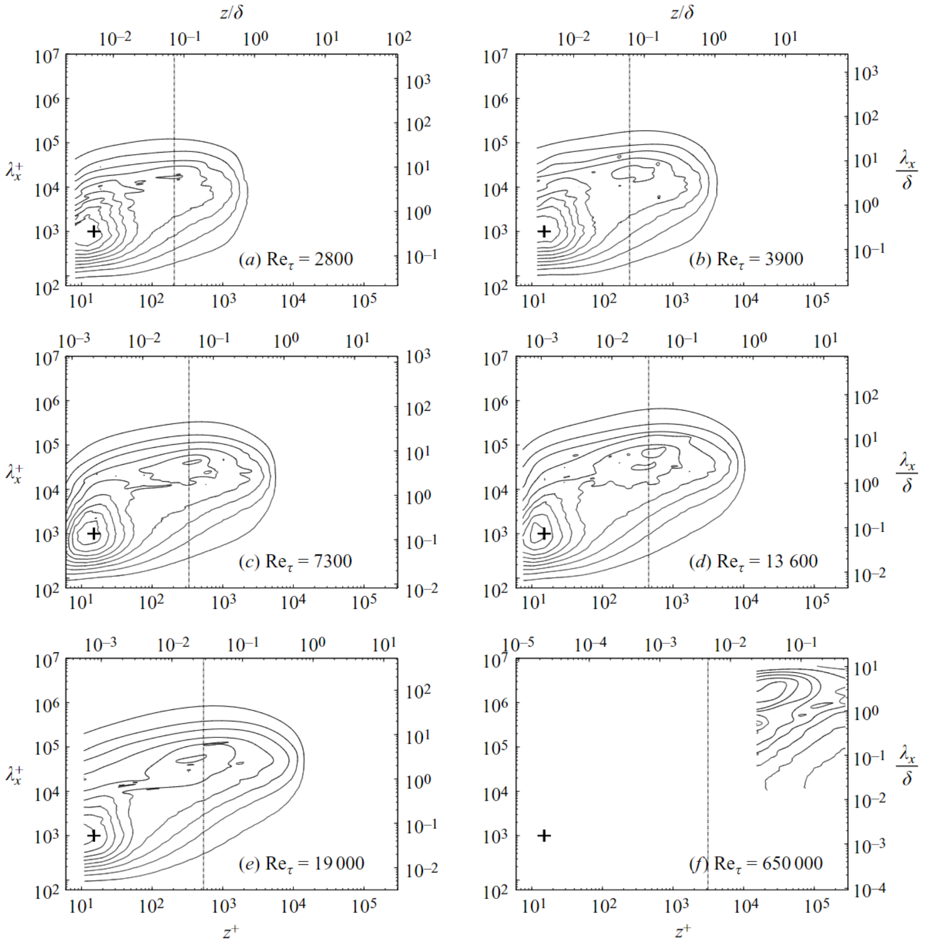

Figure 2.16: Reynolds number effect on pre-multiplied energy spectra of ’u’ fluctuation as visualized by Baars et al., 2016.

The (**+**) sign denotes the location of the inner spectral peak, which is at $y^+ = 15$ for various Reynolds numbers, as shown in Figure 2.16. The dotted line passes across the middle of the logarithmic region and the second peak, representing the outer spectral peak. As Re_{tau} increases from 2.800 to 13,000, the intensity of the outer spectral peak increases alongside an increase in the energy spectrum and the activity of superstructures in the outer layer.

2.5. Concluding Remarks On Flow Structures

The characteristic length scale of LSMs and VLSMs are in order of $\mathcal{O}(\delta)$, and the production of these structures increases with an increase in Reynolds number, making their production rate comparable to the production of small-scale structures. As these LSMs and VLSMs interact with the near-wall structures, they can be a suitable target for efficient flow control. The significant advantage of large-scale manipulation is the characteristic frequency of these structures, as it is inversely proportional to the Reynolds number [Smits and Sreenivasan, 2010].

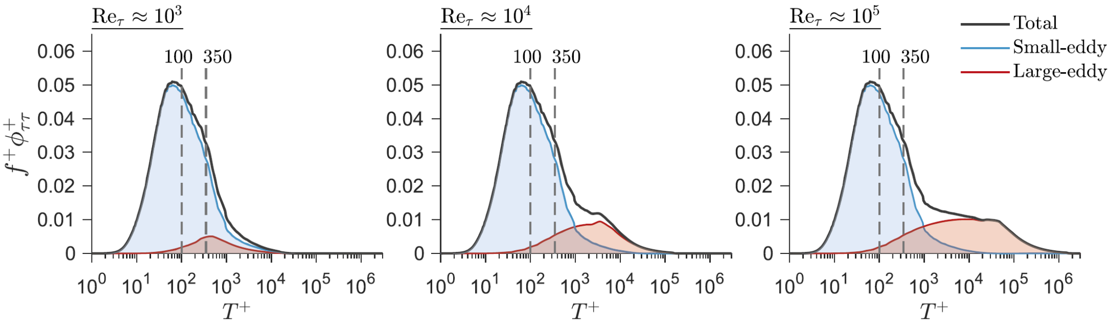

Figure 2.17: Wall spectrum dependence on Reynolds number. Pre-multiplied spectra of the wall stress with inner scaling without any forcing [Marusic et al., 2021].

In Figure 2.17, the wall stress spectrum is plotted as a function of non-dimensional time for a range of Re_τ. The area under the curve corresponds to the variance of inner scaled τ_w. Each spectrum is decomposed into the contribution from high frequency (corresponds to small eddy) and contribution from low frequency (corresponds to large eddy). The **contribution of the large eddies to total wall stress increases with the Reynolds number**; hence at a **higher Reynolds number flow, comparatively lower frequencies are required to actuate/manipulate the LSMs**. This also ensures a reduction in the power required. For example, for a flow at $Re_\tau = 12,800$, the T^+_{OSC} increases ten times from 100 to 1000 for LSMs. The corresponding frequency decreases ten folds from $150Hz$ to $15Hz$, which is less energy intensive. Therefore it is hypothesized that **large scale manipulation will be less energy intensive and might result in net power saving**.

3

Flow Control Strategy for Turbulent Drag Reduction

After reviewing the fundamentals of a TBL flow, various flow features, and the Reynolds number effect. It is essential to dig deeper into controlling and manipulating these phenomena to achieve drag reduction. This chapter deals with various passive and active control devices already being used or in various stages of research to propose an efficient and simple flow control technique.

Passive flow control devices are usually preferred over active flow control techniques due to no power requirement. Active flow control systems employ powered devices, such as sensors and actuators, combined with a control algorithm to dynamically manipulate the flow properties near the wall by targeting specific spatiotemporal scales. These active control techniques are frequently considered superior due to their enhanced control authority. Additionally, active flow control can adapt to changing conditions and optimize system performance through real-time adjustments or predetermined approaches, providing a more adaptable and versatile flow control approach [Ghaemi, 2020]. Each subsection below is dedicated to individual active and passive flow control methods and extensively discusses its working principle, the current state of research, and applicability. The active control method is limited to wall-embedded actuation as they are directly relevant to this thesis work.

3.1. Passive Control Method For Drag Reduction

Passive control methods are flow control techniques that manipulate flow dynamics via inherent flow characteristics, modified geometry, or material property without using any external power. They include techniques such as:

Large Eddy Break up Devices

LEBU (Large-Eddy Breakup Devices) is a typical passive flow control system that manipulates the flow dynamics to improve efficiency. They are typically an outer-scaled control technique shaped as an airfoil and placed between $0.1\delta < y < 0.8\delta$ aligned to primary flow. LEBUs primarily work by breaking up the large scales turbulent structures into small scales that are quickly dissipated by the viscous effects of the flow (as visualized in Figure 3.1). This, overall, reduces the turbulence intensity [Corke et al., 1981]. Chan et al., 2021 conducted a numerical simulation and differentiated between three regions downstream of the LEBUs. In the first region, the unsteady vortices in the wake travel in TBL's inner and outer regions, dampening the velocity fluctuation near the wall. In the second region's case, the velocity fluctuation's dampening effect becomes more pronounced. This region also accounts for the highest local skin friction reduction due to the interaction of the inner vortex with the viscous sublayer. Finally, in the third region, these inner vortices move away from the wall, regenerating the Reynolds stresses. These three regions can be visualized in Figure 3.2.

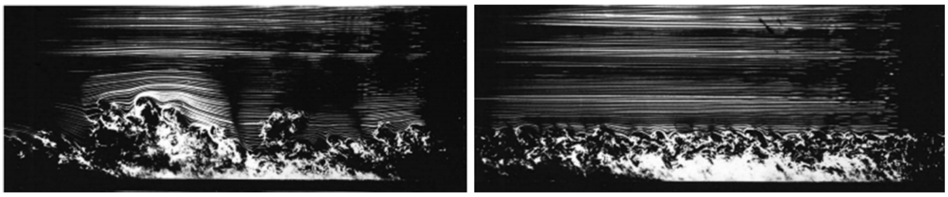

Figure 3.1: Effect of LEBU on TBL. (Left) TBL without LEBU and (Right) TBL with LEBU [Corke et al., 1981].

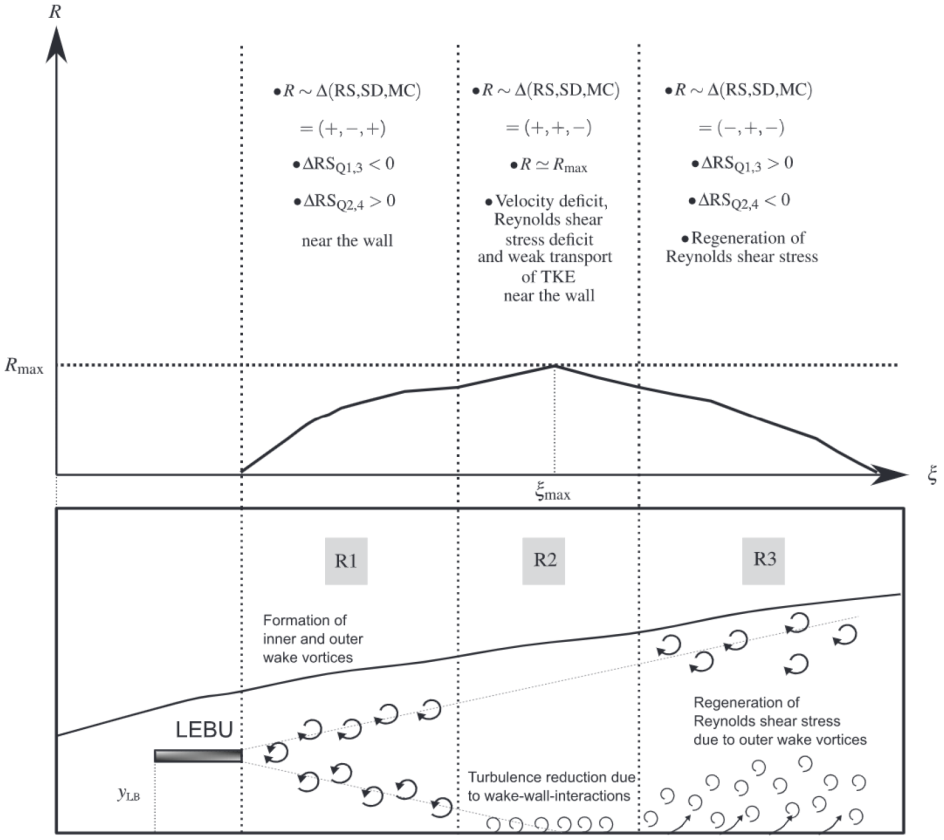

Figure 3.2: Schematic of skin friction reduction downstream of LEBU [Chan et al., 2021].

Despite friction drag reduction, this control strategy does not provide any net power savings, as an extra flat plate in the flow creates additional disruption and pressure drag. Furthermore, the regeneration of Reynolds stresses in the last region also increases local skin friction. Finally, integrating such large structures on a full-scale aircraft creates additional complexity. However, understanding the scales' interaction and manipulation will aid future innovative designs.

Riblets

Riblets break the coherence of streaks, disrupting the turbulence production cycle [García-Mayoral and Jiménez, 2011]. Conversely, the vorticity generated in the grooves of riblets interacts with the streamwise vortical structures and dampens them. Smith et al., 1990 hypothesized that riblets interfere with the periodic spanwise sinuous low-speed streaks. These low-speed streaks are elongated regions of relatively low-speed fluid that meander in the spanwise direction. Therefore, by disrupting this organization, riblets influence near-wall turbulence and reduce drag. Even though riblets are widely used in the aviation industry for ease of manufacturing and implementation, practical issues such as dirt, icing, wear, and weight create a bottleneck for their application.

3.2. Wall Embedded Active Control Method

Active flow control methods add mass, momentum, or energy to the flow. As a result, these methods need a constant power supply for their operation, making their implementation far more complex than passive control methods. However, unlike the passive control method, active flow control methods intermittently change the local fluid properties through a controlled closed loop or predetermined open loop control. Some other active flow control techniques not covered in this report include plasma actuators, polymer injection, and porous wall blowing, among others.

3.2.1. Wall Suction and Blowing

Wall suction and blowing have been a topic of interest for the past few decades due to their effectiveness for flow control. Sano and Hirayama, 1985 studied the effect of steady blowing and suction in the spanwise direction in a TBL. They concluded that during the phase of steady suction, the turbulent intensity tends to decrease, increasing the skin friction downstream of the spanwise slot. On the contrary, the blowing reduces the skin friction and increases the turbulent intensity. Even though later, Antonia et al., 1995 demonstrated that local suction relaminarizes the TBL, this was only seen with a very lower Re_τ (mostly in the transient Re region). The synthetic jets employing both blowing and suction also fails to achieve higher amplitude actuation, limiting the efficacy of such a technique to manipulate the energetic large scales in the outer layer. No future credible evidence was found from literature holding suction's effectiveness at higher Re_τ. As a result, **the focus shifts solely to blowing techniques**. Park and Choi, 1999 conducted multiple DNS to analyze the effect of uniform/steady suction and steady blowing. In steady blowing and suction methods, fluid is continuously injected or removed through a slot. Park and Choi, 1999 reported that steady local blowing elevates the streamwise vortices, consequently reducing and limiting their interaction with the wall. However, these uplifted vortices tend to strengthen downstream as they experience reduced viscous diffusion. The tilting and stretching of these uplifted vortices downstream from the actuation plate lead to increased turbulence intensities and skin friction.

Tardu, 1998; Tardu, 1999; Tardu and Doche, 2009 carried out multiple experimental campaigns to study the effectiveness of steady and unsteady blowing. Here unsteady blowing refers to blowing where a continuous jet goes on and off with a specified periodicity. They concluded that even though both blowing types reduce drag, the shear stress intensity is significantly reduced by unsteady blowing. The idea behind unsteady blowing is to induce pulsating coherent patterns to negatively interact with convecting energetic scales and reduce drag downstream. In addition, by targeting particular flow structures, unsteady blowing has the potential to tune to different length scales and reduce skin friction drag more effectively.

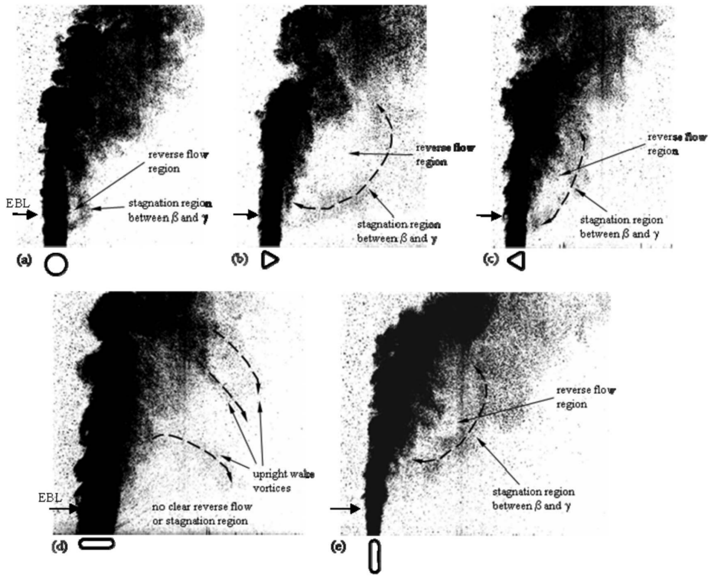

Figure 3.3: Average velocity contours of a jet plume in a cross-flow field at a blowing ratio = 8 [Gutmark et al., 2008].

Unsteady active blowing control can be implemented using either open-loop control or closed-loop control systems. In a closed-loop control system, the setup includes input sensors, a feedback loop, and an actuation system that injects fluid into the domain based on the feedback received. Input sensors, such as hot film or pressure microphones, continuously monitor the changes in the incoming TBL. In contrast, an open loop control system lacks a secondary feedback mechanism, making it less effective in targeting the energetic large-scale motions (LSMs) based on input from the feedback loop. Despite this limitation, open-loop control systems are generally simpler to operate compared to closed-loop control systems [Talluru, 2014]. Open loop control is also commonly known as ”Desynchronized control”.

Gutmark et al., 2008 investigated the interaction of the cross-flow with the flow for circular and non-circular jets in terms of their flow characteristics and jet-induced effects (see Figure 3.3). They concluded that the jets slit with a major axis aligned to the streamwise direction have better jet penetration and ensure the creation of stronger vortical pairs. To investigate the behavior of vortex rings inducing form jet and interacting with a cross-flow, Sau and Mahesh, 2008 conducted a DNS study and concluded that a reduced velocity ratio increases vorticity in the cross-flow boundary layer. Thus, for lower velocity ratios (r<2), the vorticity in the cross-flow boundary layer interacts with the nozzle boundary layer’s vorticity in the nozzle’s upstream location. At r=1, the vorticity in the nozzle-emerging boundary layer is almost annihilated by the incoming cross-flow boundary layer. Therefore, no complete vortex ring structures form for lower velocity ratio cases. Instead, a hairpin structure is formed due to the downstream side’s roll-up alone. The scalar contours due to the counter-rotating hairpin legs in the spanwise plane appear similar to those of the counter-rotating vortex pair (CVP) seen for higher exit velocity ratio jets in cross flow. However, in the case of a lower exit velocity ratio, there is no CVP.

Cheng et al., 2021 and Zhang et al., 2022 tried controlling the TBL through a steady and unsteady blowing technique via multiple streamwise jet slits to understand the dependence of skin friction reduction on the blowing strategy and geometric parameters of the jet slit. Cheng et al., 2021 concluded that multiple slits reduce drag through two distinct mechanisms in cases of steady blowing strategy. First, the regularized streamwise vortices form a barrier between the QSVs and the wall. This hinders the sweep from interacting with the wall and reduces drag. Secondly, the introduced zero-momentum fluid decreases the streamwise velocity gradient near the wall. However, the observations made by Cheng et al., 2021 for weighted PSD of streamwise velocity fluctuations are opposite to what IUSO et al., 2002 observed. To reduce drag, IUSO et al., 2002 introduced large-scale streamwise counter-rotating vortex pairs to achieve drag reduction. Contrary to what was observed by Cheng et al., 2021, the energy content of larger length scales increased, and lower length scales decreased for IUSO et al., 2002. The streamwise vortices introduced by IUSO et al., 2002 had a stabilizing effect because large-scale control techniques increased the lateral spacing and length of near-wall streaks, thereby increasing the energy content of large scales.

Talluru, 2014 were among the first to study the effect of both open and closed-loop control schemes to target large-scale structures in a TBL via a single jet. Even though there were a few drawbacks with Talluru, 2014 due to improper scaling of the jet, the project work positively concluded on the effectiveness of streamwise oriented jet to affect large scale structures for a greater streamwise distance. However, this thesis project will solely focus on **open loop blowing control for manipulating large scales convecting in the log region** for drag reduction in order to reduce the complexity of input sensor installation for LSM detection and the complexity of transfer function for real-time actuation.

3.2.2. Wall Oscillation

After several numerical research on a developed TBL, evidence of a reduction in the turbulence production and the RSS via sudden spanwise pressure gradient was given by Sendstad, 1992, and Bradshaw and Pontikos, 1985. This claim paved the way for multiple works on steady and unsteady transverse wall motion to achieve drag reduction. Later, Jung et al., 1992 stipulated a significant drag reduction in a TBL when subjected to unsteady transverse wall motion. Spanwise wall oscillation was first carried out experimentally by Laadhari et al., 1994 in a channel (see Figure 3.4). They observed a reduction in the second-order turbulence statistics compared to the uncontrolled case. The oscillating plate is mounted on a crankshaft and enclosed inside the channel. The behavior of RSS with frequency observed by Laadhari et al., 1994 agreed well with the initial study by Jung et al., 1992. Following this, Choi et al., 1998 measured up to 45% reduction in drag coefficient near the wall for up to $5 \cdot \delta$ distance downstream at $Re_\theta = 1.19 \cdot 10^3$.

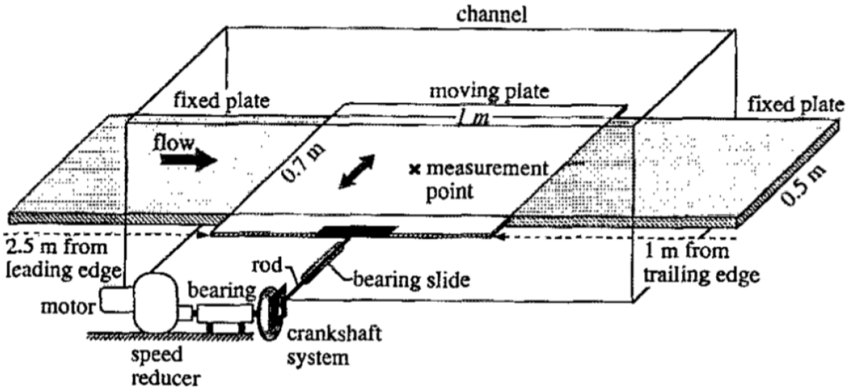

Figure 3.4: Schematic of experimental setup for wall oscillation [Laadhari et al., 1994].

Laadhari et al., 1994 attempted to explain the reason behind drag reduction with turbulence statistics, attributing the interaction between near-wall low-speed streaks and longitudinal vortices to be the reason. The streamwise vortices induced convects in the spanwise direction breaking its coherence and reducing turbulence production. Later, Ricco, 2004 also concluded that the streaks are dragged laterally due to the formation of the periodic Stokes layer due to wall oscillation. For a better understanding, Ricco et al., 2012 carried out several DNS studies keeping unambiguous inner scaling. This resulted in a drag reduction and manifested as an increased mass flow rate source. Therefore, the amount of energy spent on wall oscillation is equivalent to the viscous dissipation when looking at the global energy fluxes. Later, Kempaiah et al., 2020 claimed that the key to skin friction reduction is a reduction of hairpin packets and near-wall vorticity. He also concluded that the oscillating frequency is associated with the size of the hairpin packet, and the amplitude needs to be equivalent to the spanwise spacing of streaks. As wall oscillation is mechanically complex and energy-intensive, Hehner et al., 2019 used a novel oscillatory plasma actuator design without any moving parts. These plasma actuators use a high-frequency electric field to create localized plasma discharge, inducing an oscillatory body force and generating a stokes layer. As an alternate approach can be inducing a traveling wave in a TBL via an array of jets via an array of jets. This method is comparatively less energy intensive. The critical parameters of inducing this traveling jet via an array of jets are amplitude, frequency, and wavelength control, which can be easily adjusted based on different spatial and temporal tuning strategies.

The recent work by Marusic et al., 2021 highlights the importance of large-scale manipulation at higher Reynolds number flow. Marusic et al., 2021 obtained an order of magnitude higher drag reduction for large-scale actuation than for small-scale actuation, as extrapolated from previous models and investigations for the same Reynolds number flow. This result discovered the tendency of increasing drag reduction with Reynolds number for large-scale actuation. Therefore motivating further **investigation into the effectiveness of using an array of streamwise jet slits to mimic the wall oscillation tuned to the large scales in the log region of the TBL**. After Jung et al., 1992 first performed numerical simulations of high-frequency spanwise wall oscillation and concluded with drag reduction up to 40% at $Re_\tau = 200$. This research was further extended for TBL for higher Re_τ [Choi et al., 1998; Quadrio and Ricco, 2004; Yudhistira and Skote, 2011]. As visualized by Quadrio and Ricco, 2004 in Figure 3.5, the elongated structures meander in the spanwise direction and eventually lose their identity when they burst upward.

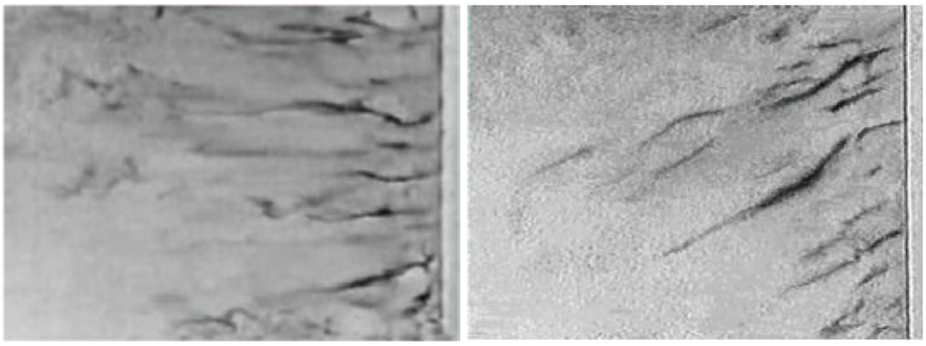

Figure 3.5: Wall-parallel view with platinum wire at $y^+ = 5$ for a stationary wall (left) and a spanwise oscillating wall (right) as visualized by Quadrio and Ricco, 2004

Other forms of spatiotemporal forcing have been developed over the years to attain similar or more effective drag reduction by introducing oscillating spanwise shear. The first modified technique inspired by wall oscillation is a spanwise or streamwise traveling wave [Du and Karniadakis, 2000; Umair et al., 2022]. Itoh et al., 2006 deformed the wall wavily in the wall-normal direction to generate a secondary flow of periodic wall-normal and spanwise fluctuation, and they observed a positive drag reduction. They concluded that the drag reduction is due to the interaction between the near wall streaks and the traveling or oscillating spanwise shear. For maximum efficiency, the frequency of traveling or oscillation can be set to the frequency of near-wall scales [Itoh et al., 2006]. Gatti and Quadrio, 2016 examined the efficacy of spanwise forcing at a higher Reynolds number to yield a reduction in turbulent drag. This study first addressed the effect of amplitude of forcing to have a comprehensive view of the drag-reducing characteristics of traveling waves. Later, Albers et al., 2020 carried out a high-resolution large eddy simulation (as visualized in Figure 3.6) to analyze the drag-reducing and the net power-saving potential of this control strategy. They first concluded with similarities between spanwise traveling waves with wall-normal deflection and spanwise wall oscillation without wall-normal deflection. The spanwise oscillating stokes layer formed for both cases correlated with skin friction reduction.

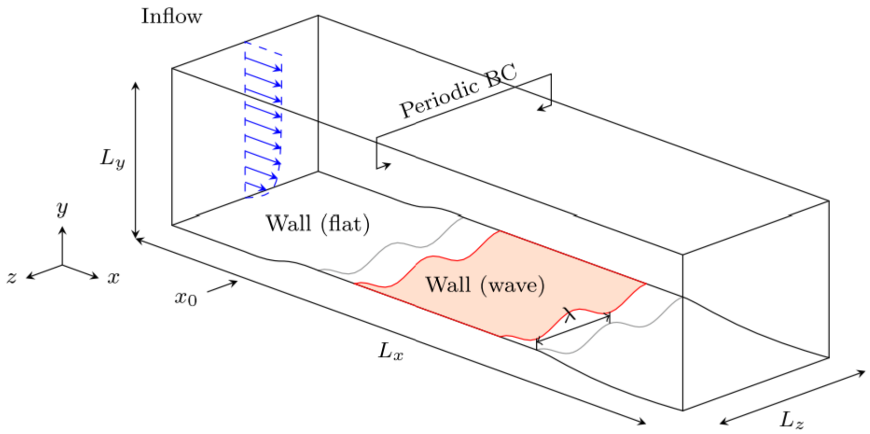

Figure 3.6: Spanwise travelling wave modelled by Albers et al., 2020.

Albers et al., 2020 concluded that there was no linear relationship between drag reduction and net energy saving due to the nonlinear response of near-wall flow to the drag-reducing actuation parameters. Therefore the highest drag-reducing actuation does not result in maximum power saving. These studies confirm that spanwise forcing is inefficient for near-wall small-scale actuation but is hypothesized to be efficient for large-scale manipulation resulting in net energy savings. Additionally, it can be established that a 2-dimensional wall oscillation and 2-dimensional spanwise traveling wave work under the same principle to reduce drag.

4

Experimental Methodology And SetUp

In light of the effectiveness of temporary and sudden pressure gradient variation in suppressing turbulence [Sendstad, 1992], the concept of spanwise traveling waves will be investigated further. Even though Albers et al., 2020 discusses the effectiveness of this approach with a range of wave amplitudes and wavelengths aimed at the near-wall scale, additional research needs to be done to analyze the effectiveness of this control technique tuned to large scales. Additionally, the extremely high oscillation frequency requirement of $15KHz$ for near-wall small-scale manipulation at a cruise speed of $225m/s$ is energy intensive and difficult to achieve with the current state of actuators. The energy required for such actuation might eventually outweigh the net energy saving due to drag reduction. As Re_τ increases, the contribution of low frequency (large eddy) increases [Marusic et al., 2021]. This makes large-scale forcing an ideal and efficient choice for real-world applications.

An array of streamwise jet slits can be employed to generate streamwise streaks that resonate with the coherent frequency of LSMs within a TBL. These induced streaks interact negatively with the LSMs and influence near-wall scales via amplitude modulation or superposition. Thus further leading to a reduction in drag. The streamwise streaks disrupt the momentum transfer mechanisms within the LSMs, weakening their contribution to the overall drag. Alternatively, blowing individual jet slits with a time delay creates a spanwise traveling wave. This traveling wave can be tuned both spatially and temporally to match the width and coherent frequency of the LSMs. By tuning the traveling wave to align with the LSMs' characteristics, it becomes possible to target these structures effectively and attenuate them. In both approaches, the idea is to manipulate the flow structures within the TBL to counteract the LSMs responsible for drag generation. By carefully designing the jet slits' configuration and tuning the induced coherent patterns to the LSMs, these approaches can significantly reduce drag within the boundary layer.

4.1. Array Of Streamwise Blowing Jet Slits

Unsteady wall normal blowing via a single streamwise jet slit has been studied earlier to understand the dependence of drag reduction on different actuation and slit geometry parameters. Cheng et al., 2021 aimed to understand the influence of wall-normal jets and obtained substantial drag reduction up to 70% persisting 500 wall units downstream. They concluded that the unsteady jets from the slit create highly regularized streamwise vortices, interrupting the turbulence regeneration cycle. Secondly, the zero-streamwise momentum fluid reduces the near-wall streamwise velocity, reducing drag downstream. However, the first mechanism dominates unsteady blowing. This unequivocally concludes that unsteady blowing can attain higher drag reduction than steady blowing. Later, Zhang et al., 2022 carried out the same experiment with multiple slits to investigate the dependence of drag reduction on slit parameters, including the slit width, length, number of slits, and separation between two slits (see Figure 4.1). Interestingly, they observed higher drag reduction for high-frequency unsteady blowing than compared to steady blowing. They concluded that the main reason behind drag reduction via unsteady blowing is producing a layer of streamwise vortices near the wall or spanwise velocity gradient that counteracts the sweep motion and interrupts the turbulence regeneration. Zhang et al., 2022 also concluded that with increased slit width, the drag reduction also increases for steady blowing. On the contrary, for unsteady blowing, the jet penetration height is highly correlated with drag reduction.

As an array of wall-normal streamwise jet slits have proven beneficial for drag reduction, the actuation has majorly been tuned to the oscillating frequency of the near-wall small scales. However, given the disadvantages of near-wall small-scale forcing and the increasing contribution of large scales to RSS at a high Reynolds number, more research needs to be done to study the efficacy of such an actuation technique for controlling energetic larger scales. Given the multiple advantages of the blowing mechanism via multiple streamwise jet slits, a control strategy can be developed to manipulate the convecting large scales to reduce drag.

The exit velocity of the jet during blowing can be controlled based on different approaches and aspects of a TBL. The jet exit velocity can be set in terms of velocity ratio, which is given as:

$$r = \frac{v_{jet}}{u_{\infty}} \tag{4.1}$$

A higher jet exit velocity can ensure an efficient penetration of the jet plume to the edge of the boundary layer; however, this can have a detrimental effect and alter the flow physics. The overall pressure drag created due to higher jet penetration degrades the whole TBL (see subsection 3.2.1). Therefore the velocity ratio (r) needs to be selected such that it has the least pressure drag but efficient jet penetration to the middle of the log region. When $r < 0.3$, the jet plume from the streamwise jet slits is unstable. However, at $r = 0.4$, the trajectory emanates from the jet's geometric middle and remains in the log region up to a minimum distance of δ downstream Dacome, 2022b.

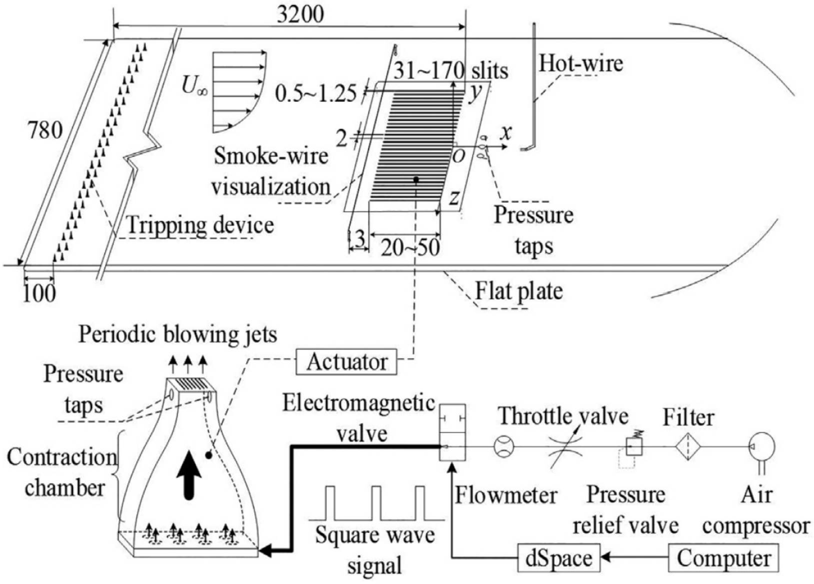

Figure 4.1: Schematic of setup for steady and unsteady blowing via streamwise slits as presented by Zhang et al., 2022.

4.2. Formulation Of Spanwise Travelling Waves And Coordinate System

The spanwise traveling wave can be formulated as a sinusoidal oscillation as given by Marusic et al., 2021. The spanwise traveling wave equation can be written as:

$$w_z(z,t) = \sin(k_z z - \omega_x t) \tag{4.2}$$

Here w_z is the spanwise velocity at any given instant, ω_x represents the angular frequency of the spanwise traveling wave, and $k_z = 2\pi/\lambda_z$ is the wave number. The variables ω_x and k_z represent the wave characteristics. The Equation 4.2 can be re-written as:

$$w_z(z,t) = [(\sin(k_z z)\cos(\omega_x t)) - (\cos(k_z z)\sin(\omega_x t))] \tag{4.3}$$

The wave character defining variables λ_z and ω_x can be tuned to the frequency and spanwise width of the LSMs to manipulate and reduce drag downstream effectively.

Coordinate System

Before imposing this formulated spanwise traveling wave in the test section, a coordinate system must be established. This coordinate system will be kept uniform throughout the rest of the report. All the plots and graphs will adhere to this coordinate system for a more straightforward analysis.

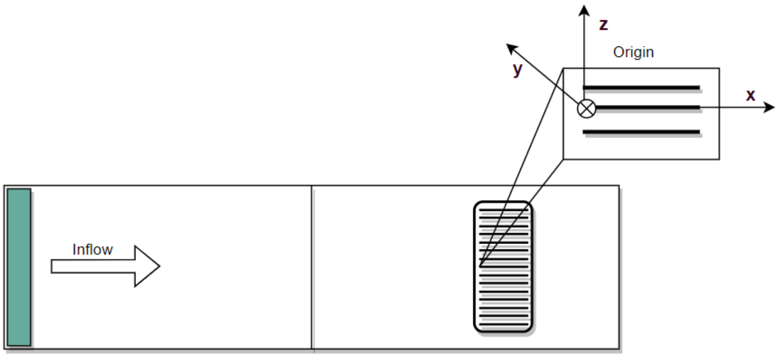

Figure 4.2: Visual representation of the coordinate system and test section considered for the experimental campaign.

First, a right-handed Cartesian coordinate system is utilized. The streamwise flow direction corresponds to the x axis, while the z axis represents the spanwise direction. The y axis denotes the wall-normal direction. The midpoint of the leading edge of the eighth jet slit is chosen as the origin of the domain. This slit is located at the center of the jet plate, ensuring that the origin lies precisely in the middle of the domain. The coordinate system can be visualized in Figure 4.2.

4.3. W-Tunnel Setup And Test Section

The experimental campaign is carried out in the W-tunnel of the Faculty of Aerospace in TU Delft's high-speed laboratory. This is a simple open jet wind tunnel and has a modular exit contraction. This can be set to different contraction ratios based on the exit freestream velocity required at the test section. The cross-section used for this experimentation is $0.6m \times 0.6m$ as it can put out an exit velocity of $16.5m/s$ at the contraction exit. The highest possible exit velocity configuration is used to investigate the effect of large-scale manipulation at a higher Reynolds number. The flow velocity is set by controlling the RPM of a centrifugal fan present inside the inlet of the W-tunnel. The W-tunnel is designed and built from wood, hence providing a highly laminar flow for the different experimental requirements. Within the tunnel's inlet, wire meshes are installed to reduce turbulence and ensure a smooth flow at the exit of the contraction section. With a freestream velocity of $16.5m/s$, the freestream turbulence at the contraction is as low as 0.3%.

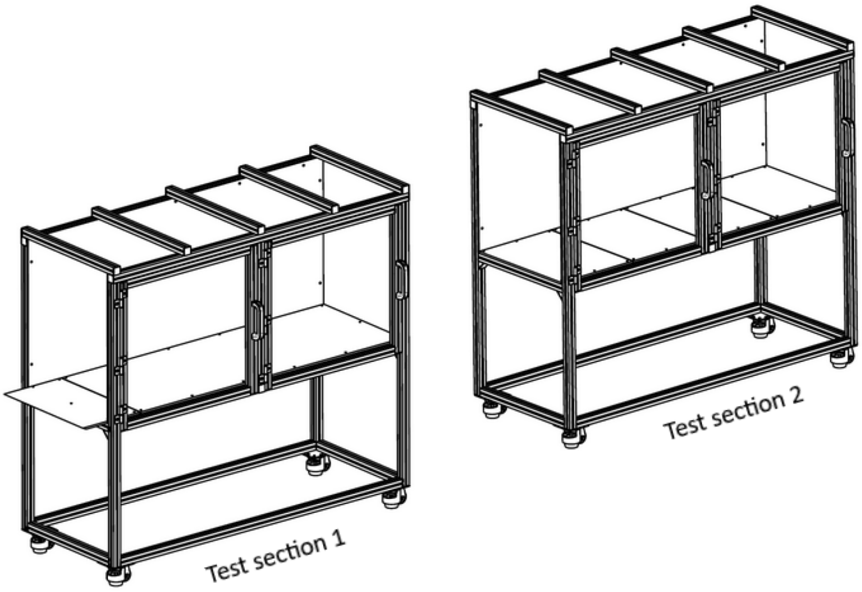

Figure 4.3: ISO view of modular test sections 1 and 2 that can be attached together via clamps and to the W-Tunnel [Baars and Dacome, 2022].

The whole test section assembly consists of two sections installed together downstream of the W-Tunnel contraction to generate a higher Reynolds number TBL. These sections are modular to conduct different experiments at low-subsonic flows for TBL and can be visualized in Figure 4.3. An individual section has a length of 1.8 m, which is then connected together to create a long flat plate measuring 3.6 m in length. A long flat plat ensures a thicker boundary layer formation downstream, making visualization and actuation to the log region relatively easier. The total length of the whole assembly is 3.75 m, which comprises an extruded plate at the bottom and top of the leading edge of section 1. The bottom extrusion in section 1 contains a strip of P40 sandpaper, which trips the boundary layer. A venturi channel attenuates the blockage effect and eliminates the flow separation at the sandpaper's leading edge. Section 2 is divided into four individual panels to provide additional modularity in choosing between different flow control devices and measurement device locations. The array of streamwise jet slits is affixed to the second-to-last panel of section 2. The actuation plate containing multiple streamwise oriented jet slits is affixed at the center of this panel, i.e., 3075 mm downstream of the trip. A pitot-static tube is fixed at the test section near the actuation plate (3400mm downstream of the trip) to measure the freestream velocity near the actuation plate and use it as a reference or to normalize certain velocity data sets. Having some clearance from the extreme open end of section 2 ensures no non-physical effect from outside. A freestream velocity of $15m/s$ with a boundary layer thickness of $0.07m$ is measured at the actuation plate location [Dacome, 2022a].

As visualized in Figure 4.4, the ceiling in section 1 and 2 are adjustable. Hence enabling the flexibility to adjust the pressure gradient ($\frac{dP_\infty}{dx}$) along the streamwise direction to get a ZPG, an APG, or FPG based on the purpose of the study. Hundred pressure taps are affixed to the bottom of the whole test section to measure $\frac{dP_\infty}{dx}$. The actuation plate and other interchangeable panels are accessible via the side-access doors (refer to Figure 4.3). Both modular sections are made up of polycarbonate (Plexiglass) to allow optical access from different planes to set the PIV measurement setup.

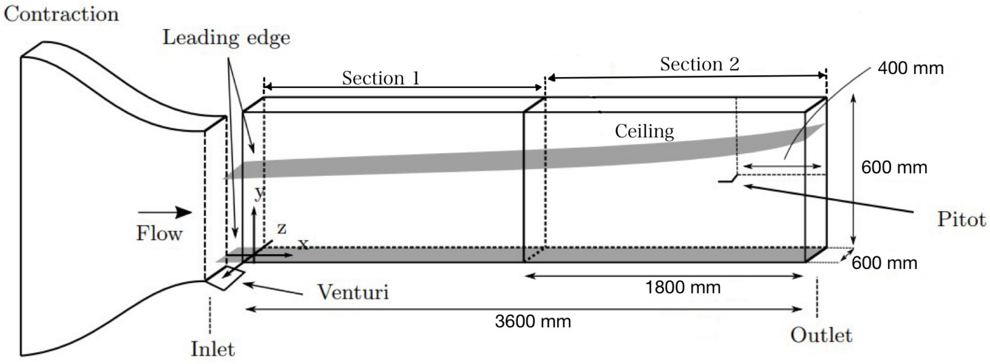

Figure 4.4: Side view schematic of the modular turbulent boundary layer set up [Baars and Dacome, 2022].

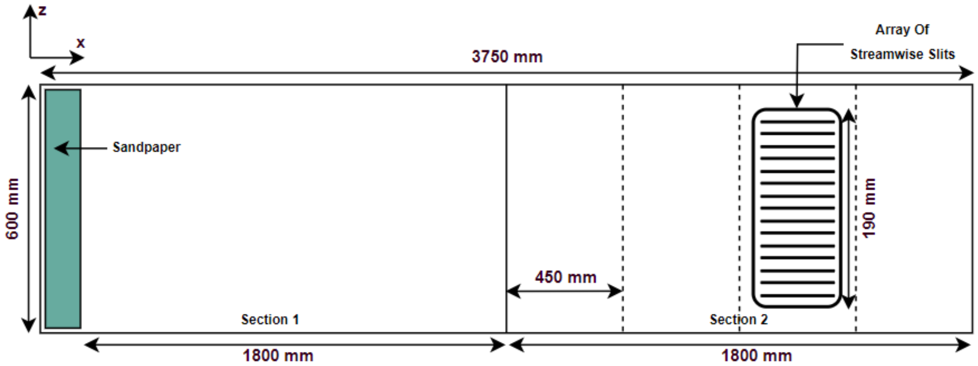

Figure 4.5: Top view schematic of the modular turbulent boundary layer set up.

Before fixing the physical dimensions of the actuation plate and actuation parameters, an overview of different flow conditions at the location of the jet plate is measured and presented in Table 4.1.

Re$_\tau$	2007
u$_\infty$	15 [m/s]
δ	69.90 [mm]
θ	6.83 [mm]
Re$_\theta$	6930
u$_\tau$	0.48 [m/s]

Table 4.1: Flow characteristic values measured at the jet plate location and calculated using composite fit [Dacome, 2022a].

4.4. Spatial and Temporal Tuning of Spanwise Traveling Waves

Different wave-defining parameters, such as λ_z and $\omega_x(\omega_x = 2\pi f_x)$, can be fixed for various control cases in order to tune the spanwise traveling wave to the LSMs. *Spatial tuning* is defined as tuning the traveling wave's wavelength (λ_z) to the spanwise spatial width of the logarithmic region's high and low momentum zone. This is calculated to be $0.3 \cdot \delta - 0.5 \cdot \delta$ using a two-point correlation of streamwise velocity fluctuations [Hutchins and Marusic, 2007b]. To understand the effect of spatial tuning, a set of wavelengths [$0.8 \cdot \delta$, $0.4 \cdot \delta$, and $1.6 \cdot \delta$] are selected.

Temporal tuning is defined as tuning the frequency ($f_x = \frac{\omega_x}{2\pi}$) of the traveling wave to the frequency of the LSMs in the log region of a TBL. When the pre-multiplied energy spectrogram of the streamwise velocity fluctuation is considered to analyze the contribution of energy by different length scales, a broad spectral peak is observed at the log region [Baars and Marusic, 2020]. As the majority of turbulent kinetic energy occurs in this region, this peak signifies the immense contribution of LSMs and VLSMs to TKE at a higher Reynolds number. As these LSMs can influence the near-wall small scales via amplitude modulation or superposition (as discussed in subsection 2.4.3), it is seen that controlling these LSMs at high Reynolds number affects the near-wall small scales and has the potential to attenuate the wall shear stress and TKE production near the wall. The location of the log region can be signified as the geometric middle point of the whole region and is given by [Baars et al., 2016]:

$$y^+_{LSMs} = 3.9\sqrt{Re_\tau} \tag{4.4}$$

The convection velocity (U_c) is the velocity at which turbulent scales propagate downstream in a TBL. This is usually equal to the mean velocity at different wall-normal locations. However, the convection velocity in the viscous sublayer and the buffer region is constant at $U_c \approx 10 \cdot u_\tau$ as seen in Figure 4.6 [Liu and Gayme, 2020].

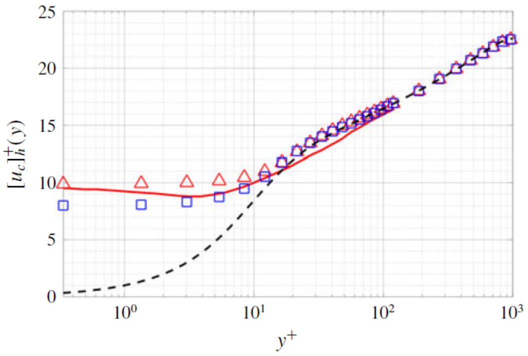

Figure 4.6: Inner-scaled convection velocity at various wall-normal locations for a TBL [Liu and Gayme, 2020].

As no direct formula is available for estimating the frequency of LSMs, the frequency(f_x) of the LSMs can either be approximated from the near-wall scale convection velocity or at the midpoint of the log region using Taylor's frozen wake hypothesis. The coherent frequency is calculated by:

$$f_x = \frac{u_c}{l_{LSM}} \tag{4.5}$$

Here $l_{LSM} = \lambda_x$ is assumed to be the streamwise length of LSMs convecting downstream and is estimated by Baars et al., 2016 to be 6 (see Figure 2.15). With the given setup and experimental conditions (see Table 4.1), the location of the outer peak in terms of wall viscous units is calculated by Equation 4.6.

$$y^+_{LSM} = 3.9\sqrt{2227} = 182.78 \tag{4.6}$$

In Figure 4.7, the mean velocity profile is measured at the location of the jet plate using the same experimental setup at $u_\infty = 15m/s$.

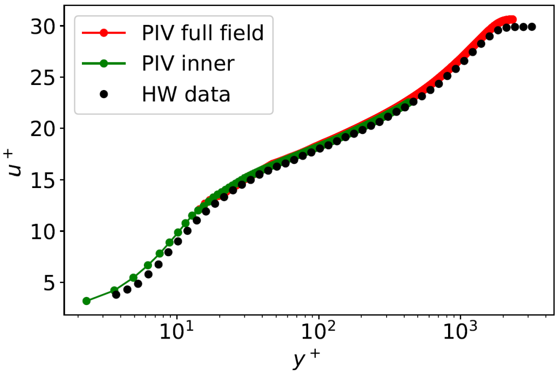

Figure 4.7: Mean velocity profile measured inside TBL setup at a freestream velocity $U_\infty = 15m/s$ [Dacome, 2022a].

Using this velocity profile, the scale convection velocity at the wall and the middle point of the log region are calculated as:

$$\begin{aligned} u_{c_{(y^+=0)}} &= 10 \cdot u_\tau \\ u_{c_{(y^+=0)}} &\approx 10 \cdot 0.480 \approx 4.80 m/s \\ f_{x_{(y^+=0)}} &= \frac{4.80}{6 \cdot 0.0699} \approx 12 Hz \end{aligned} \tag{4.7}$$

$$\begin{aligned} u^+_{(y^+_{LSM})} &= 20.5 \\ u_{c_{(y^+_{LSM})}} &\approx 9.84 m/s \\ f_{x_{(y^+_{LSM})}} &= \frac{9.84}{6 \cdot 0.0699} \approx 24 Hz \end{aligned} \tag{4.8}$$

The variables λ_z and f_x can be normalized with the outer layer variables u_∞ and δ. The non dimensional f_x^+ and λ_z^+ are given as:

$$\begin{aligned} f_x^+ &= \frac{f \cdot \delta}{u_\infty} \\ \lambda_z^+ &= \frac{\lambda}{\delta} \end{aligned} \tag{4.9}$$

Once these actuation frequencies are established, understanding the receptivity of LSMs to different control cases is crucial for designing and optimizing such large-scale active flow control techniques. Conducting experimental campaigns for different actuation frequencies and wavelengths will help analyze and quantify individual control cases' effect on attenuating the TKE production and spectral energy of streamwise velocity fluctuations. This enables identifying an optimal actuation frequency for effective large-scale manipulation. All actuators can be triggered together or individually based on the forcing strategy. Two major forcing strategies can be defined based on the wavelength of the spanwise traveling wave. As discussed in chapter 3, each forcing strategy has its own advantages and complexity. For example, based on a simple adjustment of λ_z, a standing wave (SW) or a traveling wave (TW) can be actuated. These different forcing strategies can be visualized in Figure 4.8a and Figure 4.8b. In addition, multiple control cases can be defined based on different spatial and temporal tuning strategies in order to understand the influence of individual wave-defining parameters on the efficacy of large-scale manipulation.

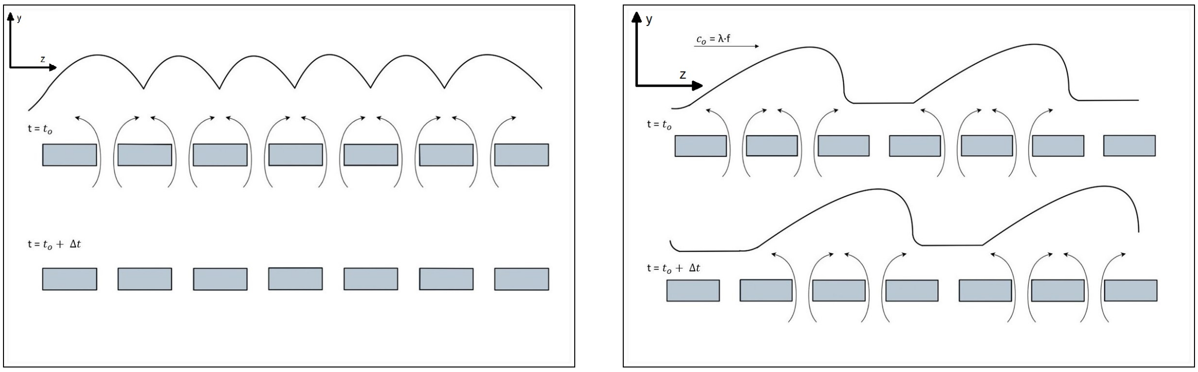

(a) **(b)**

Figure 4.8: (a.) Visualization of SW actuated from an array of wall-normal jets slits.; (b.) Visualization of TW actuated from an array of wall-normal jets slits. (Figure not to scale, only for illustrative purposes).

4.5. Test Cases Description

Several control cases can be established to investigate the relationship between drag reduction, various control strategies, and spatial and temporal tuning approaches.

Sl. No.	Forcing Startegy	u_∞ [m/s]	f_x [Hz]	f_x^+	λ_z^+
0.	Uncontrolled/Base Case	15	-	-	-
1.	SW	15	6	0.028	∞
2.	**SW**	**15**	**12**	**0.056**	∞
3.	**SW**	**15**	**24**	**0.112**	∞
4.	SW	15	48	0.224	∞
5.	TW	15	6	0.028	0.8
6.	**TW**	**15**	**12**	**0.056**	**0.8**
7.	**TW**	**15**	**24**	**0.112**	**0.8**
8.	TW	15	48	0.224	0.8
9.	TW	15	12	0.056	0.4
10.	TW	15	12	0.056	1.6
11.	TW	15	24	0.112	0.4
12.	TW	15	24	0.112	1.6

Table 4.2: Overview of all the case parameters for proposed spanwise forcing in the wind tunnel.

The Base Case 0 refers to an uncontrolled canonical TBL case, SW refers to a standing wave with a $\lambda_z = \infty$, and TW refer to a traveling wave with a defined λ_z. For the ideal spatial tuning case, $\lambda_z = 0.8{\cdot}\delta$, i.e., equal to the total spanwise spatial width of a high momentum zone and flanked low momentum zones. Actuation frequency $f_x = 12Hz$ and $f_x = 24Hz$ are estimated for the ideal temporal tuning strategy. This frequency estimation is based on different hypothesized theories used to estimate the coherent frequency of LSMs. The four ideal cases are marked in bold in Table 4.2.

To understand the influence of the introduced coherent pattern in the test section, space-time diagrams of four ideal cases are visualized in Figure 4.9 and Figure 4.10. Using Taylor's frozen hypothesis, these space-time (z-t) diagrams can be transformed into space-space(z-x) diagrams. From these plots, a rough estimation of the shape and size of the introduced coherent pattern in the test section can be seen (refer to Figure 4.11 and Figure 4.12). When these introduced patterns interact with the incoming TBL, they propagate downstream with a certain convection velocity. The magnitude and direction of this downstream propagation depend on the convection velocity at that particular wall-normal location and the size of the introduced coherent pattern. This " advection " phenomenon further causes the structure to get stretched, deformed, and mixed downstream.

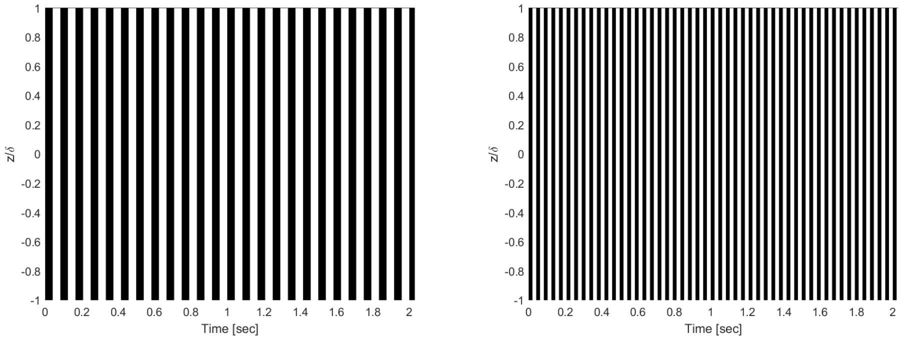

(a) **(b)**

Figure 4.9: (a.) z-t diagram of Case 2: A standing wave actuated at $f_x = 12Hz$.; (b.) z-t diagram of Case 3: A standing wave actuated at $f_x = 24Hz$.

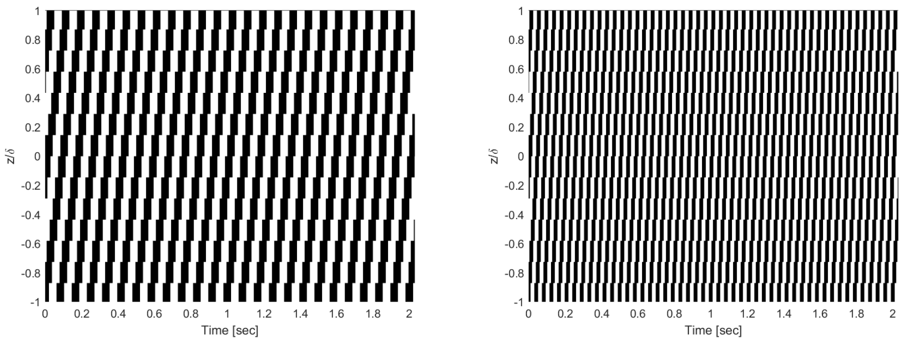

(a) (b)

Figure 4.10: (a.) z-t diagram of Case 6: A traveling wave actuated at $f_x = 12Hz$ with a $\lambda_z = 0.8 \cdot \delta$.; (b.) z-t diagram of Case 7: A traveling wave actuated at $f_x = 24Hz$ with a $\lambda_z = 0.8 \cdot \delta$.

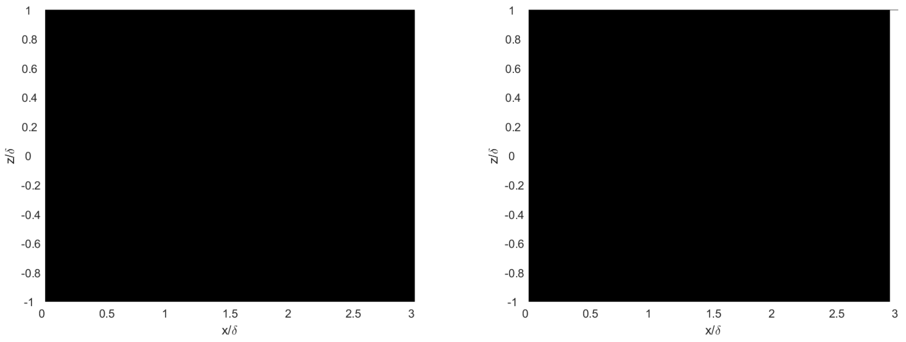

(a) (b)

Figure 4.11: (a.) z-x diagram of Case 2: A standing wave actuated at $f_x = 12Hz$.; (b.) z-t diagram of Case 3: A standing wave actuated at $f_x = 24Hz$.

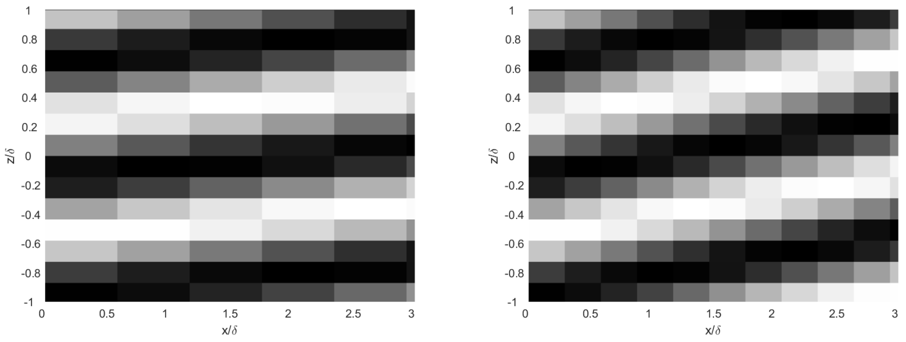

(a) (b)

Figure 4.12: (a.) z-x diagram of Case 6: A traveling wave actuated at $f_x = 12Hz$ with a $\lambda_z = 0.8 \cdot \delta$.; (b.) z-x diagram of Case 7: A traveling wave actuated at $f_x = 24Hz$ with a $\lambda_z = 0.8 \cdot \delta$.

4.6. Jet Slit Spacing

According to the Nyquist frequency criteria, to accurately measure and control a targeted flow feature, the minimum separation between actuation and measurement points needs to be at least twice the width of these LSMs. Therefore, at least a jet slit separation of $0.15 \cdot \delta - 0.2 \cdot \delta$ is required to control or measure these large-scale flow features of $0.3 \cdot \delta - 0.4 \cdot \delta$ wide [Hutchins and Marusic, 2007a].

A rectangular jet slit with dimensions $0.2 \cdot \delta \times 0.02 \cdot \delta$ (high A.R.) will ensure a higher jet penetration by creating stronger vertical pairs. Due to cross flow, the vortical pair forms at the lee-ward side and has characteristics similar to the CVP forming at the jet's far-field [Sau and Mahesh, 2008]. The vortical pair originates from the roll of the jet plume during the transfer of streamwise momentum from the cross-flow due to mean shear. Therefore, rectangular slits are recommended for optimal jet efficacy as they have the most persistent effect downstream of the actuation plate.

4.7. Full-Scale Applicability

To realize the practical viability of spanwise traveling waves, real-world dimensions can be estimated for the suggested control technique for a full-size aircraft. Table 4.3 tabulate different wave-defining parameters for different control cases as introduced in section 4.5. The wave-defining and hardware design parameters are calculated using different formulas and literature as discussed in section 4.4 and subsection 2.4.2. The suggested spatial and temporal tuning strategies result in realistic design values for the actuation plates in wind tunnel experiments and for actual flying conditions. Therefore the practicality of these approaches for rapid prototyping and industrial applications can be determined based on these estimates.

Tuning Strategy	**Typical Experimental Campaign Conditions** ($u_\infty = 15m/s$; $u_\tau = 0.48m/s$; $\delta = 0.069m$)	**Typical Real Life Flight Conditions** ($u_\infty = 250m/s$; $u_\tau = 7.1m/s$; $\delta \approx 0.353m$)
Tuned with convection velocity of inner layer small scale.	$f_x = 12Hz$ $\lambda_z = (0.4 - 1.6) \cdot \delta = 0.028 - 0.111m$ length of jet slit: $0.215 \cdot \delta = 0.015m$ spanwise length of the whole jet actuation plate = $2 \cdot \delta = 0.138m$	$f_x = 37.44Hz$ $\lambda_z = (0.4 - 1.6) \cdot \delta = 0.14 - 0.56m$ length of jet slit: $0.215 \cdot \delta = 0.0161m$ spanwise length of the whole jet actuation plate = $2 \cdot \delta = 0.706m$
Tuned with convection velocity of outer layer large scale present in the log region.	$f_x = 24Hz$ $\lambda_z = (0.4 - 1.6) \cdot \delta = 0.028 - 0.111m$ length of jet slit: $0.215 \cdot \delta = 0.015m$ spanwise length of the whole jet actuation plate = $2 \cdot \delta = 0.138m$	$f_x = 76.75Hz$ $\lambda_z = (0.4 - 1.6) \cdot \delta = 0.14 - 0.56m$ length of jet slit: $0.215 \cdot \delta = 0.151m$ spanwise length of the whole jet actuation plate = $2 \cdot \delta = 0.706m$

Table 4.3: A rough estimation of design parameters for the proposed Spanwise Traveling Wave in terms of blowing in the wind tunnel's experimental condition and for a typical fuselage condition. The typical wing conditions are approximated by Modesti et al., 2021.

As highlighted by Marusic et al., 2021, achieving the high-frequency requirements for small eddy manipulation at higher Reynolds numbers is quite challenging. On the other hand, the frequency requirements for large eddy manipulation at higher Reynolds numbers are relatively less energy-intensive. Moreover, the actuation plate's design parameters and hardware requirements are more feasible for real-life applications than other methods, such as wall oscillation. This emphasizes the ease of design and implementation of the proposed control strategy while further encouraging further evaluation of the potential impact of large-scale manipulation through spanwise traveling waves on a TBL.

The variables f_x and λ_z represent the two control parameters that define all the different control strategies. For simplicity and ease of understanding, f_x and λ_z will be replaced by f and λ in all future sections and chapters.

4.8. Implementation Of Spanwise Traveling Wave

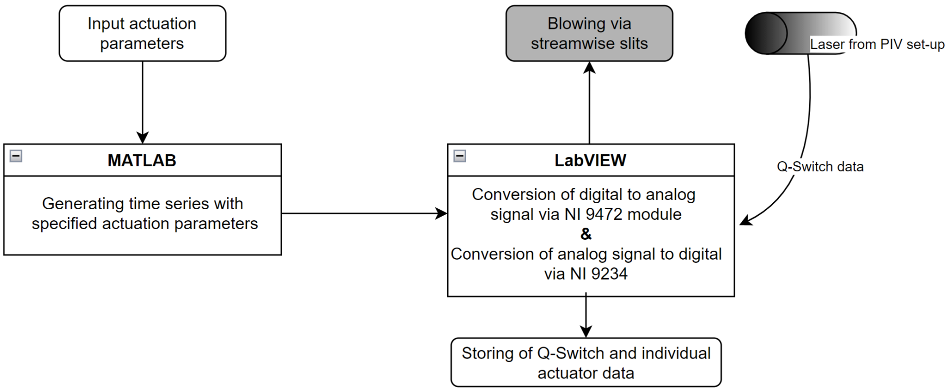

Figure 4.13: Flow chart explaining the implementation steps taken to actuate individual streamwise jet slit.

Once the spanwise traveling wave equation is formulated and various actuation parameters are set, multiple control cases are established to tune the introduced pattern to convecting LSMs. Twelve control cases and an uncontrolled base case are laid out by combining different suggested forcing strategies with various spatial and temporal tuning strategies. These are explained in section 4.2 and section 4.5. par The first step in modeling the spanwise traveling wave from the formulated equation

involves specifying the spatial (z) and temporal (t) domains. The spatial domain is scaled down based on the actual size of the test section and jet actuation plate. In contrast, the number of images required for convergence and the frequency of PIV acquisition are crucial for the temporal domain. A time series can be generated for individual actuators controlling specific jet slits according to the given ranges and the formulated equation. This file can be saved as a .csv or .mat format and imported into LabVIEW.

As shown in Figure 4.13, once this file is read and converted into a waveform, it can be transformed into an analog signal using the DAQ module and an NI 9472 board and then sent to individual actuators. Additionally, the q-switch data from the laser module is recorded using the NI 9234, which converts the analog voltage signal into a digital signal. It is essential to recreate the actual jet behavior and flow conditions while capturing a PIV image by storing the q-switch data for future result analysis.

4.9. Jet Plate Design And Assembly

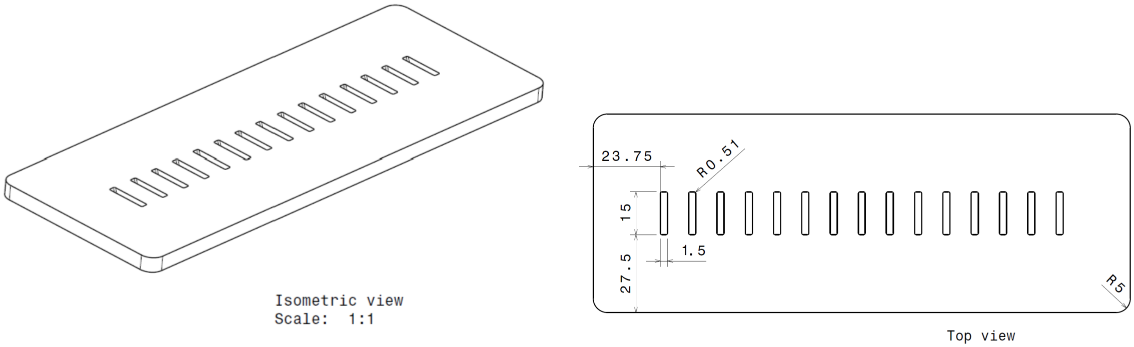

(a) Isometric view of the jet plate consisting of fifteen individual jet slits.

(b) Top view of the jet plate consisting of fifteen individual jet slits.

Figure 4.14: CAD models of the jet actuation plate[Dacome, 2022b].

As discussed previously in section 4.6, for manipulating LSM, the minimum spanwise jet slit spacing required is $0.15 \cdot \delta$. Gutmark et al., 2008 investigated the efficacy of circular and non-circular jet slits in a TBL for active flow control. They discovered that high AR slits aligned with the streamwise direction resulted in strong and efficient jet penetration with a lasting effect far downstream. Furthermore, these high AR geometries generate a hairpin with similar properties to CVP. Gutmark et al., 2008 also concluded that the geometry of the jet strongly influences the formation of coherent structures, with high AR geometries being highly effective for a more lasting effect far downstream. Therefore, it is necessary for the jets actuators to effectively interact with the large scales in the log region of a TBL in order to attain control authority from the wall position.

Considering these facts from previous literature, the array of streamwise jet slits are designed and fabricated (refer to Figure 4.14) on a jet actuation plate. Fifteen streamwise slits are designed with dimensions $15mm \times 1.5mm$ $(0.2 \cdot \delta \times 0.02 \cdot \delta)$. These fifteen jet slits span from left to right covering a spanwise length of $2 \cdot \delta$. The jet slit separation is $10.5mm$. This spanwise length of the jet actuation plate ensures actuation on multiple pairs of high and low momentum zones convecting downstream and gives better controllability.

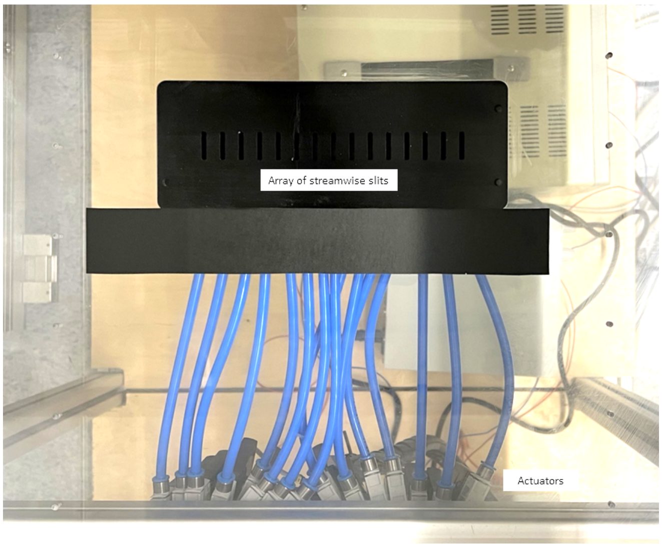

Figure 4.15: Arrangement of a flush-mounted jet plate within the test section, as seen from above.

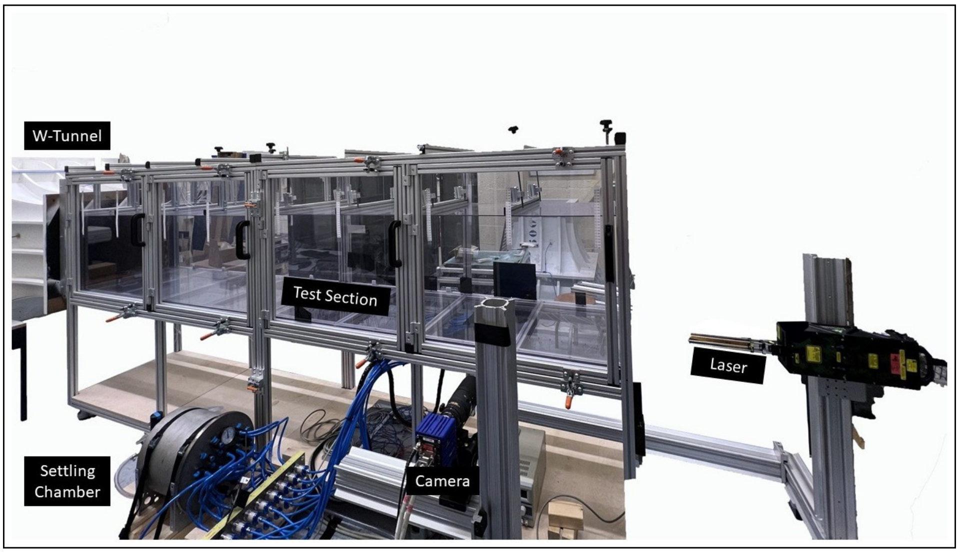

Figure 4.16: Photo of the experimental setup considered during the campaign.

As seen in Figure 4.15, an individual jet slit is connected to a fast-acting solenoid valve which can be actuated at a particular frequency. To maintain a uniform jet exit velocity from each jet slit, the individual tube connecting the pressure lines must be of equal length. Failing to do so will lead to changes in response time and inefficiencies. Figure 4.16 shows the control hardware considered during the experimental campaign. The jet plate is perfectly flush-mounted inside the wall to avoid any sudden change in surface geometry. However, any small protrusion can create an additional boundary layer inside the test section, affecting the zero pressure gradient condition. Hence, utmost care is taken to seal the gap between the interchangeable plates in order to create a smooth and uniform surface as possible.

4.10. Actuator Setup

An individual streamwise jet slit is connected to its own *FESTO MHJ-10* fast-acting solenoid actuator that can actuate at a maximum frequency of 1KHz. An individual FESTO MHJ-10 fast-acting solenoid has three terminals one positive, one negative, and one for switching. As visualized in Figure 4.17, the *NI 9472* board switches individual actuators via a *DAQ* module. Now the actuator devices are connected to the negative terminal of the power supply along with the *COM* terminal of the NI 9472 board. The *Vsup* terminal of the board is connected to the power supply, and the *Do* terminal is to the individual actuator. Finally, an individual actuator is connected to the settling chamber for feeding in dry compressed air, which is pressurized with a pressure regulator. The pressure inside the settling chamber is maintained at a particular level based on the jet exit velocity requirement. A jet exit velocity ratio $r = 0.4$ is chosen for this experimental campaign. This exit velocity ratio ensures the jet plume to emerge from the middle of the slit and convect for at least $delta$ distance in the log region. This chosen velocity ratio results in a jet exit velocity of $6m/s$.

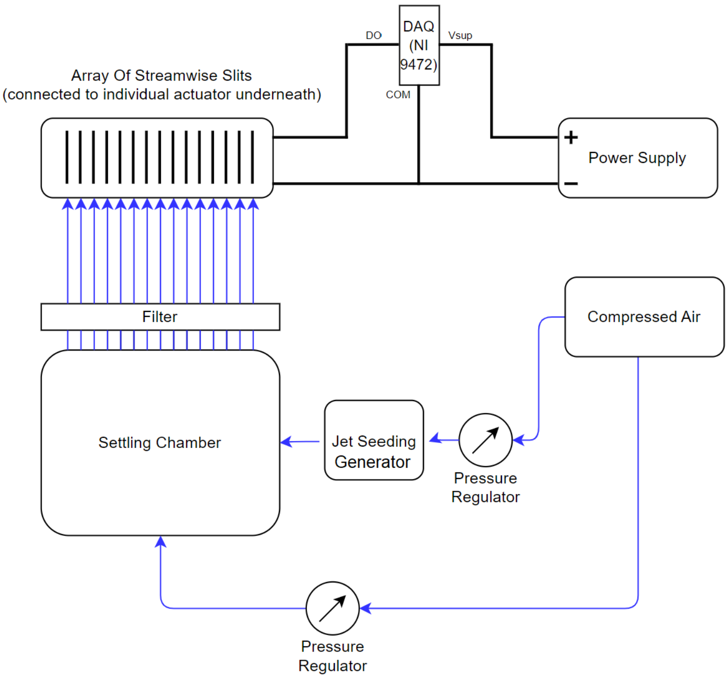

Figure 4.17: Schematic diagram of the jet actuator system.

A seeding generator is kept at a higher pressure and used to introduce the seeding particles into the jet's settling chamber. This ensures no backflow or pressure loss inside the settling chamber and establishes a uniformly seeded jet flow from individual streamwise slits. The NI board works as a switch between individual actuators and the power supply. Each actuator is connected to the NI board via a D-SUB DB25 female connector. Once a *jet on* command signal is given, it takes around $1ms$ for the fast-acting solenoid to actuate, while the flow takes $3ms$ to emerge from the streamwise slits.

5

Measurement Techniques

Following the description of the experimental methodology and setup used during the campaign, discussing specific flow measurement techniques for analyzing the flow characteristics is essential. These techniques include non-intrusive Particle Image Velocimetry (PIV) techniques and comparatively intrusive Hot-Wire Anemometry (HWA) techniques. This chapter provides a comprehensive overview of the PIV technique and practical considerations made during the campaign to measure flow characteristics and understand the receptivity of large-scale manipulation via spanwise traveling wave actuated from an array of streamwise jet slits.

A brief introduction to the working principle of HWA and data acquisition is also presented below. The acquisition of HWA data offers better time and frequency-resolved data of velocity fluctuations in the middle of the log region. This information can further help analyze the energy modulation of existing scales in the middle of the log region due to different control cases.

5.1. Planar Particle Image Velocimetry

Planar PIV is a non-intrusive 2-dimensional velocity field measurement technique. PIV techniques track the motion of individual tracer particles infused into the flow over a short duration of time, Δt. A high-power laser sheet is shone onto a specific plane, illuminating the particles and enabling the reconstruction of instantaneous velocity fields based on cross-correlation analysis. The PIV setup comprises a Lavision sCMOS camera system that captures two consecutive images with a given Δt time separation, a high-power Quantel Evergreen laser, and a programmable timing unit (PTU) that triggers the camera and laser to capture images at a particular frequency rate.

Δt is a critical parameter for PIV and depends on the magnification factor and flow velocity. When Δt is too small, it results in insufficient particle displacement. This leads to poor correlation and reduced accuracy. Conversely, when Δt is too large, it causes very large particle displacement, which eventually results in the particle exiting the window. A window here is a small overlapping sub-region of the images selected to analyze tracer particle motion over time. The size and shape of this window significantly impact measurement accuracy hence should be chosen carefully. Stitching all the windows begins by finding a common point between adjacent windows and averaging the vectors at those points to create a smooth transition between windows. This process ensures no discontinuity or inconsistencies in the velocity fields.

5.1.1. PIV Setup Parameters

Before diving into the PIV setup and measurement procedure, a brief introduction to the various measurement parameters that need to be set for obtaining well-resolved PIV data is presented below.

1. **Magnification Factor (M):** Magnification factor is a ratio between the image-to-lens distance and object-to-lens distance. This is usually rewritten in terms of pixel size, the total number of pixels,

and the size of FOVs.

$$M = \frac{d_i}{d_o} = \frac{size\ of\ pixel * no\ of\ pixels}{FOV} \tag{5.1}$$

2. **f-stop ($f^{\#}$):** $f^{\#}$ is an important parameter ensuring the FOVs are always focused. $f^{\#}$ is the ratio of the lens's focal length and the size of the diaphragm of the lens's aperture.

$$f^{\#} = \frac{f}{d_{aparture}} \tag{5.2}$$

3. **Depth Of Field (δ_z):** The depth of field represents the range of particles that are in focus.

$$\delta_z = 4.88 \cdot \lambda \cdot (f^{\#})^2 \cdot \left(\frac{M+1}{M}\right)^2 \tag{5.3}$$

Usually, the δ_z is kept slightly larger than the thickness of the introduced laser sheet.

4. **Particle Image Diameter (d_τ):** This is the size of the tracer particle that is captured with the camera.

$$\begin{aligned} d_\tau &= \sqrt{(M \cdot d_p)^2 + (d_{diff})^2} \\ d_{diff} &= 2.44 \cdot \lambda \cdot (1+M) \cdot f^{\#} \end{aligned} \tag{5.4}$$

Here d_p is the physical diameter of the tracer particles, and d_{diff} is the particle image diameter due to the diffraction effects.

5.1.2. Seeding

Seeding is critical for conducting PIV measurements, so it is essential to seed both the primary core flow and the secondary jet flow. A proportionally seeded flow for the cross-flow and the jets are vital in order to prevent a low signal-to-noise ratio. As a result, two different seeding setups are required: one for the cross-flow originating from the upstream W-Tunnel and another for the jet flow emerging from the streamwise slits.

A glycol and water solution is heated for the cross-flow seeding to create fog particles ($1\mu m$) using a SAFEX fog generator. This generator is placed inside the W-Tunnel's inlet before the centrifugal fan to ensure uniformly seeded flow. Failure to achieve homogeneous seeding can lead to various issues, such as inaccuracies in particle tracking and flow field calculation.

A lower seeding density is chosen for the jet flow emerging out from the streamwise slits. This helps to differentiate between the two flows in the test domain. As depicted in Figure 4.17, the settling chamber of the jets is seeded with paraffin seeding using a pressurized seeding generator. The paraffin seeding process involves atomizing molten wax and injecting it along with the jet flow from each streamwise slit. The seeding generator housing the paraffin seeder is pressurized higher than the settling chamber in order to prevent backflow from the settling chamber to the jet seeding generator.

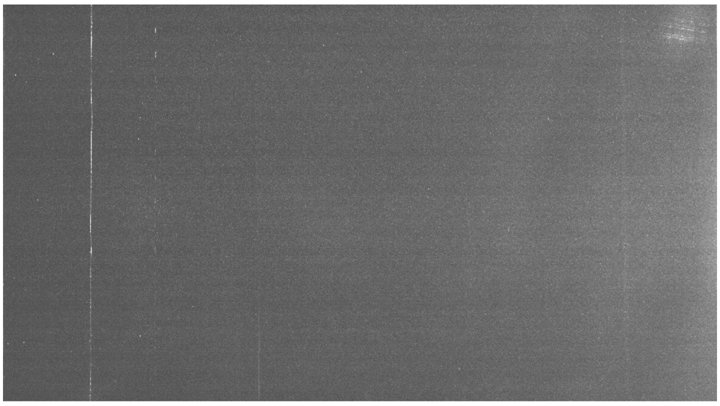

Figure 5.1: Gif for visualizing the proportional seeding in the test section.

The size and density of tracer particles are essential factors to consider while selecting tracer particles for seeding for an experimental campaign. Suppose the size of the seeding particles is too small. In that case, they may not effectively scatter enough light for the camera to detect, necessitating a powerful laser for appropriate illumination. Additionally, very small particles do not follow the behavior of the flow accurately, further leading to higher cross-correlation errors. Conversely, very large seeding particles have a very high repose time. The tradeoff between the size and density of the seeding particles also contributes to the slip velocity. The slip velocity is the difference between the fluid velocity and the velocity of the seeding particles inside the flow due to their distinct physical properties. Therefore, seeding particles should be meticulously chosen to reduce measurement errors and ensure precision.

5.1.3. Illumination

To illuminate the seeding particles, a high-powered double-pulse laser is employed. A PTU box controls the experimental campaign's laser system and can be triggered using LaVision DaVis software for image acquisition. The laser setup utilized is a double-pulse Nd:YAG EverGreen Quantel 200 laser, which features two cavities for generating infrared light at a wavelength of 1064 nm. This wavelength is subsequently halved to 532 nm using a second harmonic generator. According to the experiment's requirements, the acquisition frequency can be adjusted via the LaVision DaVis software. Typically, the laser sheet's thickness is maintained as thin as possible without compromising on the quality of illumination.

Two distinct planes of orientation were taken into account. First, the wall-parallel PIV measurements focus on visualizing the convection of energetic large-scale structures and their interaction with the coherent patterns introduced by various flow control strategies (as illustrated in Figure 5.2a). Second, the zoomed-in wall-normal PIV (as depicted in Figure 5.2b) aids in calculating second-order turbulence statistics along the wall-normal distance, providing insights into the TKE production and RSS profile close to the wall. Brief descriptions of both fields of view are outlined below.

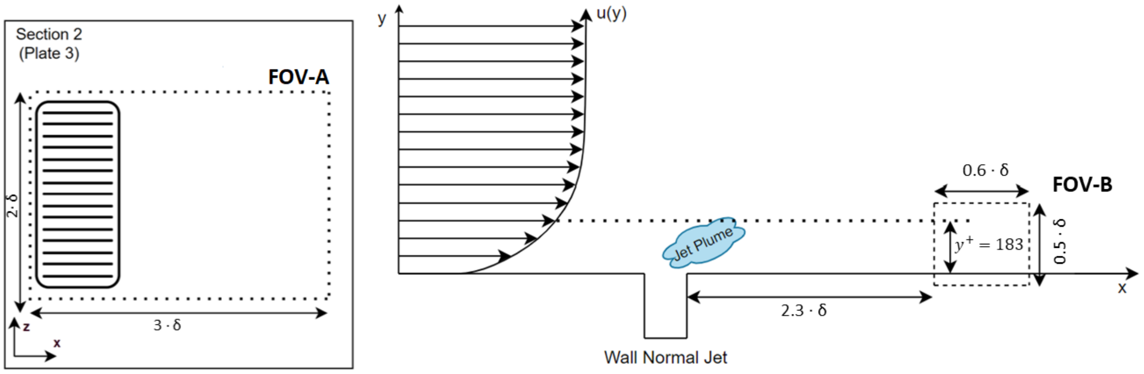

(a) Wall-parallel FOV for PIV measurement.

(b) Wall-normal FOV for PIV measurement.

Figure 5.2: FOV considered during the experimental campaign.

Wall-Parallel FOV/FOV-A: The laser sheet is shinned at the **z-x** plane at a wall-normal height of $y^+ = 183$. This corresponds to the geometrical midpoint of the log region of the formed TBL. A wooden target plate is fabricated to achieve this, keeping the thickness equal to $y^+ = 183$. The laser setup is placed downstream of the test section. Pointing the laser sheet towards the W-Tunnel perfectly cuts across the wall parallel plane and can be visualized in Figure 5.3.

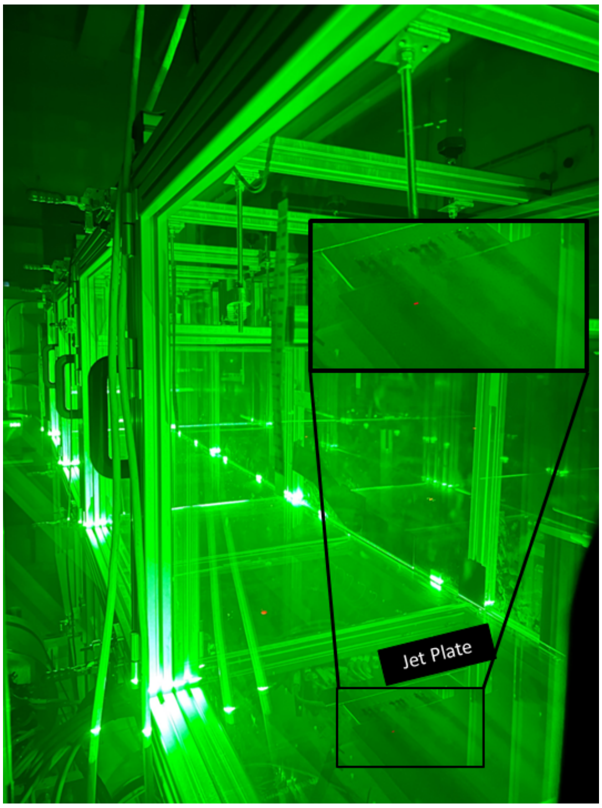

Figure 5.3: Laser sheet shinned parallel to the wall at the height of $y^+ = 183$ or $y/\delta = 0.08$

Wall-Normal FOV/FOV-B: Similar to the wall-parallel plane, the laser setup is placed downstream of the test section. However, to rotate the laser sheet to **x-y** plane, the same set of mirrors is tilted to 90^o. To understand the interaction and influence of individual control cases on the near-wall scales, the wall-normal PIV is measured $2.5 \cdot \delta$ downstream of the origin. Having the turbulence statistics measured at this location will help further understand each control case's global effect. As most of the literature has focused on the local effect of blowing downstream of the jet, a global influence of unsteady blowing is still not established. In subsequent sections, this experimental campaign will attempt to establish the global effect of an active flow control strategy for large-scale manipulation.

5.1.4. Imaging and Data Acquisition

Two sets of camera lenses are needed based on their aperture and focal length specification in order to acquire images for both FOVs effectively. For FOV-A, a large domain of area $2 \cdot \delta \times 3 \cdot \delta$ is captured. Therefore, a *Nikon AF Nikkor 50mm* lens with a minimum $f^{\#} = 1.8$ is used. The aperture of the camera lens is set to $f^{\#} = 5.6$ to focus the camera lens on the infused Safex particles. A rule of thumb is employed to determine the appropriate Δt, ensuring accurate tracer particle displacement. According to this rule, the particle displacement must be at least 10 pixels in any given image pair. Exceeding this value can impact measurement accuracy, while anything lower can lead to pixel-locking issues. Based on this consideration, a $\Delta t = 100 \mu s$ is found to be ideal for the tracer particle displacement in FOV-A.

In the case of FOV-B, a magnified small domain close to the wall is chosen for estimating the turbulence statistics along the wall-normal direction for different control cases. The lens used for FOV-B is *Nikon AF MICRO NIKKOR 200m*, which can go till $f^{\#} = 4$ and is majorly used for microphotography. An aperture of $f^{\#} = 8$ is selected in order to focus the lens on the infused tracer particles illuminated downstream of the origin. Additionally, a smaller Δt is required for FOV-B, as the size of the domain is comparatively smaller. Finally, a $\Delta t = 15 \mu s$ is chosen for FOV-B, allowing for an ideal displacement of tracer particles within the domain without causing pixel-locking issues.

The main acquisition parameters considered for FOV-A and FOV-B are presented in Table 5.1.

-	FOV-A	FOV-B
Laser	Quantel Evergreen laser 2000	
Camera	LaVision sCMOS	
Resolution	2650×2160	
Synchronizer	A Programmable Timing Unit	
Focal Length of Lens	50 mm	200 mm
F-Stop ($f^{\#}$)	5.6	8
FOV	$2 \cdot \delta \times 3 \cdot \delta$	$0.6 \cdot \delta \times 0.5 \cdot \delta$
Δt	$100 \mu s$	$15 \mu s$
Spatial Resolution	$2.95 mm$	$0.29 mm$
Acquisition Frequency	14 Hz	
Images Acquired	2000	1000

Table 5.1: Parameters that were chosen for different FOVs.

As mentioned earlier, the PIV measurements are acquired using LaVision DaVis software. Each control case mentioned in section 4.5 is actuated for both FOVs. A total of 2000 image pairs are acquired for FOV-A to have a convergence solution and to maintain the least statistical uncertainty possible. For FOV-B, 1000 image pairs are acquired, as acquiring 2000 image pairs for a zoomed-in FOV triggers a slowdown in image acquisition. Additionally, the wall-normal velocity profile measured fits well with the DNS solution, indicating the experimental setup's accuracy and influence of the trade-offs made with the total number of image pairs acquired (see section 6.1).

Estimation Of Acquisition Frequency

Phase locking in Particle Image Velocimetry (PIV) occurs when the acquisition frequency of the camera is not correctly tuned with respect to the actuation frequency of the flow. This issue can lead to the camera capturing predominantly a single phase or a limited number of phases of the actuation cycle, resulting in biased measurements and misrepresentation of the actual flow dynamics.

One of the major problems encountered while implementing an active forcing strategy is phase locking. Now, phase locking in PIV occurs when the acquisition frequency of the camera is not correctly tuned with respect to the actuation frequency of the jets. This issue leads to the camera capturing predominantly a single phase or a limited number of phases of the jet actuation cycle. Hence resulting in biased measurements and misrepresentation of the actual flow dynamics. Therefore, if these two frequencies are not tuned properly, the camera misses out on specific parts of the flow cycle.

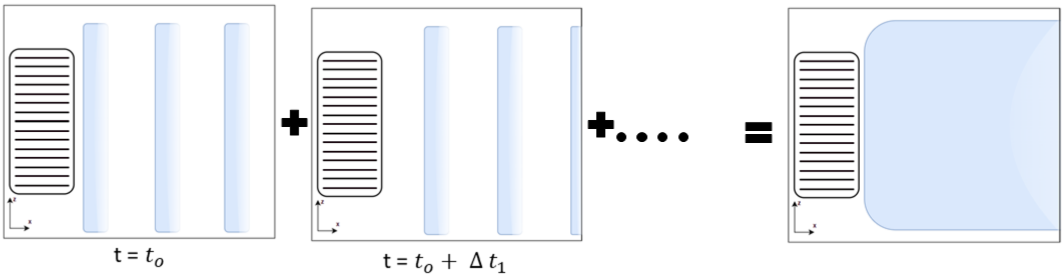

Figure 5.4: Figure illustrated to visualize the phase locking issue.

Figure 5.4 shows a well-resolved PIV measurement without any phase locking issue and can be considered as an ideal case. To implement this, MATLAB's time series of actuation signals are divided into smaller domains and sampled at a particular acquisition frequency. Then, if summing up the contours of all subdomains produces a smooth continuous contour, it can be attributed to a well-resolved PIV result.

To minimize the biasing error across all control strategy cases (considering that the actuation frequency range varies from 6Hz to 48Hz), the acquisition frequency should be carefully selected. Additionally, using a lower acquisition frequency could result in an extended acquisition time for the entire PIV measurement sets, potentially causing the camera or laser setup to slow down. Therefore, a compromise is reached to mitigate these potential errors, and an acquisition frequency of *14Hz* is chosen.

Spatial And Time Filter Application

Despite taking several precautionary steps, such as frequently cleaning with ethanol and masking highly reflecting edges and surfaces via black tap to have a clean domain without any unnecessary laser reflection, the images on LaVision DaVis still contain a few bright fringes. These bright fringes can create problems while estimating flow characteristics close to the wall. To counter this and have an unbiased and uniform result, a pre-processing script comprising a subtracting time filter and a subtracting sliding spatial filter is implemented in LaVision DaVis.

Firstly, the subtracting time filter groups seven individual image pairs and estimates a minimum for them. This minimum is then subtracted from the entire data set. This filter eliminates common bright spots in the selected seven pairs of images. Next to this, a subtracting sliding average spatial filter is applied, assuming a smooth fluid flow without high unphysical fluctuation. This filter first considers a subdomain of 19×19 pixels and estimates a velocity inside it. This fluctuation is then subtracted from the entire set of images reducing the noise or spurious velocities due to wall roughness.

Figure 5.5 shows the effect of these filters on a raw snapshot acquired by LaVision DaVis. As visualized, these filters efficiently removed few reflections near the wall for FOV-B and in of FOV-A. Additionally, the overall noise to signal also increases, which can enable LaVision DaVis to have cleaner correlation peaks.

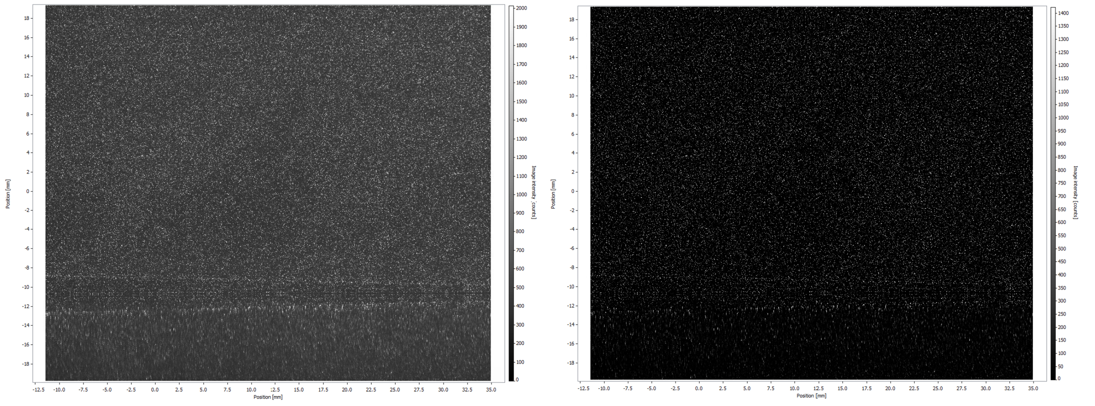

(a) (b)

Figure 5.5: (a) Raw PIV snapshot acquired for FOV-B. (b) Same PIV snapshot after applying a subtracting time filter and a subtracting sliding spatial filter.

After subtracting a time filter and subtracting a sliding spatial filter, multi-pass vector processing is set up. Initially, a geometric mask is applied on the domain to cut off noisy regions of high reflections. Then, for setting up the iterative correlation process, two different strategies are applied for FOV-A and FOV-B. Initially, a window size 32×32 is selected with 50% overlap applied. Then, the results are analyzed, and the window size is reduced until convergence. Eventually, it was found that for FOV-A, a window size of 24×24 with 75% overlap provides the best result without being computationally expensive. Similarly, for FOV-B, a window of size 16×16 with 75% overlap is chosen based on a balance between clean velocity fields, and computational time is taken. Finally, the number of passes is added based on the refinement of the velocity fields and increased until there is no noticeable difference in results. A detailed overview of parameters chosen for each FOV is presented in Table 5.2.

-	FOV-A	FOV-B
Initial Pass	32×32 (2 passes)	24×24 (2 passes)
Final Pass	24×24 (3 passes)	16×16 (3 passes)

Table 5.2: Parameters selected for multi-pass vector processing.

After the vector fields are generated in LaVision DaVis, the data is imported into MATLAB using .csv files for all subsequent post-processing. The instantaneous fluctuating velocity field, processed from the filtered images, can be seen in Figure 5.6. In addition, the formation of a shear layer and the downstream propagation of turbulent eddies from the actuation plate is evident in Figure 5.6.

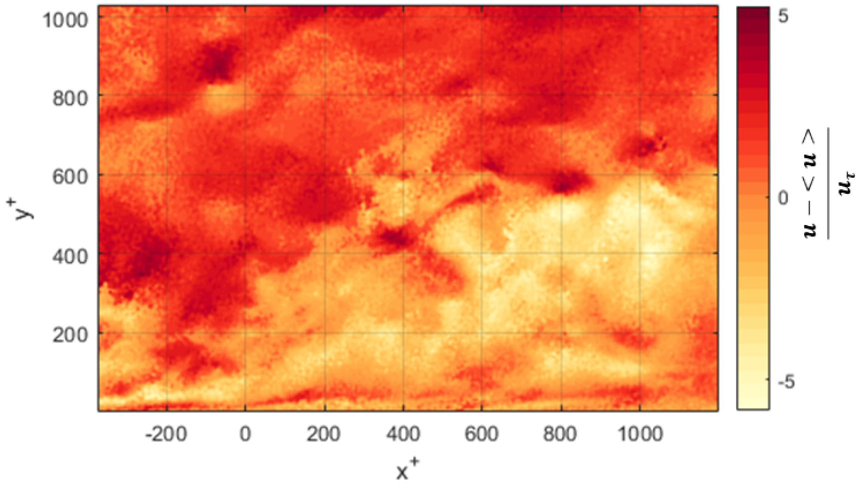

Figure 5.6: Instantaneous streamwise velocity contour processed after applying a spatial and temporal filter.

5.2. Wall Finding Procedure

As mentioned earlier, PIV uses a combination of interrogation window and cross-correlation analysis to estimate the instantaneous velocity fields. However, the velocity gradient near the wall is very steep in wall-bounded turbulence. This leads to significant changes in the particle displacement near the wall, which can result in weak correlation peaks and data loss near the wall. This makes it difficult to directly estimate the location of the wall from the inflection point. Therefore, a wall-finding algorithm is set up to estimate the location of the wall by analyzing the mean velocity profile along the wall-normal direction. Once the location of the wall is known, all the data sets can be shifted accordingly and corrected velocity and turbulence statistics profiles can be acquired.

As depicted in Figure 5.7a, the uncorrected velocity profile is plotted against the wall-normal distance to visualize the inflection point at the edge of the reflection. It is established that the velocity profile behaves linearly very close to the wall (in the linear sublayer). Therefore plotting the velocity gradient can show the highest peak of this gradient, which coincides with the location of the viscous sublayer. However, as seen in Figure 5.7b, the wall-normal PIV acquired for FOV-B is coarsely discretized (has lesser data points inside the liner sublayer). This can create problems in capturing the full range of turbulent scales within the linear sublayer region.

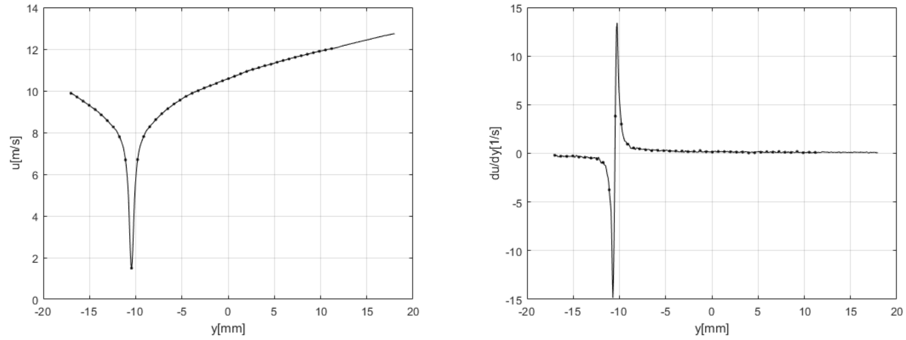

(a) Uncorrected mean streamwise velocity profile of a TBL over a flat plate.

(b) Finding the location of the maximum velocity gradient in the TBL.

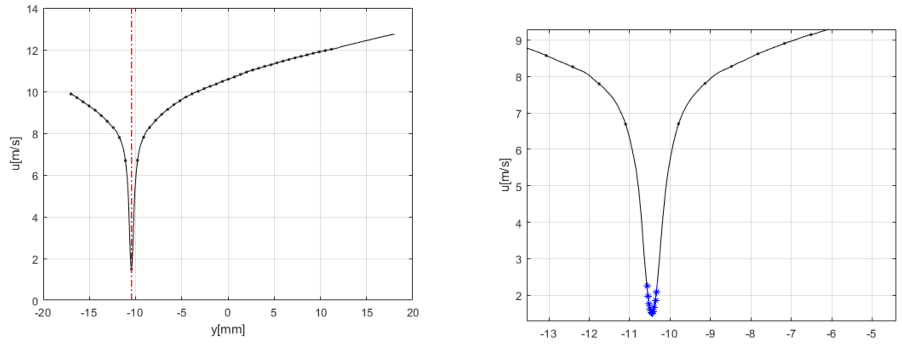

(c) Finding the location of the minimum velocity in the TBL.

(d) Parabolic fit through points near the wall

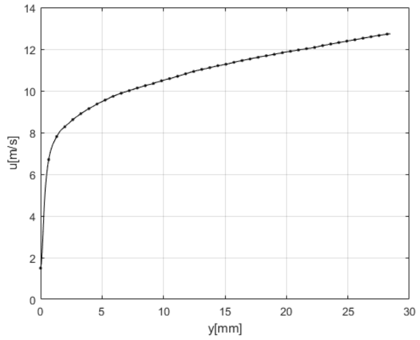

(e) Uncorrected mean streamwise velocity profile of a TBL over a flat plate.

Figure 5.7: Different steps to estimate the wall's location for PIV data measured for FOV-B.

Although a coarse discretization of wall-normal PIV results can limit accuracy in velocity measurements close to the wall, extracting useful information about the flow by analyzing the peaks and trends of particular profiles is still possible. Additionally, this coarsely discretized PIV velocity field can still capture the dominant scales in a TBL and provide helpful information regarding their behavior and interaction. By carefully analyzing the PIV data obtained, it was established that the measurements still provide a useful qualitative understanding. Therefore these results will be used for future analyses in the report. By comparing the PIV results obtained from the same experimental campaign, the effect of these sources of uncertainty can be minimized or neglected, allowing for a more meaningful comparison.

Before estimating the wall location, we assume the wall is perfectly reflecting and provides a symmetrical velocity profile along the edge of the wall and the reflection plane. In the first step, the location of the minimum velocity can be found (as illustrated in Figure 5.7c), and by taking two sets of subsequent points on either side of the minima, a parabola can be fitted. Now, considering the parabola equation, the lowest possible point can be evaluated. This point can then be set as the new location of the wall.

Figure 5.7e shows a corrected velocity profile. The same procedure is further applied for all measured case files to correct the wall location.

5.3. Hot-Wire Anemometer Measurement Setup

Although PIV is a versatile tool providing a larger spatial domain coverage, its temporal resolution still remains limited. The error in approximating velocity within the interrogation window becomes a limiting factor when resolving the spectral energy of velocity fluctuations for individual length scales. As a result, the Hot-Wire Anemometry (HWA) measurement technique is a better alternative. However, HWA also has limitations regarding spatial domain coverage. Therefore, these methods were combined during the experimental campaign for a comprehensive analysis (see Figure 5.8a).

During the experimental campaign, a TSI IFA-300 (CTA) anemometer with a Dantec 55P15 probe acquiring measurements at $51.2KHz$ is set up for HWA measurements (see Figure 5.8b). This probe is a small electric device that can be heated via a power supply. Based on its working principle, an HWA device can be a constant current anemometer(CCA) or a constant temperature anemometer(CTA). For CTA, a constant measured voltage is supplied into the device in order to maintain a set constant temperature. When there is a change in flow conditions near the device, the temperature changes due to heat loss via convection. The probe used for the experimental campaign is $\mathcal{O}(5\mu m)$ in diameter, $\mathcal{O}(1mm)$ in length, and made up of platinum. The whole HWA system can traverse inside the test section with the help of Zaber computer-controlled positioner equipment. This HWA probe is connected to the Wheatstone Bridge. This bridge contains a total of four resistors, including the probe. As the resistance of a metal increases along with temperature, a flow condition change near the probe can increase or decrease the local temperature near the probe, changing its resistance. This imbalance is detected by a high-gain DC amplifier which gives an output in terms of voltage.

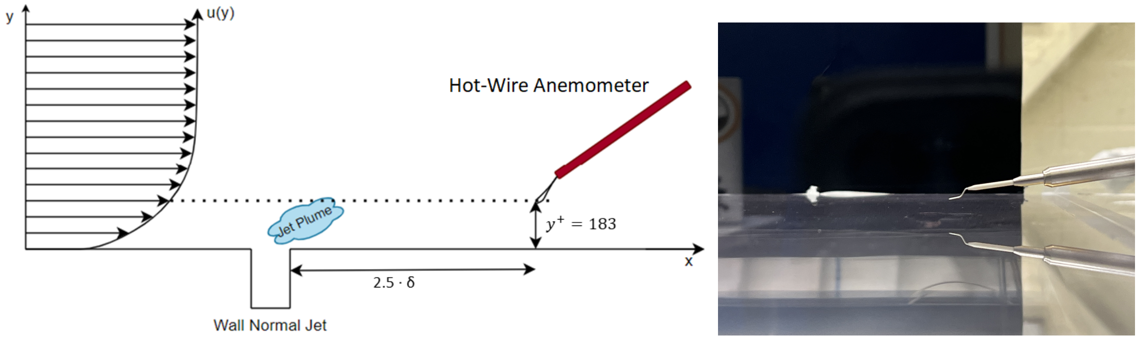

(a) **(b)**

Figure 5.8: (a) HWA measurement setup for the experimental campaign; (b) Dantec probe placed in the middle of the log region of incoming TBL.

Before experimentation, the initial resistance of the wire needs to be determined. This can be done via setting the overheat ratio(a) (given in Equation 5.5).

$$a = \frac{R_w - R_0}{R_0} = \alpha_0 \left(T_w - T_0\right) \tag{5.5}$$

The variable R_w represents the resistance of the wire when hot, T_w and T_0 represent the wire's temperature at the working conditions and room condition, respectively. This overheat ratio (a) is usually set between 0.5 to 0.8. However, at $a = 0.8$, the overheat ratio is too high, causing the wire to cool off faster and causing damage to the probe wire.

The HWA is calibrated using a formulation called King's law (refer to Equation 5.6). Here the E represents the voltage, A and B are the constants depending on the flow properties. U is the flow velocity and n is usually taken as 0.4, which represents a 4th order polynomial relation between voltage E and flow velocity U.

$$E^2 = A + B \cdot U^n \tag{5.6}$$

While calibrating the HWA, the 4th order equation derived from King's law needs to be fit to the measured data points. Therefore, 50 different HWA measurements are taken from logarithmically spaced wall-normal locations with the help Zaber traverse mechanism. This helps to plot an interpolation curve for voltage and flow velocity. This plot is used as a calibration curve for the HWA probe. To have a higher temporal resolution of the streamwise velocity components and to observe the effect of each control case, the HWA probe is placed at the location of (x^+, y^+, z^+) = (5722,183,0) corresponding to $2.5 \cdot \delta$ downstream of the trailing edge of jet. This wall-normal location coincides with the middle point of the log region.

5.4. Uncertainty Analysis

PIV being an experimental technique, is subjected to different sources of error. These uncertainties can occur due to several reasons ranging from statistical uncertainties to cross-correlation uncertainty. Hence these can affect the reliability of measurements. In order to contain these uncertainties, it is essential to understand and quantify their effect to assess the quality of the results. A few of the significant sources of uncertainties are discussed below.

5.4.1. Statistical Uncertainty

Benedict and Gould, 1996 defined statistical uncertainty as an inherent variability of the measured data that cannot be eliminated but can be contained with near-perfect measurements. They explained that one way of quantifying the uncertainty is by the standard deviation. The standard deviation measures the dispersion of measured values around the mean; hence a higher standard deviation means a higher data variability.

$$\epsilon_u = \frac{\sigma}{\sqrt{N}} \tag{5.7}$$

Here σ denotes the standard deviation of the measured data, and N is the total number of samples obtained during the campaign. The Equation 5.7 function computes the standard deviation of the measured data and the sample size. As the number of samples increases, the data distribution transforms into a normal distribution with a standard deviation proportional to the square root of the instantaneous fluctuating velocity component. Consequently, the statistical uncertainty reduces as the number of samples acquired increases.

5.4.2. Cross-Correlation Uncertainty

Raffel et al., 2007 described the cross-correlation uncertainty as the accuracy of the displacement measurements due to factors such as image quality, the accuracy of the cross-correlation algorithm, etc. These factors affect the correlation peak intensity and are subject to noise and errors. Therefore, this inaccuracy displacement measurement can be translated to an error in terms of $[m/s]$ for better assessment [Raffel et al., 2007].

$$\epsilon_{cc} = \frac{\epsilon_c}{k\delta_t} \tag{5.8}$$

Here k represents the image resolution in terms of [px/mm], δ_t is the laser pulse separation, and ϵ_c is the correlation uncertainty which is approximately 0.1 [px] for planar PIVs. Many pieces of literature estimated this value at 0.1. However, it is important to note that this value can vary depending on the experimental setup and image quality.

5.4.3. Uncertainty Estimation

In conclusion, considering the discussed sources of uncertainties, a quick estimation of these uncertainties is calculated for the experimental campaign for both FOVs. As FOV-A covers a more extensive domain for analyzing the organization of LSMs, it has higher uncertainties than FOV-B. Taking this into account, a more significant number of images were acquired for FOV-A compared to FOV-B. The out-of-plane velocity components are not recorded since the experimental campaign employed a planar PIV. This makes it impossible to estimate uncertainties for all velocity components for both FOVs. Table 5.3 summarizes the uncertainty values approximated for the experimental campaign.

Source Of Uncertainty	**FOV-A**	**FOV-B**
ϵ_u	0.049 [m/s]	0.066 [m/s]
ϵ_v	-	0.038 [m/s]
ϵ_w	0.032 [m/s]	-
ϵ_{cc}	0.123 [m/s]	0.121 [m/s]

Table 5.3: Estimated uncertainties for the experimental campaign.

The statistical uncertainties for both FOVs are well below 10% of the friction velocity (u_τ). This uncertainty level is acceptable for most turbulence research applications because it indicates that the PIV measurements are accurate enough to capture the essential flow dynamics and provide meaningful insights into flow behavior. For cross-correlation uncertainty, the estimated uncertainty is around 24% of the frictional velocity. However, this FOV-A is mainly acquired to analyze the organization of the large energetic scales. As a result, a larger FOV was considered to capture the maximum portion of the convecting LSMs without obscuring their true length. This resulted in comparatively lower-resolution images for FOV-A compared to FOV-B. However, when the uncertainty is compared with the mean velocity at the midpoint of the log region, the cross-correlation uncertainty is less than 1.5%. In conclusion, we need to be more critical while interpreting different control cases in terms of second-order turbulence statistics as they are more prone to noise.

6

Results And Discussions

This chapter examines the results obtained from FOV-A and FOV-B for all control cases. Before evaluating the effectiveness of each control case, the uncontrolled base case is compared to DNS results under similar boundary conditions to validate the experimental setup. Following this, the wall parallel velocity contours are analyzed to understand how the cross-flow interacts with different control cases. Understanding the mean fields is crucial for identifying the organization and location of energetic large scales. Moreover, mean velocity fields and two-point correlation contours are key for detecting potential errors while implementing individual control cases. After analyzing the velocity contours, examining the second-order turbulence statistics profile meaningfully becomes simpler. This, in turn, allows for a qualitative evaluation of the flow behavior.

6.1. Uncontrolled Canonical Turbulent Boundary Layer

Before investigating the impact of different control cases, it is essential to verify the credibility of the experimental setup and flow conditions. Consequently, this section discusses the formation of the TBL in Case 0, which corresponds to an uncontrolled or no-forcing case. These results can be used for benchmarking the test results against existing DNS results with similar boundary conditions. This ensures the credibility of the setup while enabling comparisons between individual control cases and with the uncontrolled base case. The DNS results produced by Jimenez and Hoyas, 2008 is for a similar ZPG TBL condition with a $Re_\tau = 2003$. Therefore the corresponding DNS data is used for comparison with PIV measurements.

Figure 6.1a illustrates the inner-scaled mean velocity profile for the streamwise velocity component (u) of the uncontrolled base case compared to the DNS data. The *red line with star marker* represents Case 0. However, the number of markers for Case 0 does not signify the number of data points in the region; instead, it helps distinguish it from other control cases. For easier comparison, this legend styling for Case 0 will be kept consistent throughout the rest of the report. As shown, the experimental results overlap the DNS results from the wall until $y^+ = 400$. The discrepancy after that can be attributed to the fact that the DNS results were obtained for a channel flow that displays different characteristics away from the wall. As discussed earlier, the PIV results near the wall should be interpreted cautiously. This is because of very steep velocity gradients and noise close to the wall. These effects can create a correlation error, resulting in inaccurate particle displacement. Therefore, to minimize this impact on the overall result, practitioners should exclude the measurement data inside half the size of the interrogation window (8 [px] for FOV-B) adjacent to the wall.

Consequently, the first *red dashed line* on all future graphs represents 8 [px] away from the wall, i.e., at $y^+ = 4.9$. The data points before this y^+ unit should be interpreted with caution to avoid drawing any firm conclusions; instead, it is necessary only to focus on the trend of velocity profiles to compare the results of different control cases under the same experimental condition. The following three green dash lines separate the TBL region in wall-bounded turbulence into four regions based on the non-dimensional wall unit y^+ as visualized in Figure 6.1. The four regions are the viscous sublayer, buffer layer, logarithmic layer, and wake. For more information, refer to section 2.2. These markings will be kept consistent for all future graphs for better analysis of flow features and their location from the wall.

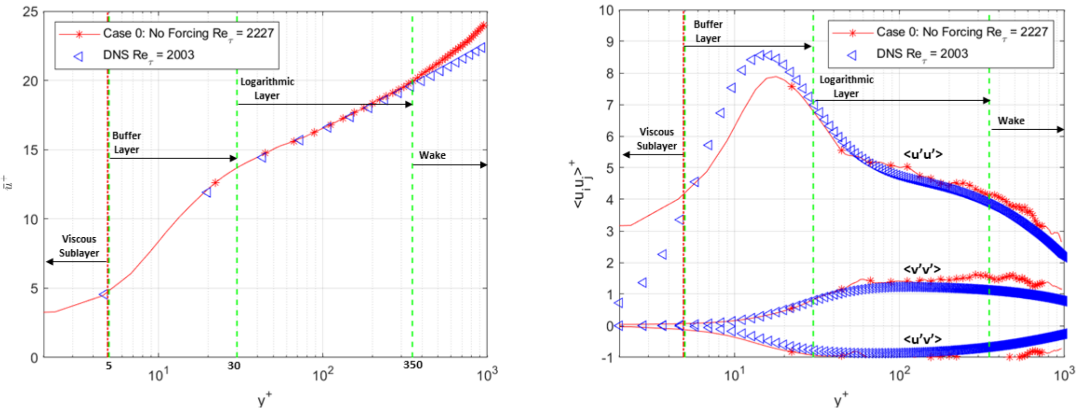

(a) **(b)**

Figure 6.1: (a.) Mean streamwise velocity profile scaled with inner variables of a TBL over a flat plate. (b.) Mean Reynolds stresses profile scaled with inner variables of a TBL over a flat plate.

Unlike Figure 6.1a, Figure 6.1b shows a little offset in $< u'u' >$, which is the Reynolds shear stress associated with streamwise velocity component. This offset in PIV results till $y^+ = 15$ can be attributed to the fact that there were limitations to PIV near the wall. One is the susceptibility to noise for second-order statistics near the wall due to large velocity fluctuations. Second is an error in correlation peaks due to reflection and noise. In addition, PIV and DNS setups differ in numerical schemes and boundary conditions used, which can create this offset. However, except for this offset near the wall, both trends overlap for the rest of the domain, indicating the credibility of the results.

6.1.1. Friction Velocity Estimation

The law of the wall can be used to approximate the frictional velocity. This law relates the mean velocity profile in the TBL to frictional velocity via Equation 2.15. Once the mean velocity profile is measured from the PIV results, it is then fit to the law of the wall and solved for the frictional velocity u_τ. Since it is crucial to accurately estimate u_τ for scaling in TBL for different result comparisons, the u_τ measured in the previous campaign for the same experimental setup and flow conditions will be used in all future cases (see Table 4.1). Additionally, the PIV results obtained for this campaign are susceptible to steep gradients near the wall. Therefore, the u_τ calculated from PIV results might be biased. Moreover, when the wall-normal FOV-B results are carefully observed, they lack the entire wake region, and only up to $y^+ = 1000$ is captured. This limits the ability to fit the velocity profile perfectly for friction velocity estimation. Therefore, a composite fitting is used to estimate the friction velocity from the previous campaign measurements. The composite fitting procedure is one of the most accurate methods for flow characteristics estimation, as it fits the mean profile to a composite exponential Musker function. The composite fit enables the TBL profile to be fitted from the viscous sublayer to the wake layer, making it one of the most accurate techniques for frictional velocity approximation.

6.2. Mean Flow Field Organization

Analyzing the mean velocity contours in the middle of the log region will initially aid in understanding the organization of large-scale structures over a flat plate. The log region is characterized by the presence of LSMs, which play a crucial role in transporting momentum and energy in the TBL. Therefore, performing wall-parallel PIV will first validate the arrangement of LSMs with results from Hutchins and Marusic, 2007a as visualized in Figure 2.13. These plots will assist in analyzing the impact of spanwise traveling waves on the organization of LSMs.

As observed in Figure 6.2, the mean streamwise velocity contour is not continuous. This discontinuity can be attributed to several minor reasons, such as non-uniform laser sheet thickness within the domain, leading to a relatively thicker laser sheet in one region. Additionally, a slight curvature in the wall might also contribute to the non-uniformity in velocity contours. To account for this non-physicality of the wall, the velocity contours of all control cases will be normalized by the uncontrolled base case.

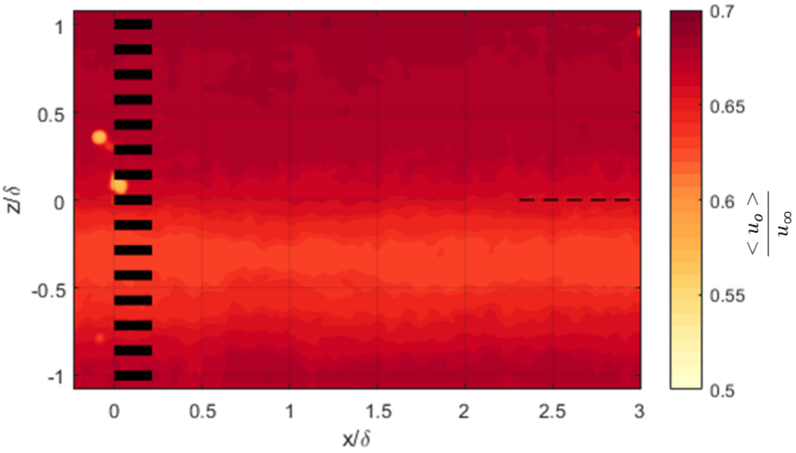

Figure 6.2: Mean streamwise velocity $< u >$ contour for Case 0: No Forcing normalized with free stream velocity $(u_\infty = 15m/s)$ at $y^+ = 183$ or $y/\delta = 0.08$

One of the significant features observed in all streamwise mean velocity $< u >$ contours is the formation of the shear layers from the sides of the domain (see Figure 6.4). These shear layers are again formed due to the slowing down of fluid particles at the edges of the test section. Therefore the decision to include multiple streamwise slits covering the entire spanwise length was necessary to have an unbiased result in the middle of the domain.

6.2.1. Standing Wave (SW)

As shown in Figure 6.4, the fifteen black strips represent the locations of fifteen streamwise jet slits. The black dotted line on the right of the domain represents the acquisition location of the wall-normal/FOV-B plane. A smoother contour was expected from FOV-A measurements. The non-uniform coherent structures vaguely visible in all of the mean images in Figure 6.4 can be attributed to the fact that the overall percentage of *Jet on time* was more than *Jet off time*. This minute phase locking issue happened even though great care was taken to avoid it. After careful investigation, it was established that the acquisition frequency, even though set to $14Hz$, was not constant throughout all the control cases. After taking several precautionary steps, such as acquiring images in small batches to prevent the laser system from heating up and slowing down, the acquisition frequency drops down as the day progresses. Even though the acquisition is initially carried out at 14Hz, in the following cases, the acquisition frequency drops from 14Hz to 12Hz and continues dropping until 5Hz in the middle of the day. This reason is the primary cause of the phase locking issue in PIV measurements. Analyzing the individual jet actuation data and Q-Switch data from the PIV setup can provide insight into the extent of phase locking for the measurements.

The jet actuation data provides information regarding the timing and duration of the individual jet actuators. For example, analyzing this jet actuation data with the timing of Q-Switch data will provide information on the proportion of *Jet on time* to *Jet off time*. As seen in Figure 6.3, the degree of phase locking diminishes as the actuation frequency increases. This observation could be coincidental since the slowdown of the PIV setup was not linear. Nevertheless, a conclusion can be drawn that, at most, the *Jet On time* was only 7% higher than the *Jet Off time*. Thus, using the PIV results with such a low phase locking can still be valuable for understanding the flow field under different control cases. Moreover, turbulence statistics will serve as a primary tool for estimating the effects of various control cases, and as these are calculated from wall-normal PIV measurements averaged at a downstream distance of $2.5 \cdot \delta$, the individual effects of jets will most probably not be noticeable. Instead, a combined effect of blowing through multiple streamwise slits is expected to be seen at FOV-B.

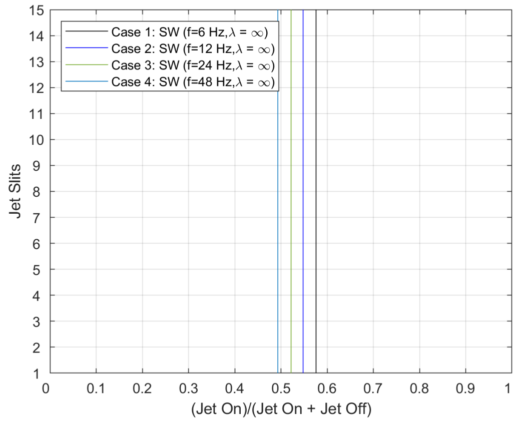

Figure 6.3: Jet actuation plotted for individual jet slit from the Q-switch data for all SW cases.

One of the striking characteristics seen in Figure 6.4 is the expansion of low-speed areas downstream of the jet array as the actuation frequency rises. This pattern may be attributed to several possible explanations. One such reason is that the low-speed region is situated in the wake of the jet. As a result, a noticeable low-speed area emerges when compared to the uncontrolled base case. Therefore, as the actuation frequency increases, the jets create more frequent low-speed regions downstream, which can be observed in the mean velocity field. This could be due to the increased interaction between the jets and the incoming turbulent boundary layer, altering the flow characteristics downstream. Additionally, as the maximum amplitude reached for an actuator during its blowing phase is reached during its starting phase. With an increase in actuation frequency, the jet and cross-flow interaction increases. This creates comparatively larger reduced velocity zones compared to the uncontrolled base case. However, as these are mere speculations regarding the reduced velocity region downstream of the jet plate, further insight might be gained after analyzing different instantaneous fields.

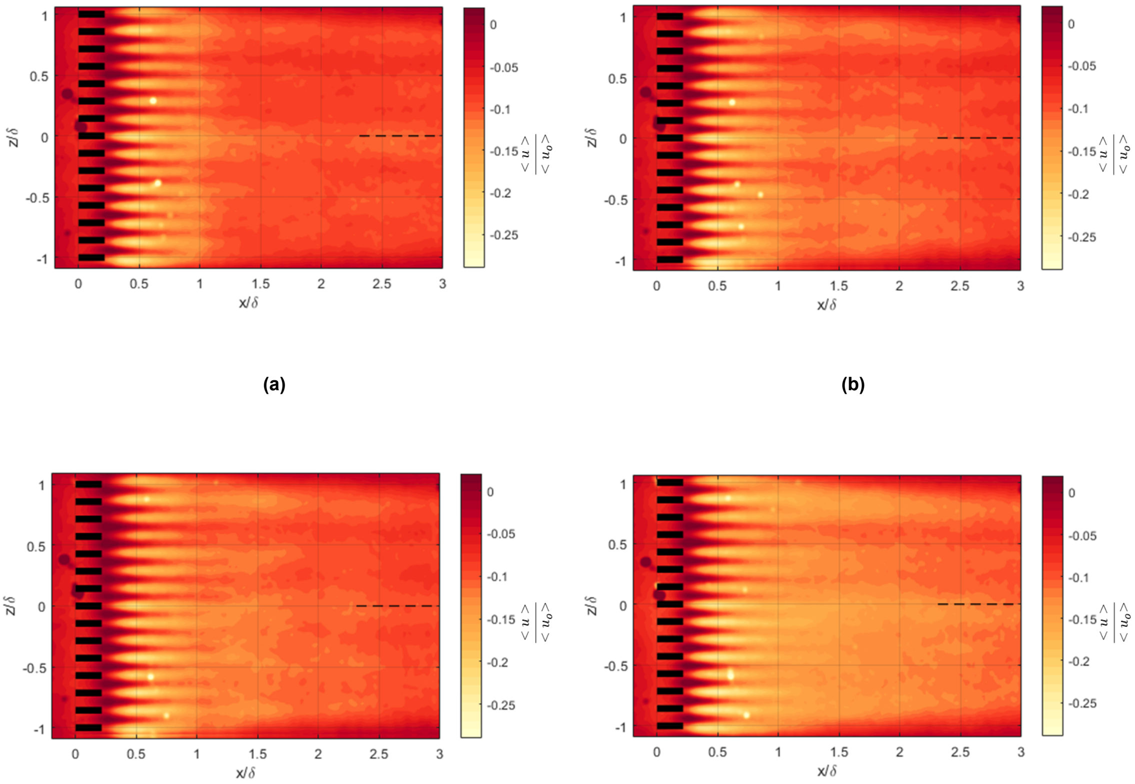

(a)

(b)

(c)

(d)

Figure 6.4: Mean streamwise velocity $< u >$ contour for (a.) Case 1: SW (f = 6Hz, $\lambda = \infty$); (b.) Case 2: SW (f = 12Hz, $\lambda = \infty$); (c.) Case 3: SW (f = 24Hz, $\lambda = \infty$); (d.) Case 4: SW (f = 48Hz, $\lambda = \infty$) normalized with Case 0: No Forcing/uncontrolled case at $y^+ = 183$ or $y/\delta = 0.08$.

6.2.2. Traveling Wave (TW)

A notable effect observed in Figure 6.5 is the presence of finger-like patterns convecting downstream of the jet slits. These patterns closely resemble those in Figure 4.12 and are observed due to phase locking with a few specific jet slits. As the *jet on time* for these particular jet slits is comparatively higher than the remaining jet slits, these frequently introduced spanwise traveling waves are visible in Figure 6.5, appearing locked at a particular instance in time. However, after analyzing Figure 6.6, a maximum of 6% phase locking for *jet on time* was found. Therefore, considering the similar arguments as presented in the previous section, these results are accepted for future analysis.

Upon comparing the inclination and behavior of the finger-like structures observed in Figure 6.5 and Figure 4.12, it becomes evident that the interaction between the introduced spanwise traveling wave and the incoming TBL, as well as the LSMs convecting downstream of the jet plate, lead to significant changes. Furthermore, the inclination angle appears to increase as the actuation frequency rises. At $f = 48Hz$, the mean streamwise velocity contour shown in Figure 6.5d is strikingly similar to that in Figure 6.4d. However, it can be speculated that the reduced velocity region downstream of the jet plate for a TW control strategy is due to the sudden creation of spanwise shear, which interacts with both the near-wall scales and existing LSMs, causing them to break down [Quadrio and Ricco, 2004]. Moreover, the interaction between the introduced coherent pattern and TBL may lead to further non-linear interactions with LSMs, resulting in their breakdown. These explanations, however, are speculative at best. The following sections will delve deeper into the analysis of instantaneous velocity fields to better comprehend the underlying physics behind the reduced velocity field downstream.

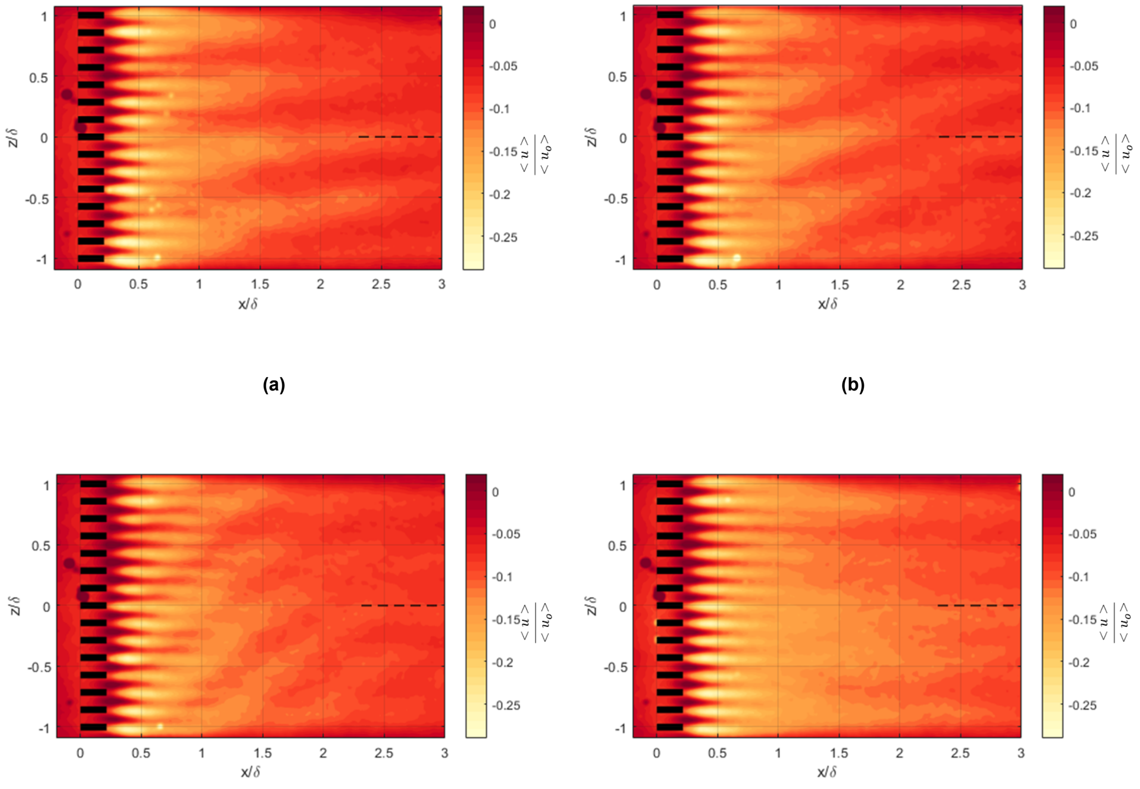

(a) (b)

(c) (d)

Figure 6.5: Mean streamwise velocity $< u >$ contour for (a.) Case 5: TW (f = 6Hz, $\lambda = 0.8 \cdot \delta$); (b.) Case 6: TW (f = 12Hz, $\lambda = 0.8 \cdot \delta$); (c.) Case 7: TW (f = 24Hz, $\lambda = 0.8 \cdot \delta$); (d.) Case 8: TW (f = 48Hz, $\lambda = 0.8 \cdot \delta$) normalized with Case 0: No Forcing/uncontrolled case at $y^+ = 183$ or $y/\delta = 0.08$.

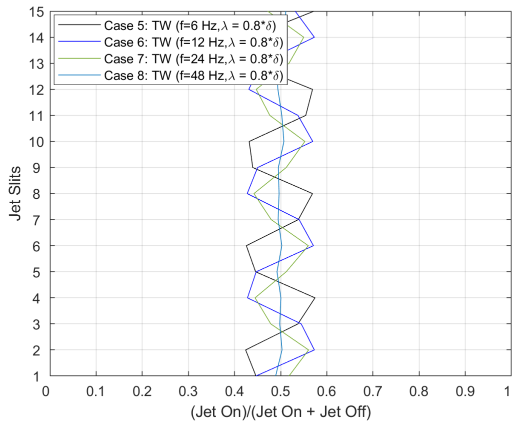

Figure 6.6: Jet actuation plotted for individual jet slit from the Q-switch data for all SW cases.

6.3. Instantaneous Flow Field Organization

Examining the wall-parallel instantaneous velocity contours can offer valuable insights into the orientation and interaction of the introduced coherent patterns. Unlike averaged velocity contours, which present a temporally averaged view of the flow field, instantaneous velocity contours capture the flow structure's spatial and temporal fluctuations. The instantaneous fields should be sampled at a specific moment after the *jet on* command is sent to the NI board to conduct an unbiased analysis of various control strategies. The ideal sampling time would be when the jet plume reaches the middle of the log region from the jet slits embedded in the wall. This approach ensures that the flow is in a comparable state. Furthermore, since the jet plumes are directed towards the LSMs convecting in the log region, this region is susceptible to the different actuation phases. Once the jet plume reaches the log region and stabilizes, the transient effect of the jet can be disregarded. From a previous campaign, Dacome, 2022a determined that it takes $4ms$ for the jet to emerge from the slits after the *jet on* command is issued. Upon actuation, the jet plume rises until it reaches a maximum jet exit velocity, slightly higher than the preset jet exit value [Dacome, 2022a]. However, following this point, the jet exit velocity decreases before stabilizing at the set velocity. The time required for the jet plume to reach the midpoint of the log region and get stable is $5ms$. Thus, it takes a total of $9ms$ for an individual jet slit to become actuated and reach a stable condition in the log region.

6.3.1. Standing Wave (SW)

One of the initial distinctions between different actuation frequencies for the SW control strategy is the extent of the reduced velocity region downstream of the jet plate. This pattern closely resembles the $z-x$ diagram (see Figure 4.11). The extent of the low-speed region downstream is directly proportional to the actuation time for individual jet slits. For instance, at a lower actuation frequency, the total duration of *jet on time* is comparatively more prolonged than that of a higher actuation frequency. Consequently, the streamwise length of the introduced coherent pattern is relatively larger for lower actuation frequency cases than those with higher actuation frequencies.

As a result, with increased actuation frequency, the streamwise length of the introduced coherent pattern decreases. This occurs because, at higher frequencies, the time interval between successive jet actuation decreases, leading to the formation of smaller and more frequent coherent patterns. Although this trend was anticipated earlier, one significant observation is the discrepancy between the expected streamwise length (recall Figure 4.11) and the actual streamwise length observed in Figure 6.7. The expected streamwise length of coherent patterns introduced by jet actuation was more prominent and longer than in Figure 6.7. This difference can be attributed to the interaction between the incoming TBL and the introduced coherent pattern. Such nonlinear interactions can lead to the formation of new structures or the breakup of existing ones.

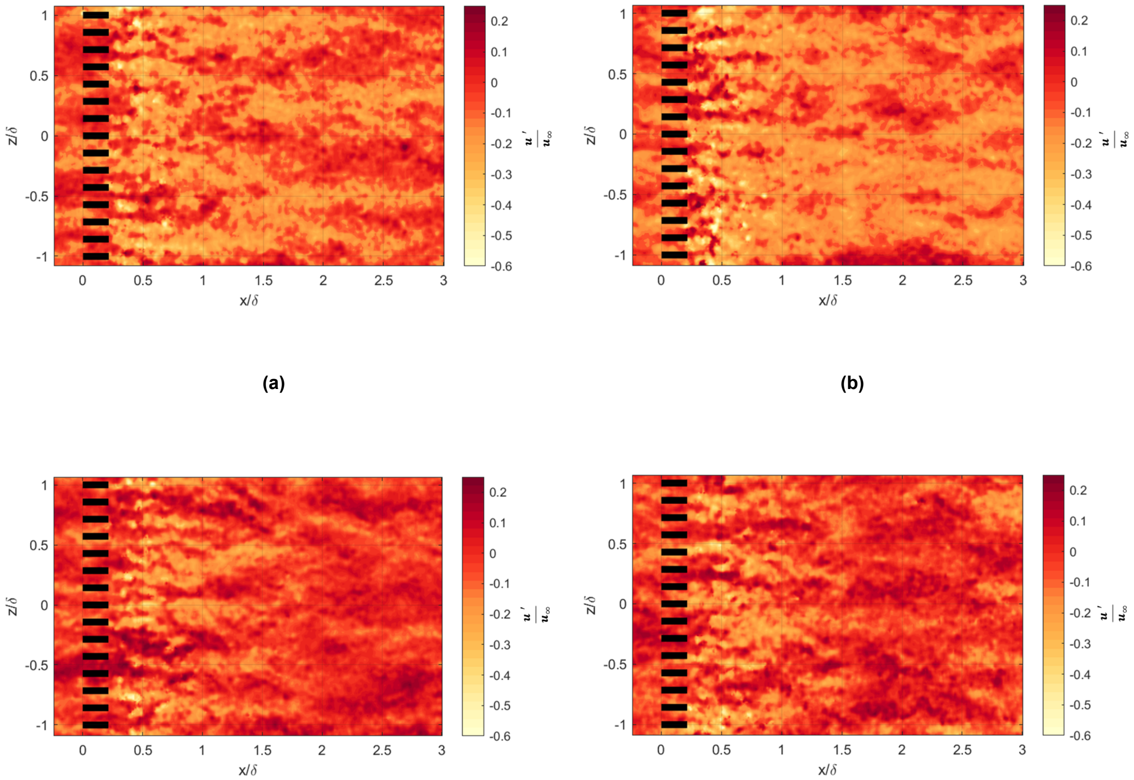

(a)

(b)

(c)

(d)

Figure 6.7: Instantaneous streamwise fluctuating velocity (u') contour for (a.) Case 1: SW (f = 6Hz, $\lambda = \infty$); (b.) Case 2: SW (f = 12Hz, $\lambda = \infty$); (c.) Case 3: SW (f = 24Hz, $\lambda = \infty$); (d.) Case 4: SW (f = 48Hz, $\lambda = \infty$) normalized with freestream velocity ($\frac{u'}{u_\infty}$) at $y^+ = 183$ or $y/\delta = 0.08$.

6.3.2. Traveling Wave (TW)

The introduced inclined coherent patterns for spanwise traveling waves are visible as regions of lower speed convecting downstream, as seen in Figure 6.8. However, the inclination angle depends on the actuation frequency, scale convection velocities, and scale interaction. This discrepancy can be attributed to the failure of Taylor's frozen hypothesis, which is based on theoretical models. The incoming TBL may also disrupt the coherence of introduced patterns, altering their inclination angle. A phenomenon commonly observed in all of the images presented in Figure 6.8 is the meandering of the introduced coherent pattern downstream of the jet plate. The lateral displacement from the fluctuating velocity component of the incoming TBL causes this. This effect influences the overall flow properties and can impact the organization of introduced coherent structures.

There are more effective approaches than the wall-parallel PIV measurements for discerning differences in the receptivity of near-wall scales towards each control case. Measurements performed for FOV-B can reveal these differences through second-order turbulence statistics. However, the mean velocity field and instantaneous velocity field for FOV-B are not discussed further because, although the influence and coherence of introduced patterns are maintained until a downstream distance of 2.5δ, the interaction between these large streaks and near-wall small scales is not particularly significant in terms of velocity contour visualization.

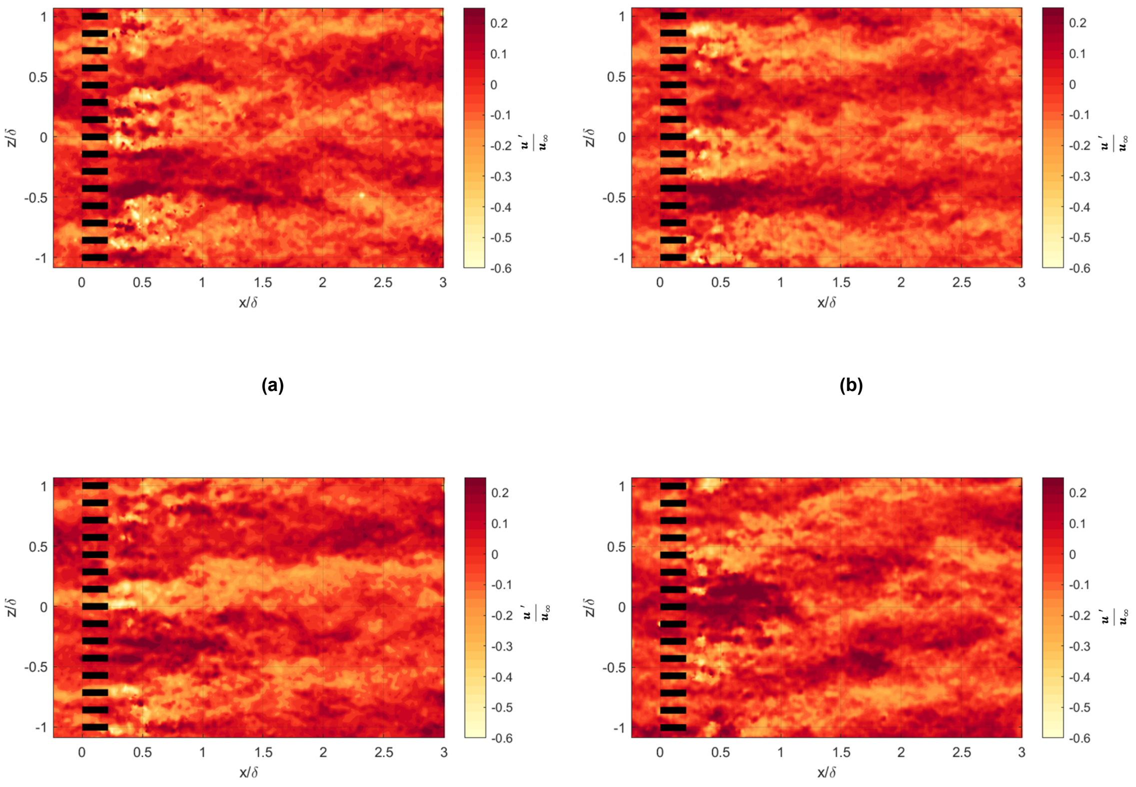

(a)

(b)

(c)

(d)

Figure 6.8: Instantaneous streamwise fluctuating velocity (u') contour for (a.) Case 5: TW (f = 6Hz, $\lambda = 0.8 \cdot \delta$); (b.) Case 6: TW (f = 12Hz, $\lambda = 0.8 \cdot \delta$); (c.) Case 7: TW (f = 24Hz, $\lambda = 0.8 \cdot \delta$); (d.) Case 8: TW (f = 48Hz, $\lambda = 0.8 \cdot \delta$) normalized with freestream velocity ($\frac{u'}{u_\infty}$) at $y^+ = 183$ or $y/\delta = 0.08$.

6.4. Two-Point Correlation

Two-point correlation is one of the most important tools to analyze the scales' statistical structure in a TBL. Unlike, as previously mentioned, averaged streamwise velocity contours ($\frac{<u>}{<u_o>}$) and instantaneous streamwise velocity contours ($\frac{u'}{u_\infty}$), two-point correlation enables analysis of statistical properties of the flow over a range of spatial and temporal scales. Therefore, this tool becomes particularly useful for analyzing the correct implementation of different control cases via analyzing the statistical structure of introduced coherent patterns and deducing its interaction in existing high and low momentum zones.

For uncontrolled base flow, the averaged two-point correlation contours show the existence of a highly correlated zone in the middle of the domain that is flanked by two anti-correlation zones. It can also be concluded that the Figure 6.9 resembles Figure 2.13. The comparison of both plots ensures the legitimacy of the experimental setup used for the campaign. The highly positive correlation region in the middle of the domain represents the presence of large-scale structures (previously mentioned as "LSMs/Superstructure"). The flanked anti-correlation zones on each side confirm the presence of alternate high-speed and low-speed zones in the spanwise direction. The spanwise width of these LSMs has been estimated to be $0.4 \cdot \delta$ in the middle of the domain [Hutchins and Marusic, 2007a] and can be seen in Figure 6.9 and Figure 6.9. However, the true length of these LSMs is still not captured inside the FOV. This is because the streamwise length of these convecting LSMs is around $6 \cdot \delta$. However, there are reports regarding the true streamwise length to be around $20 \cdot \delta$, and the discrepancy in streamwise length is due to the spanwise meandering effect [Hutchins and Marusic, 2007b; Hutchins et al., 2011]. The spanwise meandering of convecting LSMs occurs due to the interaction between turbulent fluctuation and LSMs. Due to this interaction, the LSMs get distorted and displaced in a spanwise direction, creating an alternate streamwise velocity pattern downstream. This phenomenon obscures the true length of the LSMs.

Using a Gaussian filter can be advantageous for filtering the dominant large scales and analyzing the impact of different control cases on their organization. The Gaussian filter convolves the correlation contour with a Gaussian function, which then smooths out lower energy small scales and background noise. A Gaussian filter with a window size of $0.4 \cdot \delta \times 0.4 \cdot \delta$ is utilized since the dominant coherent structures have a spanwise width of $0.4 \cdot \delta$ in the middle of the domain. Moreover, this filter will also facilitate the analysis of differences in the organization of introduced coherent patterns for various control cases. For example, Figure 6.10 shows a filtered two-point correlation contour for an uncontrolled/base case. As anticipated, applying the Gaussian filter increases the spanwise width of captured LSMs near the edges. Nonetheless, the organization and trend of formation remain intact after filtration. Consequently, all of the two-point correlation contours presented in subsequent sections are filtered using a Gaussian function with a window size of $0.4 \cdot \delta \times 0.4 \cdot \delta$ for improved comparison.

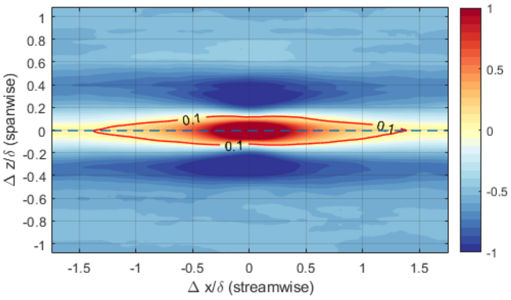

Figure 6.9: Unfiltered two-point correlation contour of streamwise velocity fluctuations for Case0: No Forcing at $y^+ = 183$ or $y/\delta = 0.08$.

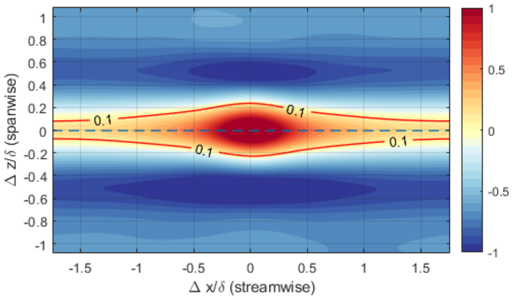

Figure 6.10: Filtered two-point correlation contour of streamwise velocity fluctuations for Case0: No Forcing at $y^+ = 183$ or $y/\delta = 0.08$.

6.4.1. Standing Wave (SW)

Figure 6.11 presents the two-point correlation contours for all the SW control strategies. A notable trend observed in the two-point correlation contours for different actuation frequency cases is the extent of the highly correlated zone downstream of the jet plate for lower actuation frequency cases. As the actuation frequency increases, the highly positive correlated zones shrink in size. The anticipated trend from previous results is also seen here. As the actuation frequency increases, the streamwise width of the introduced coherent pattern decreases; however, this spatial width is inconsistent throughout the spanwise domain. As observed in Figure 6.11a, Figure 6.11b, and Figure 6.11d, the two flanking zones on the side containing the anti-correlation regions (recall Figure 6.10) interact with the introduced coherent pattern and reduce the intensity, resulting in this inconsistency in the spanwise domain. In a TBL, the spanwise coherence is not maintained due to the spanwise meandering effect, which disrupts the coherence of convecting large scales. However, the spanwise coherence is preserved only for Figure 6.11c.

Ideally, all two-point correlation contours should be symmetrical along the reference line (marked as the dotted line in the middle of the domain). However, a slight asymmetrical behavior is observed in all two-point correlation contours. This is due to the uneven thickness of the laser sheet compared to the wall, which was also observed in Figure 6.2. One significant takeaway from Figure 6.11 is the effective implementation of the intended control strategy.

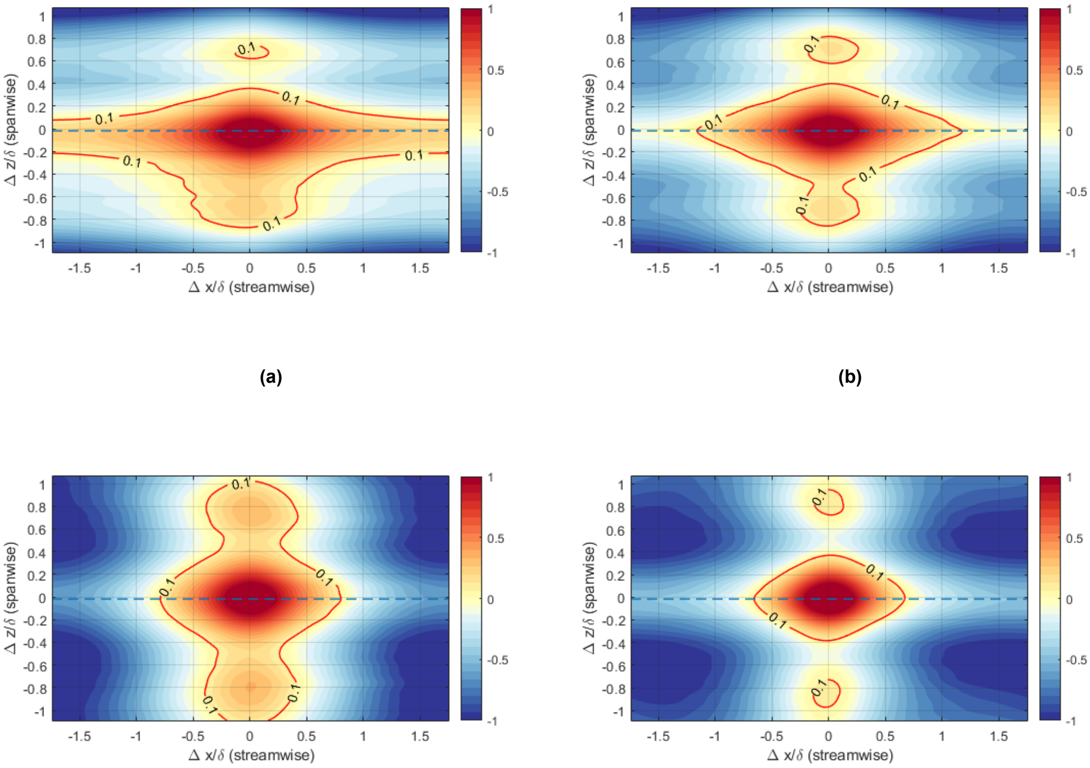

(a) **(b)**

(c) **(d)**

Figure 6.11: Two-point correlation contour of streamwise velocity fluctuations for (a.) Case 1: SW (f = 6Hz, $\lambda = \infty$); (b.) Case 2: SW (f = 12Hz, $\lambda = \infty$); (c.) Case 3: SW (f = 24Hz, $\lambda = \infty$); (d.) Case 4: SW (f = 48Hz, $\lambda = \infty$) at $y^+ = 183$ or $y/\delta = 0.08$.

6.4.2. Traveling Wave (TW)

For TW control strategies, a clear alternating pattern of highly correlated and anti-correlated zones can be observed in the spanwise direction. Furthermore, the spanwise width of these zones is directly proportional to the wavelength of the introduced TW control strategy. Thus, based on the requirements of various tuning strategies, the wavelength set for the TW case can be directly expected to be seen in terms of the spanwise width of the introduced coherent pattern in the log region.

As the actuation frequency increases, the intensity of both highly correlated and anti-correlated zones decreases in the streamwise direction. Additionally, the inclination angle with respect to the x direction for alternating high and low momentum zones increases with actuation frequency. These inclined finger-like patterns also confirm the presence of spanwise shear for the TW control strategy, which was initially speculated (recall Figure 3.5). Moreover, an interesting observation regarding Figure 6.12c and Figure 6.12d is that the overall intensity of the highly correlated zone in the center of the domain is also reduced compared to Figure 6.10. Since decreasing the proportion of high momentum zones in the log region of a TBL is highly desirable due to its interaction with near-wall scales and increasing wall shear property. Therefore, it is speculated that Case 7 and Case 8 have better control authority and the potential to reduce wall shear in the domain.

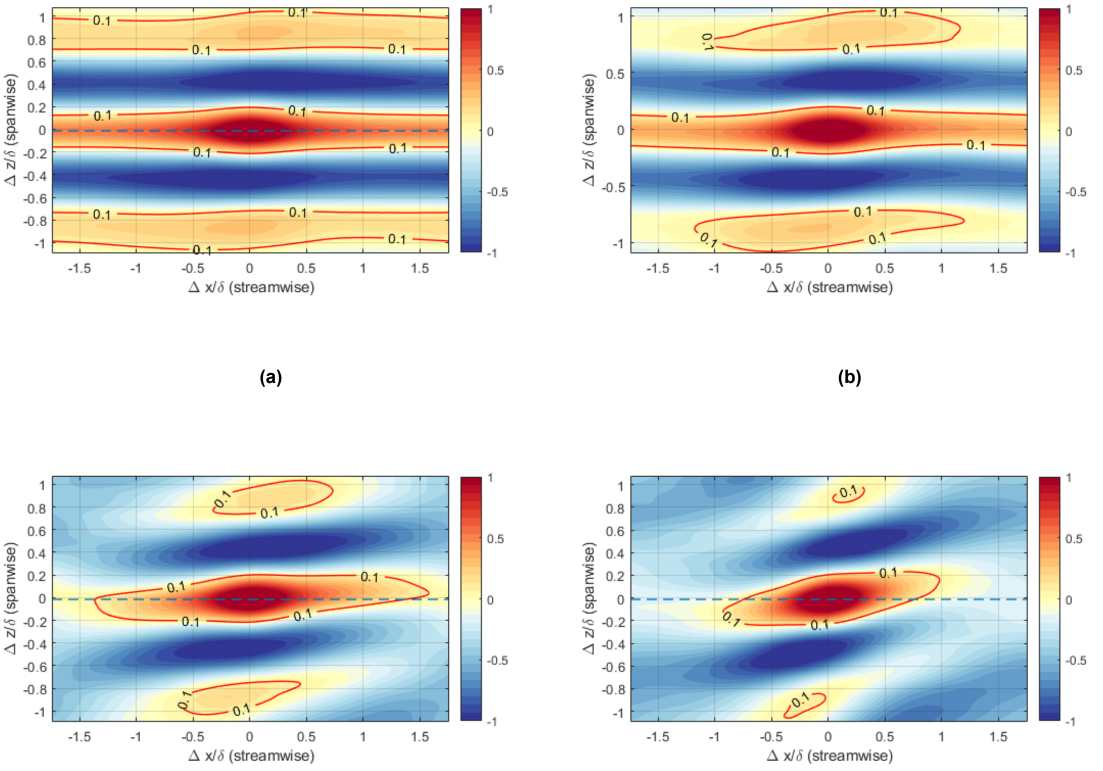

(a)

(b)

(c)

(d)

Figure 6.12: Two-point correlation contour of streamwise velocity fluctuations for (a.) Case 5: TW (f = 6Hz, $\lambda = 0.8 \cdot \delta$); (b.) Case 6: TW (f = 12Hz, $\lambda = 0.8 \cdot \delta$); (c.) Case 7: TW (f = 24Hz, $\lambda = 0.8 \cdot \delta$); (d.) Case 8: TW (f = 48Hz, $\lambda = 0.8 \cdot \delta$) at $y^+ = 183$ or $y/\delta = 0.08$.

Upon analyzing the two-point correlation contours for Case 9, Case 10, Case 11, and Case 12, it was observed that the TW control strategy aimed at $\lambda = 0.4 \cdot \delta$ was not correctly implemented. This is because the jet slit spacing chosen earlier was $0.15 \cdot \delta$, and for an accurate implementation of a spanwise traveling wave with $\lambda = 0.4 \cdot \delta$, the jet slit spacing should be at least $0.1 \cdot \delta$ (as per the Nyquist criterion). As seen in Figure 6.13a and Figure 6.13d, the expected spanwise width of $0.2 \cdot \delta$ is not maintained in the log region. As a result, Case 9 and Case 11 will be discarded and not included in future discussions.

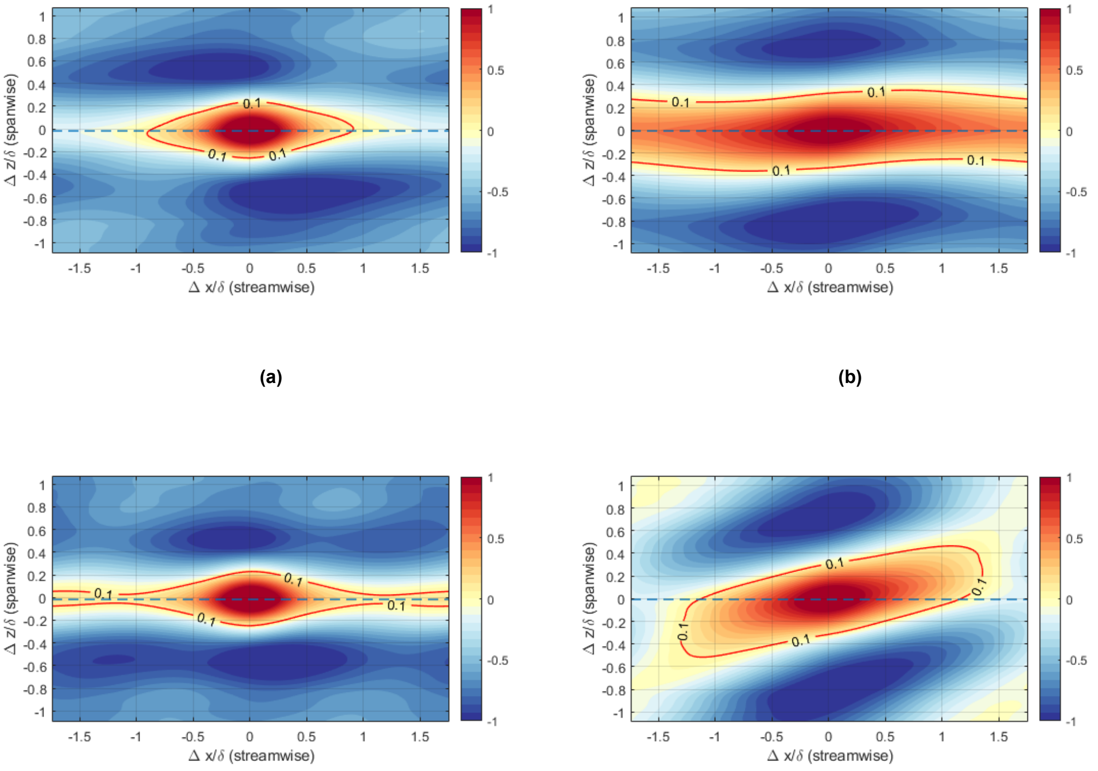

(a)

(b)

(c)

(d)

Figure 6.13: Two-point correlation contour of streamwise velocity fluctuations for (a.) Case 9: TW (f = 12Hz, $\lambda = 0.4 \cdot \delta$); (b.) Case 10: TW (f = 12Hz, $\lambda = 1.6 \cdot \delta$); (c.) Case 11: TW (f = 24Hz, $\lambda = 0.4 \cdot \delta$); (d.) Case 12: TW (f = 24Hz, $\lambda = 1.6 \cdot \delta$) at $y^+ = 183$ or $y/\delta = 0.08$.

6.5. Comparison Of Mean Streamwise Velocity Profile

Different control strategies' non-dimensionalized mean velocity profiles are compared to an uncontrolled case in Figure 6.14. There is a significant shift in the mean velocity profile for all the control cases compared to the uncontrolled case. This shift in the velocity profile can be attributed to various reasons based on different control strategies. One of the first reasons for this change in velocity profile is due to the obstruction created by the jet in cross flow, which reduces flow velocity downstream. However, this reason can be speculated to be consistent throughout all control cases.

Control in terms of SW control strategy injects a zero-momentum fluid into the test section. When the incoming TBL interacts with these introduced jet plumes, the streamwise momentum gets transferred, reducing mean velocity profiles. However, a TW control strategy creates a sudden spanwise pressure gradient, reducing the near-wall turbulence production and RSS downstream. The spanwise inclined coherent pattern seen for the TW control strategy is actuated via an array of jets. These inclined coherent patterns meander with convecting LSMs and breaks them away.

For Figure 6.14, the velocity profile for all different actuation frequency cases collapses together into a single curve. The main reason for this can be the limitation of the mean velocity profile to capture the flow's mean statics rather than minor variations to small scales. As this instantaneous fluctuation carries the primary information regarding the dynamics of a TBL, failing to capture this limits the ability to make a conclusive observation for different control strategies. However, for Figure 6.15, a considerable difference can be observed in the log region. According to this, it can be concluded that different actuation frequencies affect the dynamics of the log region differently for a TW control strategy. One of the main differences in the TW control strategy is the reduction of mean velocity in the log region with an increase in actuation frequency. This is because spanwise coherent pattern are rapidly introduced as the actuation frequency increases which in turn creates more frequent and stronger spanwise shear.

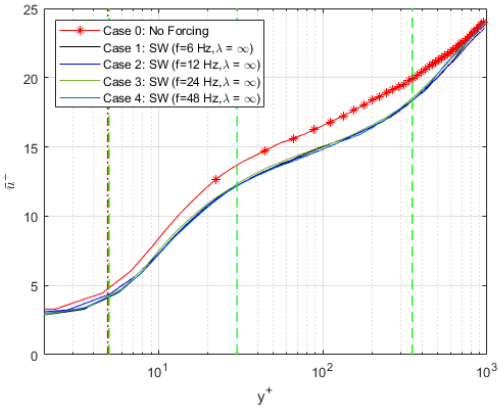

Figure 6.14: Comparison of inner-scale normalized mean streamwise velocity profile for all SW cases with the uncontrolled case.

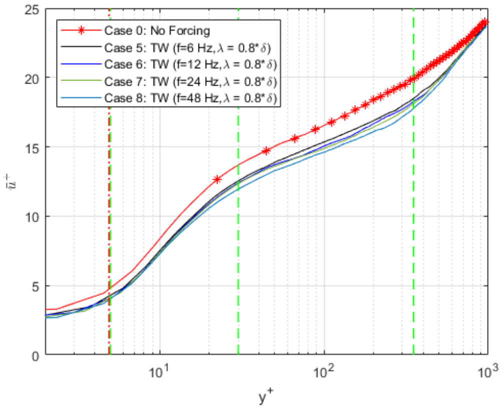

Figure 6.15: Comparison of inner-scale normalized mean streamwise velocity profile for all TW cases with the uncontrolled case.

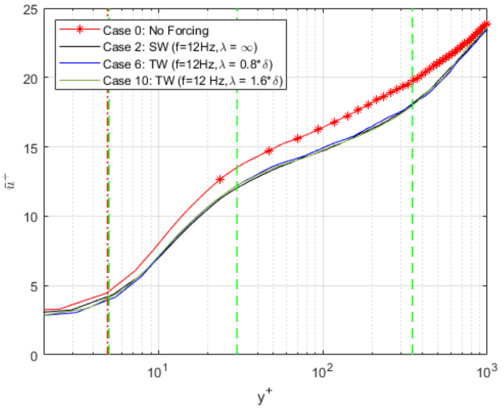

Figure 6.16: Comparison of inner-scale normalized mean streamwise velocity profile for SW and TW actuated at $12Hz$ cases with the uncontrolled case.

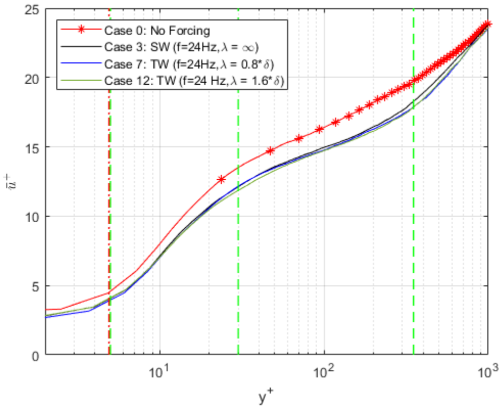

Figure 6.17: Comparison of inner-scale normalized mean streamwise velocity profile for SW and TW actuated at $24Hz$ cases with the uncontrolled case.

For Figure 6.16 and Figure 6.17, no noticeable difference between the SW and TW control strategy was found. Streamwise mean velocity profile being a 1^{st} order mean statistical approach fails to capture the influence of velocity fluctuations, limiting its ability to capture the full dynamics of the TBL flow. A second-order turbulence statics analysis is instrumental in understanding complete flow dynamics. Second-order turbulence statistics include quantities such as RSS and TKE production (P) along the wall-normal direction for a better analysis of the receptivity of individual control strategy on near-wall all-scales.

6.6. Higher-Order Turbulence Statistics

Turbulence statistics play a crucial role in understanding the underlying physics behind each control case. The streamwise velocity fluctuation (u') and wall-normal velocity fluctuation (v') offer more profound insight into the dynamic changes in TBL resulting from various control strategies. Evaluating RSS and TKE production based on these fluctuations allows one to better understand each control case's effectiveness in reducing TKE production and attenuating the spectral energy of large scales.

6.6.1. Reynolds Shear Stresses

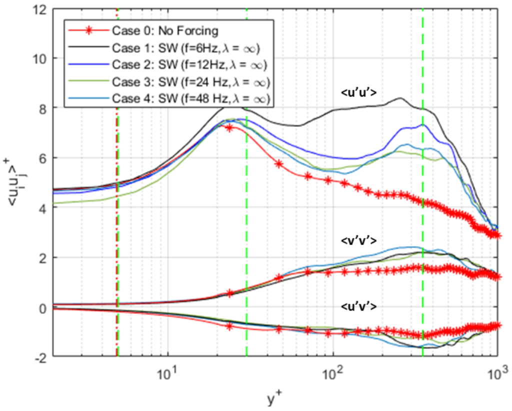

Figure 6.18: Comparison of inner-scale normalized RSS profile for all SW cases with the uncontrolled case.

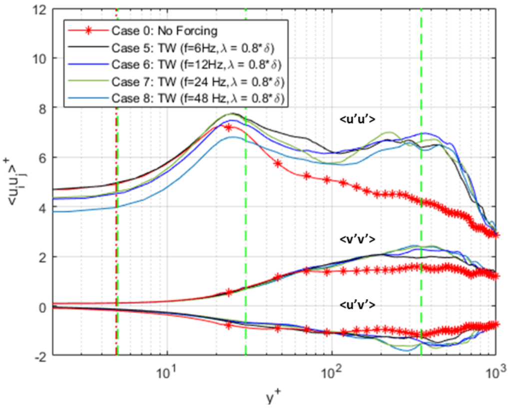

Figure 6.19: Comparison of inner-scale normalized RSS profile for all TW cases with the uncontrolled case.

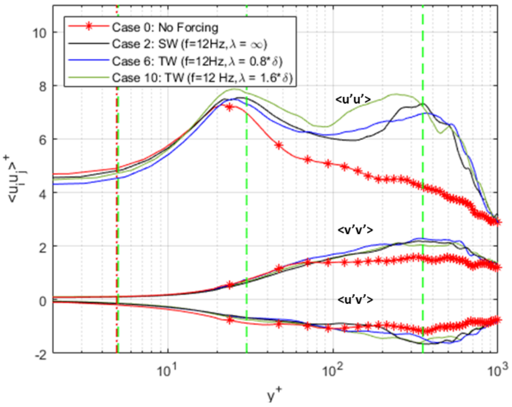

Figure 6.20: Comparison of inner-scale normalized RSS profile for SW and TW actuated at $12Hz$ cases with the uncontrolled case.

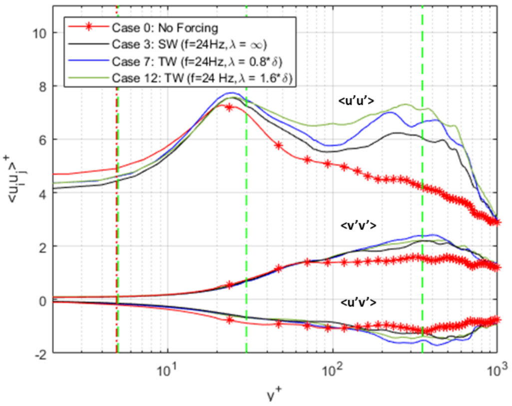

Figure 6.21: Comparison of inner-scale normalized RSS profile for SW and TW actuated at $24Hz$ cases with the uncontrolled case.

The RSS profiles shown in Figure 6.18 and Figure 6.19 compare control cases with the uncontrolled base cases. An increase in RSS for all control cases in the log region and wake can be observed due to the formation of an additional boundary layer from jet actuation. This formation significantly impacts the jet actuation plate's zero pressure gradient condition downstream. Furthermore, as previously discussed, during a periodic actuation cycle of an individual wall-normal jet, the initial jet exit velocity peaks and stabilizes after a certain delay. This initial high exit jet velocity propels a large part of the jet plume out of the targeted middle of the log region, leading to an increase in RSS in the wake of all control cases. However, tracking the RSS profile streamwise would be beneficial for a better understanding of the change in RSS.

In Figure 6.18, a significant reduction in streamwise stresses is observed for Case 3 up to the first peak at $y^+ = 25$. Therefore, it is speculated that the streamwise stress near the wall is attenuated for an actuation frequency of $24Hz$. However, for all other cases, the profile coincides with the unforced case below $y^+ = 25$. This attenuation at $24Hz$ can also be observed in Figure 6.19. For a TW control strategy, the RSS near the wall decreases for control Case 6, Case 7, and Case 8, except for Case 5. Thus, the initial goal of tuning the actuation frequency to the coherent frequency of LSM via $f = 12Hz$ and $f = 24Hz$ appears to impact near-wall streamwise stress. Moreover, the lowest streamwise stress observed for Case 8 compared to the uncontrolled case might be attributed to some differences in processing.

Although there is an increase in streamwise stresses in the log and wake region, Case 3 exhibits lower streamwise stresses throughout the domain compared to all other control cases. The SW control strategy, which commands all actuators to turn *on* and *off* simultaneously, was expected to produce a second peak in streamwise stresses for Case 3 as seen in Case 2 (refer to Figure 6.20 and Figure 6.21). However, this is not observed in reality. The streamwise stress for Case 3 consistently remains lower than the TW control strategy for actuation frequency $f = 24Hz$. Thus, based on the RSS plots, Case 3 has one of the most effective manipulation effects among all other control cases. Another key takeaway from Figure 6.20 and Figure 6.21 is that, for the TW control strategy, $\lambda = 0.8 \cdot \delta$ is best suited for RSS reduction. Consequently, for any future actuation technique, the spanwise wavelength should always be tuned to the spanwise width of high and low momentum zones observed in Figure 6.10.

6.6.2. Turbulent Kinetic Energy Production

The majority of TKE is found in the log region of a TBL, where the convecting LSMs play a significant role in TKE production and transport. In contrast, the near-wall small scales are crucial for TKE dissipation. TKE production is closely related to skin friction generation, as explained by Fukagata et al., 2002. TKE production represents the rate of energy transfer from the mean flow to turbulent fluctuations.

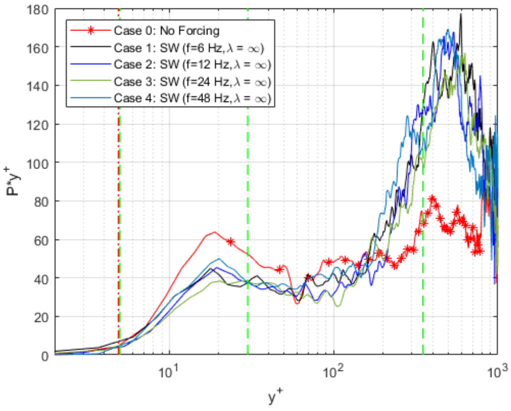

Figure 6.22: Comparison of pre-multiplied TKE production profile for all SW cases with the uncontrolled case.

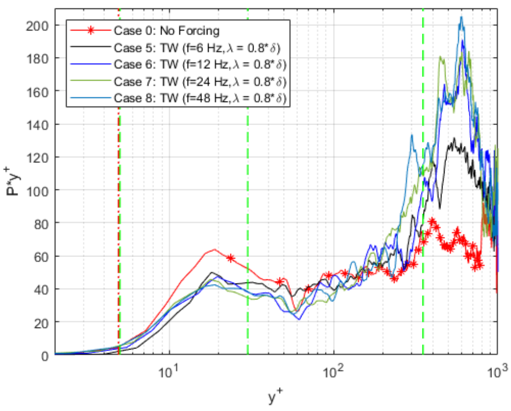

Figure 6.23: Comparison of pre-multiplied TKE production profile for all TW cases with the uncontrolled case.

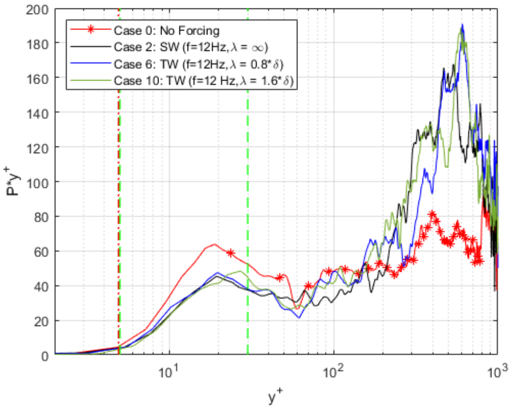

Figure 6.24: Comparison of pre-multiplied TKE production profile for SW and TW actuated at $12Hz$ cases with the uncontrolled case.

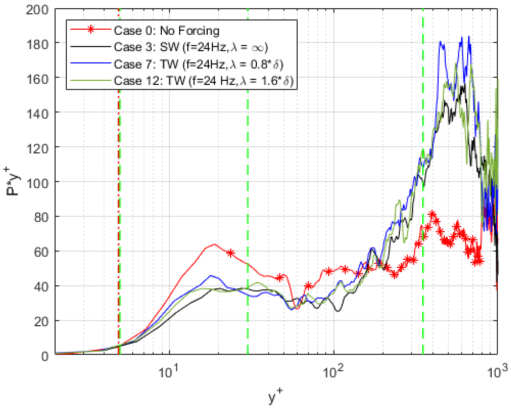

Figure 6.25: Comparison of pre-multiplied TKE production profile for SW and TW actuated at $24Hz$ cases with the uncontrolled case.

The TKE production plots presented below are pre-multiplied with the wall-normal y^+ distance to emphasize the change in TKE production in the log and wake regions. Firstly, the increase in TKE production in these regions confirms the initial assumption that a higher initial jet velocity is responsible for the increase in streamwise stress. Secondly, there is a significant reduction in TKE production for all control cases compared to the uncontrolled case from the wall to the middle of the log region. At

$y^+ = 183$, the TKE production of control cases increases more than that of the uncontrolled case. This point was targeted via the wall-normal jets by setting the jet velocity ratio $r = 0.4$. Consequently, the increase in TKE production after this point is due to the failure of the ZPG condition and the creation of an additional boundary layer because of jet actuation.

The large coherent pattern introduced via jets interacts with LSMs through superposition, adding or subtracting their intensities. This causes the change in RSS and TKE production profiles to be modified by either enhancing or suppressing the momentum transport of existing LSMs. At the same time, the introduced large-scale streaks may also interact through amplitude modulation. In amplitude modulation, large-scale structures interact with near-wall scales, causing a change in their amplitude. After comparing Figure 6.22 and Figure 6.23 for both SW and TW control strategies, the actuation frequency $f = 24Hz$ is found to be most effective in attenuating the TKE production near the wall compared to other frequencies. However, after analyzing Figure 6.24 and Figure 6.25, Case 3 appears to be the most suitable for attenuating near-wall TKE production.

However, as explained by Cheng et al., 2021 and Zhang et al., 2022, interactions of energetic large scales with near-wall scales and obstruction created by jet plumes contribute to drag reduction. Therefore, in this scenario, it is difficult to provide a definitive conclusion regarding the effectiveness of SW and TW control strategies. Thus, with the given PIV measurement data, no plausible explanation was derived for comparing SW and TW control strategies.

6.6.3. Estimation Of Integral Measures

The mean streamwise velocity profile presented in Figure 6.1a can be integrated to calculate the displacement thickness (δ^*) and momentum thickness (θ). The variables δ^* and θ are critical parameters to characterize a TBL as explained in chapter 2. The θ can be an exciting parameter for comparing the uncontrolled case and different control cases. Furthermore, the θ provides a measure of momentum transfer inside TBL, which can be used as a surrogate for trends in skin friction. Therefore, comparing the θ can provide significant insights into the shear stress distribution. Similarly, in the TKE production profile, the TKE production quantities can be integrated to calculate B_{TKE} as explained in Equation 2.21.

The TKE production (P) profiles are integrated to calculate the δ^*, θ, and B_{TKE} over the visible domain of $y^+ = 1000$. These integrated values can be compared and analyzed in Figure 6.26 in the form of a bar graph. However, integrating the values for the whole domain includes the variation caused by increased turbulence production in the wake due to the additional boundary layer formed by jet actuation downstream. To reduce the effect of these non-reality variations, the velocity, and TKE production profiles can be integrated up to the midpoint of the log region. As seen in the TKE production profile, there is an increase in TKE production after $y^+ = 183$ due to jet actuation. Therefore, to understand the collective impact of jets on near-wall scales, the velocity profile, and TKE production profiles are integrated from the wall to the middle of the log region and compared in Figure 6.27.

From Figure 6.27, it is clear that there is a reduction in B_{TKE} for all controlled cases compared to the uncontrolled base case. Notably, the most significant B_{TKE} reduction is observed for actuation frequencies $12Hz$ and $24Hz$. This suggests that the proposed temporal tuning strategies effectively attenuate TKE production compared to random actuation frequencies. However, the highest B_{TKE} reduction is found in Case 3, an SW control strategy actuated at $24Hz$. It is important to note that the difference between Case 3 and Case 7 is minimal. Therefore future analyses can be conducted using HWA measurement data better to understand the effectiveness of SW and TW control strategies.

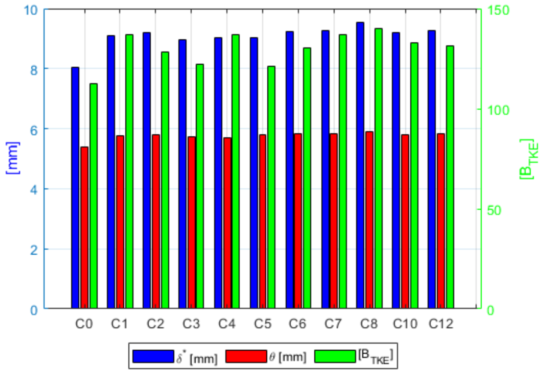

Figure 6.26: Mean streamwise velocity profile and TKE production profile integrated for the full visible domain ($y^+ = 1000$).

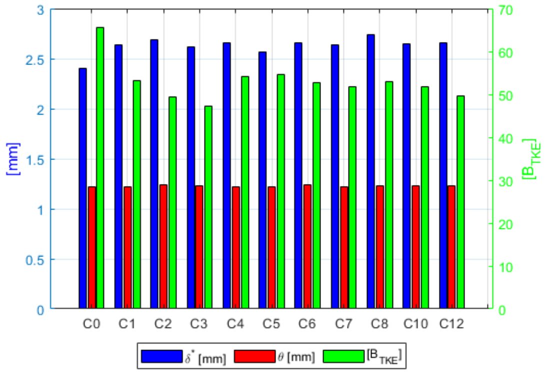

Figure 6.27: Mean streamwise velocity profile and TKE production profile integrated for till middle of the log region ($y^+ = 183$).

6.6.4. Spectral Energy

A spectral energy plot is a graphical tool used to analyze the overall energy distribution within different length scales. The spectral energy plot shown in Figure 6.28 is calculated from the streamwise fluctuating velocity component (u') measured $2.5 \cdot \delta$ downstream from the origin at a wall-normal height of $y^+ = 183$. This y^+ location allows for the analysis of energy distribution within the dominant scales convecting in the log region. Due to the limited temporal resolution of the PIV measurement technique caused by the physical limitations of laser and camera setups, an HWA probe placed in the flow can provide better temporal resolution thanks to its higher acquisition frequency. Comparing these pre-multiplied spectral energies for the uncontrolled base case and different control cases can help understand the control's effect on targeted length scales convecting downstream. For easier comparison, all pre-multiplied energy spectra are normalized by the variance of the uncontrolled Case 0. This normalization re-scales the energy magnitudes of control cases or better comparison of energy distribution across various length scales.

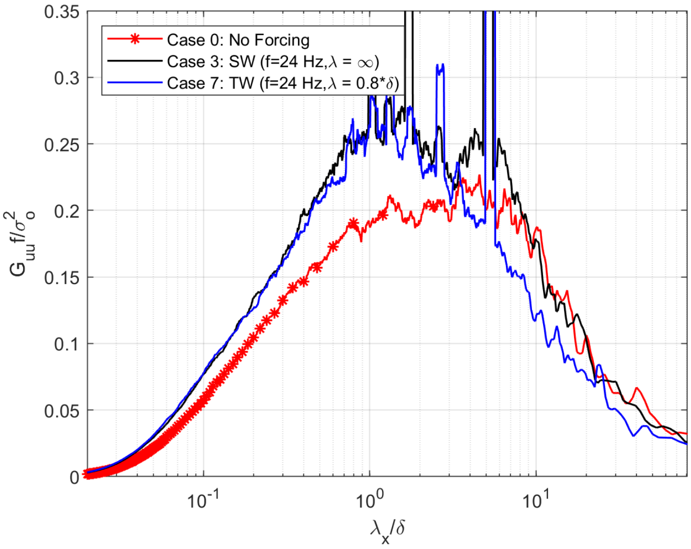

Figure 6.28: Pre-multiplied energy spectra of u' acquired by HWA at (x^+, y^+, z^+) = (5722,183,0) for different controlstrategies actuated at $24Hz$ and normalized by (σ_o^2) of the uncontrolled base case.

In Figure 6.28, the comparison plot of SW and TW control strategies at the most suitable actuation frequency reveals a significant observation for Case 7 compared to Case 3 and the uncontrolled Case 0. Remarkably, for a TW control strategy actuated at $24Hz$ and tuned to the spanwise width of LSMs, the energy contained by larger length scales decreases considerably compared to the uncontrolled base case and SW control case. Figure 6.28 also suggests that jet actuation energizes the near-wall small scales for both control cases. This was expected earlier as the jet in cross flow frequently induces near-wall small scales. However, the TW control strategy actuated at $24Hz$ effectively attenuates the energy content of length scales larger than $3 \cdot \delta$. This is a crucial takeaway from the spectral energy plots, indicating that the TW control strategy has greater control authority than the SW control strategy. Therefore, it can be hypothesized that the TW control strategy, tuned to the frequency of energetic large scales (calculated from mean scale convection velocity at the middle of log region) convecting in the log region, outperforms all other control cases and offers better controllability [Zhang et al., 2022].

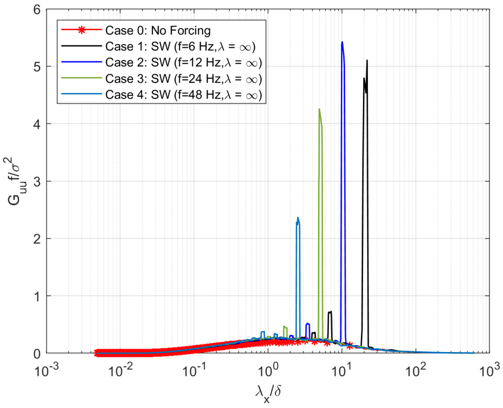

Figure 6.29: Pre-multiplied energy spectra of u' acquired by HWA at (x^+, y^+, z^+) = (5722,183,0) for SW controlstrategies and normalized by (σ_o^2) of the uncontrolled base case.

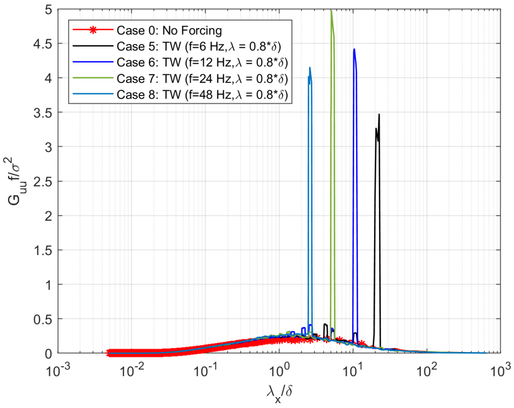

Figure 6.30: Pre-multiplied energy spectra of u' acquired by HWA at (x^+, y^+, z^+) = (5722,183,0) for TW controlstrategies and normalized by (σ_o^2) of the uncontrolled base case.

Upon examining the individual peaks in Figure 6.29 and Figure 6.30, it can be confirmed that the forcing frequency of each control strategy is successfully implemented. A notable difference between Figure 6.29 and Figure 6.30 is the location of the second peak for individual actuation frequencies for the SW and TW control strategies. In the case of the SW control strategy, the introduced streak loses its spanwise coherence as it convects downstream. This breakup results in a non-linear interaction with the convecting TBL and causes the second peak to appear slightly higher than the next multiple of the actuation frequency. Conversely, in the case of the TW control strategy, the jets are continuously actuated, generating a more coherent pattern in the spanwise direction. This coherence can lead to harmonics more closely aligned with the next multiple of the actuation frequency.

To better understand the underlying physical mechanism behind the reduction in the inner peak of TKE production and the decrease in spectral energy for larger length scales, advanced PIV techniques such as Tomographic PIV can be employed to obtain 3-D velocity fields. Analyzing these velocity fields can offer detailed insights into the evolution and interaction of the introduced coherent patterns with convecting highly energetic LSMs. Even though the differences between the SW and TW control strategies still need to be thoroughly established, the temporal tuning strategy employed in this thesis has demonstrated significant control potential for large-scale structures. Furthermore, using the suggested temporal tuning strategy, the TW control strategy successfully reduced energy at larger length scales, indicating its potential for future large-scale manipulation techniques.

7

Conclusion

As the world steadily moves towards a sustainable and greener future, all of the major industries across the globe are looking for innovative ways to minimize their carbon footprint. Following the same goal, the aviation industry is also looking for innovative ways to make air travel more efficient. Given the higher proportion of viscous drag to overall drag and the aircraft fuselage being the most significant contributor, viscous drag reduction for a turbulent boundary layer over a ZPG flat plate has been a topic of extensive research recently. Active techniques are far more suited and effective for real-world application than passive drag reduction techniques. An active control strategy's primary advantage is its effectiveness far downstream of the point of actuation. The active drag reduction technique can be tuned to near-wall small scales or outer-wall large scales. The main disadvantage of small-scale manipulation is very low T^+_{OSC} for a more practical Reynolds number. This can be in the order of $1-10$ for near-wall small scales, making it very energy intensive and challenging to manipulate via existing actuators. This paved the way to look for efficient large-scale manipulation to achieve net drag reduction. As these large scales are responsible for most of the turbulent kinetic energy in the TBL, their manipulation can be highly effective. Manipulating these large-scale structures is efficient as they directly influence the small scales via amplitude modulation and superposition. Hence these effects enable the drag reduction to cascade through the TBL in terms of reduction in wall shear stress.

Several active large-scale manipulation techniques, such as wall oscillation, synthetic jets, steady and unsteady blowing flow control techniques, have been developed over several years to achieve a global net drag reduction. While these control techniques show promising results under certain conditions, the complexity of incorporating these into aircraft for cruising flight conditions is impossible. Given these challenges, only blowing technique targeting large scales emerges promising to manipulate and get realistically implemented effectively. The practicality of implementing blowing jet slits into aircraft fuselage and its potential effectiveness at higher Reynolds numbers made this thesis topic attractive for future research and development.

Previous research by Marusic et al., 2021 demonstrated that the contribution of large-scale eddies increases with the Reynolds number, suggesting that the efficiency of large-scale manipulation is significantly higher than estimated in laboratory experiments. Based on this and other studies, it was hypothesized that an active blowing technique could be tuned to convecting large scales using multiple strategies. However, a direct measurement of the coherent frequency of LSMs has yet to be established. This frequency can be estimated either by determining the convection velocity of *(1.)* the near wall fluctuation, or *(2.)* the hairpin head at the middle of the logarithmic region. The middle portion of the log region is particularly interesting as it is where most large scales persist [Abbassi et al., 2017]. These suggested tuning approaches allowed for a more accurate estimation of the coherent frequency of large-scale structures, which can be further utilized to develop and optimize future large-scale manipulation techniques. Moreover, the effectiveness of spanwise traveling waves through wall-normal deformation led to the exploration of multiple control strategies, such as Standing Wave (SW) and Spanwise Traveling Wave (TW). The SW control technique introduces a large two-dimensional coherent pattern, while the TW control strategy generates periodic spanwise shear. Although both control strategies have been proven to reduce drag downstream, a global effect remains to be established.

The proposed tuning strategies were implemented in the experimental campaign for both control strategies. Based on this, 12 different control case combinations were defined, as explained in section 4.5. Considering these control case implementations, the actuation setup and jet plate design were derived from existing research to effectively interact with convecting large scales. The methodology, actuation setup design, fabrication, and implementation are detailed in chapter 4. Flow measurement techniques such as Particle Image Velocimetry (PIV) and Hot-Wire Anemometry (HWA) were used to investigate the effectiveness of each control strategy and actuation frequency.

As there is no direct way to measure the overall drag inside the test section, Reynolds Shear Stress (RSS), Turbulent Kinetic Energy (TKE) production, and spectral energy plots of streamwise velocity fluctuations were analyzed to assess the effectiveness of each control case. These profiles are closely related to momentum transfer and energy dissipation within the TBL, impacting the overall wall shear. The instantaneous flow fields captured for FOV-A (wall-parallel) at $y^+ = 183$ can be analyzed using a two-point correlation function to estimate the spatial organization of scales in the TBL. This method is essential for understanding the complex organization of various flow structures. Additionally, the turbulence statistics calculated for the FOV-B (wall-normal) plane at $2.5 \cdot \delta$ downstream of jet actuation provide valuable information on the global effect of each control case.

From chapter 6, it was evident that the actuation frequency ($f = 24Hz/f^+ = 0.112$) calculated with convection velocity estimated from the mean streamwise velocity at the middle of the log region most efficiently attenuates the TKE production near the wall. The higher RSS and TKE production seen at the log and the wake region in subsection 6.6.1 and subsection 6.6.2 is due to the fact that there is an additional boundary layer introduced via jet actuation. This creates higher shear and turbulence downstream of the jet actuation plate. However, to reduce the effect of local variation, the mean stream velocity profile and TKE production profile can be integrated till the middle point log region to calculate displacement thickness (δ^*), momentum thickness (θ), and bulk TKE production (B_{TKE}). This can ensure an unbiased analysis of the effect of individual control cases on the near-wall regions. However, the difference in SW and TW control strategies is difficult to establish via PIV data. After analyzing the spectral energy plot of streamwise velocity fluctuations at wall normal height of $y^+ = 183$ and downstream distance of $2.5 \cdot \delta$, it was evident that Case 7 representing a traveling wave actuated at $f = 24Hz/f^+ = 0.112$ and spatially tuned to spanwise width of LSMs ($0.8 \cdot \delta$) effectively attenuates the energy content of large length scales. To better comprehend this behavior and the difference between SW and TW control strategies, future research can keep certain factors in mind. These future recommendations are described in chapter 8.

8

Future Recommendations

The work presented in this thesis report is a first attempt to manipulate the large energetic scales via a spanwise array of wall-normal jets. These jets can be temporally tuned to LSMs via various control cases to manipulate them and achieve a global drag reduction. Even though not a well-established conclusion was drawn for each control case, these results have served to reduce the pre-multiplied energy for larger length scales. Therefore this work can potentially be the start of future investigations.

The following points can be considered future recommendations and extensions concerning the work and results discussed in this report.

1. Direct drag measurement methods such as hot-film can drag balance set behind the jet actuation plate to quantify the overall global effect corresponding to the individual control cases.
2. A zoomed-in wall-normal PIV measurement along multiple downstream field of view can help to understand the influence of each control case on RSS distribution. In addition, a zoomed-in PIV measurement can directly quantify the friction velocity, giving a direct comparison between each control case.
3. An advanced Tomographic PIV technique can be implemented to visualize the interaction between existing energetic large scales and introduced coherent streaks. This can help understand the reason behind the reduction of energy for larger scales in the Traveling wave forcing strategy.
4. The jet slit spacing explained in section 4.6 can be better optimized to analyze better the effect of different spatial tuning strategies as explained in section 4.5.
5. The convection velocity estimated for the large convecting scales in the log region can be estimated more precisely using free wake models for better tuning efficacy.
6. Additionally, a random actuation case can be implemented to analyze the effect of individual forcing strategies. Normalizing the results with a random actuation case will help establish the difference between the effect of temporal and spatial tuning and the effect of jet blowing.
7. For the standing wave forcing strategy, spanwise arranged slits can be researched as they have a better tendency to maintain the spanwise coherence of introduced streaks.

Therefore, it is highly recommended to keep these points in mind while carrying out future investigations inspired by this research work.

References

Abbassi, M. R., Baars, W. J., Hutchins, N., & Marusic, I. (2017). Skin-friction drag reduction in a high-Reynolds-number turbulent boundary layer via real-time control of large-scale structures. *International Journal of Heat and Fluid Flow*, *67*, 30–41. https://doi.org/10.1016/j.ijheatfluidflow.2017.05.003

Adrian, R. J., Meinhart, C. D., & Tomkins, C. D. (2000). Vortex organization in the outer region of the turbulent boundary layer. *Journal of Fluid Mechanics*, *422*, 1–54. https://doi.org/10.1017/S0022112000001580

Airbus. (2020). *Aviation connects and unites us!* https://www.airbus.com/en/products-services/commercial-aircraft/market/global-market-forecast

Albers, M., Meysonnat, P. S., Fernex, D., Semaan, R., Noack, B. R., & Schröder, W. (2020). Drag reduction and energy saving by spanwise traveling transversal surface waves for flat plate flow. *Flow, Turbulence and Combustion*, *105*, 125–157. https://doi.org/10.1007/s10494-020-00110-8

Antonia, R. A., Zhu, Y., & Sokolov, M. (1995). Effect of concentrated wall suction on a turbulent boundary layer. *Physics of Fluids*, *7*, 2465–2474. https://doi.org/10.1063/1.868690

Baars, W. J., & Dacome, G. (2022). *Characteristics of jet actuators and ni board*.

Baars, W. J., Hutchins, N., & Marusic, I. (2016). Spectral stochastic estimation of high-reynolds-number wall-bounded turbulence for a refined inner-outer interaction model. *Physical Review Fluids*, *1*, 054406. https://doi.org/10.1103/PhysRevFluids.1.054406

Baars, W. J., & Marusic, I. (2020). Data-driven decomposition of the streamwise turbulence kinetic energy in boundary layers. part 1. energy spectra. *Journal of Fluid Mechanics*, *882*, A25. https://doi.org/10.1017/jfm.2019.834

Benedict, L. H., & Gould, R. D. (1996). Towards better uncertainty estimates for turbulence statistics. *Experiments in Fluids*, *22*, 129–136. https://doi.org/10.1007/s003480050030

Blackwelder, R. F., & Kovasznay, L. S. (1972). Time scales and correlations in a turbulent boundary layer. *Physics of Fluids*, *15*, 1545–1554. https://doi.org/10.1063/1.1694128

Bradshaw, P., & Pontikos, N. S. (1985). Measurements in the turbulent boundary layer on an ‘infinite’ swept wing. *Journal of Fluid Mechanics*, *159*, 105. https://doi.org/10.1017/S0022112085003123

Buschmann, M. H., & Gad-El-Hak, M. (2006). Structure of the canonical turbulent wall-bounded flow. *AIAA Journal*, *44*, 2500–2504. https://doi.org/10.2514/1.19172

Cengel, Y. A. (2010). *Fluid mechanics* (2nd ed.). Tata McGraw Hill Education Private Limited, 2010.

Chan, I. C., Örlü, R., & Schlatter, P. (2021). The skin-friction coefficient of a turbulent boundary layer modified by a large-eddy break-up device collections articles you may be interested in. *Phys. Fluids*, *33*, 35153. https://doi.org/10.1063/5.0043984

Chauhan, K. A., Monkewitz, P. A., & Nagib, H. M. (2009). Criteria for assessing experiments in zero pressure gradient boundary layers. *Fluid Dynamics Research*, *41*. https://doi.org/10.1088/0169-5983/41/2/021404

Chen, J. (2019). Two-point statistics of coherent structure in turbulent flow. *Journal of Flow Control, Measurement And Visualization*, *07*, 153–173. https://doi.org/10.4236/jfcmv.2019.74012

Cheng, X. Q., Qiao, Z. X., Zhang, X., Quadrio, M., & Zhou, Y. (2021). Skin-friction reduction using periodic blowing through streamwise slits. *Journal of Fluid Mechanics*, *920*. https://doi.org/10.1017/jfm.2021.439

Choi, K. S., DeBisschop, J. R., & Clayton, B. R. (1998). Turbulent boundary-layer control by means of spanwise-wall oscillation. *AIAA Journal*, *36*, 1157–1163. https://doi.org/10.2514/2.526

Corino, E., & Brodkey, R. S. (1965). A visual investigation of the wall region in turbulent flow. *Journal of Fluid Mechanics*, *37*, 1–30.

Corke, T. C., Guezennec, Y., & Nagib, H. M. (1981). *Nasa contractor modification in drag of turbulen boundary layers resulting from manipulation of large-scale structures nasa*.

Dacome, G. (2022a). *Delft-aerospace tbl flow characterization*.

Dacome, G. (2022b). *Designing and fabrication of jet plate*.

Du, Y., & Karniadakis, G. E. (2000). Suppressing wall turbulence by means of a transverse traveling wave. *Science*, *288*, 1230–1234. https://doi.org/10.1126/science.288.5469.1230

Fukagata, K., Iwamoto, K., & Kasagi, N. (2002). Contribution of reynolds stress distribution to the skin friction in wall-bounded flows. *Physics of Fluids*, *14*, L73–L76. https://doi.org/10.1063/1.1516779

Ganapathisubramani, B., Longmire, E. K., & Marusic, I. (2003). Characteristics of vortex packets in turbulent boundary layers. *Journal of Fluid Mechanics*, *478*, 35–46. https://doi.org/10.1017/S0022112002003270

García-Mayoral, R., & Jiménez, J. (2011). Drag reduction by riblets. *Philosophical Transactions of the Royal Society A: Mathematical, Physical and Engineering Sciences*, *369*, 1412–1427. https://doi.org/10.1098/rsta.2010.0359

Gatti, D., & Quadrio, M. (2016). Reynolds-number dependence of turbulent skin-friction drag reduction induced by spanwise forcing. *Journal of Fluid Mechanics*, *802*, 553–582. https://doi.org/10.1017/jfm.2016.485

Ghaemi, S. (2020). Passive and active control of turbulent flows. *Physics of Fluids*, *32*, 080401. https://doi.org/10.1063/5.0022548

Gutmark, E. J., Ibrahim, I. M., & Murugappan, S. (2008). Circular and noncircular subsonic jets in cross flow. *Physics of Fluids*, *20*, 075110. https://doi.org/10.1063/1.2946444

Head, M. R., & Bandyopadhyay, P. R. (1981). New aspects of turbulent boundary-layer structure. *Journal of Fluid Mechanics*, *107*, 297–338.

Hehner, M. T., Gatti, D., & Kriegseis, J. (2019). Stokes-layer formation under absence of moving parts—a novel oscillatory plasma actuator design for turbulent drag reduction. *Physics of Fluids*, *31*, 051701. https://doi.org/10.1063/1.5094388

Hoyas, S., & Jiménez, J. (2008). Reynolds number effects on the reynolds-stress budgets in turbulent channels. *Physics of Fluids*, *20*, 101511. https://doi.org/10.1063/1.3005862

Hutchins, N., & Marusic, I. (2007a). Evidence of very long meandering features in the logarithmic region of turbulent boundary layers. *Journal of Fluid Mechanics*, *579*, 1–28. https://doi.org/10.1017/S0022112006003946

Hutchins, N., Monty, J. P., Ganapathisubramani, B., & Marusic, I. (2011). Three-dimensional conditional structure of a high-reynolds-number turbulent boundary layer. *Journal of Fluid Mechanics*, *673*, 255–285. https://doi.org/10.1017/S0022112010006245

Hutchins, N., & Marusic, I. (2007b). Large-scale influences in near-wall turbulence. *Philosophical Transactions of the Royal Society A: Mathematical, Physical and Engineering Sciences*, *365*, 647–664. https://doi.org/10.1098/rsta.2006.1942

Itoh, M., Tamano, S., Yokota, K., & Taniguchi, S. (2006). Drag reduction in a turbulent boundary layer on a flexible sheet undergoing a spanwise traveling wave motion. *Journal of Turbulence*, *7*, 1–17. https://doi.org/10.1080/14685240600647064

IUSO, G., ONORATO, M., SPAZZINI, P. G., & CICCA, G. M. D. (2002). Wall turbulence manipulation by large-scale streamwise vortices. *Journal of Fluid Mechanics*, *473*, 23–58. https://doi.org/10.1017/S0022112002002574

Jimenez, J., & Hoyas, S. (2008). Turbulent fluctuations above the buffer layer of wall-bounded flows. *Journal of Fluid Mechanics*, *611*, 215–236. https://doi.org/10.1017/S0022112008002747

Jung, W. J., Mangiavacchi, N., & Akhavan, R. (1992). Suppression of turbulence in wall□bounded flows by high□frequency spanwise oscillations. *Physics of Fluids A: Fluid Dynamics*, *4*, 1605–1607. https://doi.org/10.1063/1.858381

Kempaiah, K. U., Scarano, F., Elsinga, G. E., van Oudheusden, B. W., & Bermel, L. (2020). 3-dimensional particle image velocimetry based evaluation of turbulent skin-friction reduction by spanwise wall oscillation. *Physics of Fluids*, *32*, 085111. https://doi.org/10.1063/5.0015359

Kim, K. C., & Adrian, R. J. (1999). Very large-scale motion in the outer layer. *Physics of Fluids*, *11*, 417–422. https://doi.org/10.1063/1.869889

Kline, S. J., Reynolds, W. C., Schraubt, F. A., & Runstadlers, P. W. (1967). The structure of turbulent boundary layers. *J. Fluid Meeh*, *30*, 741–773. https://doi.org/10.1017/S0022112067001740

Kline, S. J., & Robinson, S. K. (1990). Quasi-coherent structures in the turbulent boundary layer. i - status report on a community-wide summary of the data.

Kornilov, V. (2021). Combined blowing/suction flow control on low-speed airfoils. *Flow, Turbulence and Combustion*, *106*, 81–108. https://doi.org/10.1007/s10494-020-00157-7

Laadhari, F., Skandaji, L., & Morel, R. (1994). Turbulence reduction in a boundary layer by a local spanwise oscillating surface. *Physics of Fluids*, *6*, 3218–3220. https://doi.org/10.1063/1.868052

Liu, C., & Gayme, D. F. (2020). An input-output based analysis of convective velocity in turbulent channels. *Journal of Fluid Mechanics*, *888*, A321–A3232. https://doi.org/10.1017/jfm.2020.48

Marusic, I., Chandran, D., Rouhi, A., Fu., M. K., Wine, D., Holloway, B., Chung, D., & Smits, A. J. (2021). An energy-efficient pathway to turbulent drag reduction. *Nature Communications*, *12*(1), 1–8. https://doi.org/10.1038/s41467-021-26128-8

Meinhart, C., & Adrian, R. (1995). On the existence of uniform momentum zones in a turbulent boundary layer. *Physics of Fluids*, *7*. https://doi.org/10.1063/1.868594

Modesti, D., Endrikat, S., Hutchins, N., & Chung, D. (2021). Dispersive stresses in turbulent flow over riblets. *Journal of Fluid Mechanics*, *917*, A55. https://doi.org/10.1017/jfm.2021.310

Nychast, S. G., Hershey, H. C., & Brodkey, R. S. (2022). A visual study of turbulent shear flow. *J. Fluid Mech*, *3*, 513–540. https://doi.org/10.1017/S0022112073000844

Offen, G. R., & Kline, S. J. (1974). Combined dye-streak and hydrogen-bubble visual observations of a turbulent boundary layer. *Journal of Fluid Mechanics*, *62*(2), 223–239. https://doi.org/10.1017/S0022112074000656

Offen, G. R., & Kline, S. J. (2022). A proposed model of the bursting process in turbulent boundary layers. *J. Fluid Mech*, *70*, 209–228. https://doi.org/10.1017/S002211207500198X

Park, J., & Choi, H. (1999). Effects of uniform blowing or suction from a spanwise slot on a turbulent boundary layer flow. *Physics of Fluids*, *11*, 3095–3105. https://doi.org/10.1063/1.870167

Perlin, M., Dowling, D. R., & Ceccio, S. L. (2016). *Freeman scholar review: Passive and active skin-friction drag reduction in turbulent boundary layers*. https://doi.org/10.1115/1.4033295

Perry, A. E., & Chong, M. S. (2022). On the mechanism of wall turbulence, 173–217. https://doi.org/10.1017/S0022112082001311

Pope, S. B. (2000). *Turbulent flows*. Cambridge University Press. https://doi.org/10.1017/CBO9780511840531

Praturi, A. K., & Brodkey, R. S. (1978). A stereoscopic visual study of coherent structures in turbulent shear flow. *Journal of Fluid Mechanics*, *89*, 251–272. https://doi.org/10.1017/S0022112078002608

Quadrio, M., & Ricco, P. (2004). Critical assessment of turbulent drag reduction through spanwise wall oscillations. *Journal of Fluid Mechanics*, *521*, 251–271. https://doi.org/10.1017/S0022112004001855

Raffel, M., Willert, C. E., Wereley, S. T., & Kompenhans, J. (2007). *Particle image velocimetry*. Springer Berlin Heidelberg. https://doi.org/10.1007/978-3-540-72308-0

Rao, I., & Narasimha, R. (2022). The ’bursting’ phenomenon in a turbulent boundary layer. *J. Fluid Mech*, *48*, 339–352. https://doi.org/10.1017/S0022112071001605

Ricco, P. (2004). Modification of near-wall turbulence due to spanwise wall oscillations. *Journal of Turbulence*, *5*, N24. https://doi.org/10.1088/1468-5248/5/1/024

Ricco, P., Ottonelli, C., Hasegawa, Y., & Quadrio, M. (2012). Changes in turbulent dissipation in a channel flow with oscillating walls. *Journal of Fluid Mechanics*, *700*, 77–104. https://doi.org/10.1017/jfm.2012.97

Richadson, L. F. (1922). Acusolve training manual: Turbulence scales and the energy cascade [Accessed on February 14, 2023]. https://2021.help.altair.com/2021/hwsolvers/acusolve/topics/acusolve/training_manual/turb_scales_energy_cascasde_r.htm

Robinson, S. K. (1991). Coherent motions in the turbulent boundary layer. *Annual Review of Fluid Mechanics*, *23*(1), 601–639. https://doi.org/10.1146/annurev.fl.23.010191.003125

Ruan, Z. (2021). *Active control of large-scale structures in high reynolds number turbulent boundary layers*.

Sano, M., & Hirayama, N. (1985). Turbulent boundary layers with injection and suction through a slit : 1st report, mean and turbulence characteristics. *Bulletin of JSME*, *28*, 807–814. https://doi.org/10.1299/jsme1958.28.807

Sau, R., & Mahesh, K. (2008). Dynamics and mixing of vortex rings in crossflow. *Journal of Fluid Mechanics*, *604*, 389–409. https://doi.org/10.1017/S0022112008001328

Schlichting, H., & Gersten, K. (2016). *Boundary-layer theory*. Springer Berlin Heidelberg. https://doi.org/10.1007/978-3-662-52919-5

Sendstad, O. (1992). The near wall mechanics of three dimensional turbulent boundary layers. *Stanford University*.

Sillero, J. A., Jiménez, J., & Moser, R. D. (2014). Two-point statistics for turbulent boundary layers and channels at reynolds numbers up to δ ⁺ ≈ 2000. *Physics of Fluids*, *26*, 105109. https://doi.org/10.1063/1.4899259

Smith, C. R. (1983). Observation of streamwise rotation in the near-wall region of a turbulent boundary layer. *Physics of Fluids*, *26*, 641. https://doi.org/10.1063/1.864178

Smith, C. R., Walker, J. D. A., Haidari, A. H., & Taylor, B. K. (1990). Hairpin vortices in turbulent boundary layers: The implications for reducing surface drag. In A. Gyr (Ed.). Springer Berlin Heidelberg.

Smits, A. J., & Sreenivasan, K. R. (2010). Coherent structures in turbulence. *Journal of Fluid Mechanics*, *642*, 1–4.

Smits, A. J., McKeon, B. J., & Marusic, I. (2011). High-reynolds number wall turbulence. *Annual Review of Fluid Mechanics*, *43*, 353–375. https://doi.org/10.1146/ANNUREV-FLUID-122109-160753

Spinosa, E., & Zhong, S. (2017). Reduction of skin friction drag in a turbulent boundary layer using circular synthetic jets. *55th AIAA Aerospace Sciences Meeting*. https://doi.org/10.2514/6.2017-0324

Talluru, M. K. (2014). *Manipulating large-scale structures in a turbulent boundary layer using a wall-normal jet*.

Tardu, S. (1998). Near wall turbulence control by local time periodical blowing. *Experimental Thermal and Fluid Science*, *16*, 41–53. https://doi.org/https://doi.org/10.1016/S0894-1777(97)10011-5

Tardu, S. (1999). Localized unsteady blowing and near wall turbulence control. *Proc of the 1st international symposium on the turbulence and shear flow phenomena*, 399–404.

Tardu, S., & Doche, O. (2009). Active control of the turbulent drag by a localized periodical blowing dissymmetric in time. *Experiments in Fluids*, *47*, 19–26. https://doi.org/10.1007/s00348-009-0630-9

Theodorsen, T. (1955). The structure of turbulence. In H. Görtler & W. Tollmien (Eds.), *50 jahre grenzschichtforschung: Eine festschrift in originalbeiträgen* (pp. 55–62). Vieweg+Teubner Verlag. https://doi.org/10.1007/978-3-663-20219-6_6

Umair, M., Tardu, S., & Doche, O. (2022). Reynolds stresses transport in a turbulent channel flow subjected to streamwise traveling waves. *Physical Review Fluids*, *7*, 054601. https://doi.org/10.1103/PhysRevFluids.7.054601

Wallace, J. M., E., H., & Brodkeyp, R. S. (2022). The wall region in turbulent shear flow. *J. Fluid Mech*, *54*, 39–48. https://doi.org/10.1017/S0022112072000515

Wang, L., Huang, W., Xu, C., Shen, L., & Zhang, Z. (2019). Relationship between wall shear stresses and streamwise vortices. *Applied Mathematics and Mechanics*, *40*, 381–396. https://doi.org/10.1007/s10483-019-2448-8

Yudhistira, I., & Skote, M. (2011). Direct numerical simulation of a turbulent boundary layer over an oscillating wall. *Journal of Turbulence*, *12*, 1–17. https://doi.org/10.1080/14685248.2010.538397

Zhang, X., Wong, C. W., Cheng, X. Q., & Zhou, Y. (2022). Dependence of skin-friction reduction on the geometric parameters of blowing jet array. *Physics of Fluids*, *34*, 105125. https://doi.org/10.1063/5.0101289

Zhou, J., Adrian, R. J., Balachandar, S., & Kendall, T. M. (1999). Mechanisms for generating coherent packets of hairpin vortices in channel flow. *Journal of Fluid Mechanics*, *387*, 353–396. https://doi.org/10.1017/S002211209900467X